ELECTRODEPOSITED METAL MATRIX COMPOSITES FOR ENHANCED CORROSION PROTECTION AND MECHANICAL PROPERTIES

Casey Ray Thurber, B.S.

Dissertation Prepared for the Degree of

DOCTOR OF PHILOSOPHY

UNIVERSITY OF NORTH TEXAS

May 2016

APPROVED:

Teresa D. Golden, Major Professor
Nandika Anne D'Souza, Committee Member
Francis D'Souza, Committee Member
Oliver M.R. Chyan, Committee Member
Adel M.A. Mohamed, Committee Member
Michael G. Richmond, Chair of the Department of Chemistry
Costas Tsatsoulis, Dean of the Toulouse Graduate School

Thurber, Casey Ray. Electrodeposited Metal Matrix Composites for Enhanced Corrosion Protection and Mechanical Properties. Doctor of Philosophy (Chemistry-Analytical Chemistry), May 2016, 156 pp, 27 tables, 54 figures, references, 227 titles.

In the oil and gas industry, high corrosion resistance and hardness are needed to extend the lifetime of coatings due to exposure to high stress and salt environments. Electrodeposition has become a favorable technique in synthesizing coatings because of low cost, convenience, and the ability to work at low temperatures. Electrodeposition of metal matrix composites has become popular for enhanced corrosion resistance and hardness in the oil and gas industry because of the major problems that persist with corrosion. Two major alloys of copper-nickel, 90-10 and 70-30, were evaluated for microbial corrosion protection in marine environments on a stainless steel substrate. Copper and copper alloys are commonly used in marine environments to resist biofouling of materials by inhibiting microbial growth. Literature surveying the electrodeposition of Cu-Ni incorporated with nano- to micro- particles to produce metal matrix composites has been reviewed. Also, a novel flow cell design for the enhanced deposition of metal matrix composites was examined to obtain the optimal oriented structure of the layered silicates in the metal matrix. With the addition of montmorillonite into the Ni and Cu-Ni matrix, an increase in strength, adhesion, wear and fracture toughness of the coating occurs, which leads to an increase corrosion resistance and longevity of the coating. These coatings were evaluated for composition and corrosion using many different types of instrumental and electrochemical techniques. The overall corrosion resistance and mechanical properties were improved with the composite films in comparison to the pure metals, which proves to be advantageous for many economic sectors including the oil and gas industry.

ACKNOWLEDGEMENTS

Through the journey of getting my PhD in Analytical Chemistry, I have encountered several people I would like to thank. First, I would like to thank the University of North Texas for accepting me into graduate school. All of the faculty in the Chemistry Department from the office personnel to the professors, I want to thank you for your constant help and support.

I would like to thank my advisor, Dr. Teresa Golden, for the opportunity to work in her research group in which you have provided me with continuous guidance and mentorship through my research and dissertation. Dr. Nandika D'Souza, thank you for generously offering me the opportunity to collaborate in this research and utilize your lab. I would like to thank Dr. Adel Mohamed from Qatar University for the chance to collaborate and provide research support. Thank you to Dr. Oliver Chyan and Dr. Francis D'Souza, who took the time to be a part of my dissertation committee along with reading and offering input into my dissertation. Also, much thanks to Dr. Yahia Ahmad from Qatar University for co-working with our research team and to my entire research group, especially Michael Hashe, Margaret Calhoun, Josey Tientong, Ryan Daugherty, and Heidi Conrad, for their support and helpful discussions.

This work was made possible by NPRP grant 4-306-2-111 from the Qatar National Research Fund (A Member of The Qatar Foundation).

Lastly, but most of all I would like to thank my family. We took on getting my PhD together as a family and without their unconditional love and support I would not of made it this far. To my four children, I want to thank you for your loving hugs and surprises when I got home every day; this kept me motivated to reach my dream of obtaining a PhD. And finally, to my loving wife and best friend, Whitney, thank you from the bottom of my heart for being unselfish in this process and providing constant positive support.

TABLE OF CONTENTS

Page

LIST OF TABLES

Page

LIST OF ILLUSTRATIONS

Page

CHAPTER 1

INTRODUCTION TO CHAPTERS

Corrosion is a phenomenon that leads to the degradation of metal components through a process of electrochemical reactions. Unfavorable environments tend to accelerate the corrosion process leading to devastating repercussions across many economic sectors. Particularly, corrosion presents an ever-growing problem to infrastructure, particularly in environments where existing bare steel is ineffective. Corrosion can be curbed by five basic approaches which include the selection of materials, chemical inhibitors, a change in the environment, cathodic protection, or coatings. Composite corrosion coatings that increase hardness and slow the rate of corrosion at a reduced cost have been heavily studied.

The off-shore oil rigs in the ocean are exposed to highly corrosive spray zones and low flow submerged components. For use in these marine environments, copper alloys are used to defend against biofouling of materials by inhibiting microbial induced corrosion (MIC). Copper ions are able to eliminate bacteria, viruses, fungi, algae and other microbes. Copper alloys have been examined due to their increased feasibility, material strength, and cost as compared to pure copper coatings. The two major copper alloys that are most commonly examined are Cu-Ni 90-10 and Cu-Ni 70-30. 90-10 Cu-Ni coatings show good protection in more stagnant conditions, whereas the 70-30 Cu-Ni coatings are employed in higher flow conditions because of the increased hardness provided by the higher concentration of nickel. Copper alloys are usually employed when long term durability is needed.

Electrodeposition of different metals and alloys has become popular for corrosion resistance and hardness in the oil and gas industry because of the major problems that persist with

corrosion. Electrodeposition has become a popular technique to produce new materials for science and engineering applications. The technique has become favorable in synthesizing coatings because of low cost, convenience, and the ability to work at low temperatures. Also, electrodeposition provides good advantages including accurate control of film thickness, the ability to upscale into an industrial setting, and it allows for uniform coating of large oddly shaped samples. Synthesizing alloys such as Ni-Mo, Zn-Ni, and Cu-Ni is important to increasing the corrosion resistance. The alloyed coatings tend to enhance the corrosion resistant properties but possess mechanical properties that compare to the individual metals. Nanoparticles such as TiO_2, CeO_2, SiC, and Al_2O_3 have been incorporated into the matrix of different coatings to enhance lifetime and performance of the coating.

Layered silicates are the ceramic compounds being analyzed in this study, which hold many lucrative properties such as a high surface area, good chemical resistance, resistance to extreme temperatures, and resistance to changes or extreme pHs. Scientists have been able to prove that layered silicates improve the resistance to corrosion when it comes to conductive polymer composite coatings, scientists have proved that layered silicates increase the resistance to corrosion. For this study, the addition of montmorillonite (MMT) into the Ni and Cu-Ni matrix helped produce an increase in strength, adhesion, wear and toughness of the coating, which lead to an enhanced corrosion resistance and hardness. As the accessibility of nanoparticles continues to increase, the interest in reduced cost and low temperature electrodeposited metal matrix composites will continue to rise.

The Ni-MMT and Cu-Ni-MMT coatings were analyzed with many different instrumental and electrochemical techniques. Scanning electron microscopy (SEM) was chosen to analyze the morphology of the electrodeposited films. X-ray diffraction (XRD) was used to analyze the crystal

structure and particle size of the films. The copper to nickel metal ratio was determined using atomic absorption spectroscopy (AAS) and the presence of the clay in the films; silicon and alumina was confirmed with energy dispersion x-ray spectroscopy (EDX). The corrosion resistance and mechanical properties of the films were analyzed using Tafel polarization, immersion tests, impedance spectroscopy, shear adhesion, and microindentation. Also, solution studies were performed with zeta potential and particle size to determine the optimum amount of loading for MMT into the Cu-Ni films.

In this dissertation, the following issues are addressed:

i. Compositional control of electrodeposited Cu-Ni coatings.
ii. The effect of MMT on the solution phase, electrodeposition process and crystalline phase of a pure metal and alloy matrix.
iii. The enhancement of the corrosion protection and mechanical properties with the addition of MMT into the metal matrix.
iv. The effect of flow cell deposition on the structure and properties of Ni-MMT coatings.

Chapter 1 introduces the research project. Chapter 2 explains the corrosion phenomena, the effects of corrosion on society and the oil and gas industry, and mitigation processes. Chapter 3 covers the compositional control of Cu-Ni coatings and background on metal matrix composites. Chapters 4 and 5 discuss the improvement of the mechanical properties and corrosion protection seen by adding MMT into the 70-30 and 90-10 Cu-Ni matrix. Chapter 6 covers the effects of using a novel flow cell design for the electrodeposition metal matrix composites. Lastly, Chapter 7 covers the overall results and future work.

CHAPTER 2

THE CORROSION PHENOMENA

2.1 Corrosion in Society

In 2013, the cost of corrosion weighed a heavy burden of over 276 billion dollars on the United States or about 3.1% of the GDP [1]. Figure 2.1, shows the breakdown of the corrosion costs for each of the major economic sectors. Industrialized societies are built around metals. Metals are used in every major economic sector in such areas as cars, planes, bridges, electronics, buildings, storage tanks, pipeline, bone replacements or repair, coins, and jewelry. Steel is the metal of choice for most industries due to low cost and good mechanical properties, but the major problem is that it tends to easily corrode. Corrosion deteriorates the properties of the metals leading to failure and fatigue. Society is confronted with a choice to both confront and control corrosion or to allow infrastructure to fail. There are four main reasons corrosion needs to be addressed and further studied [2]:

i. The safety of human life.

ii. The cost associated with corrosion.

iii. The conservation of precious materials.

iv. Learn the mechanisms of corrosion to learn how to better mitigate the problem.

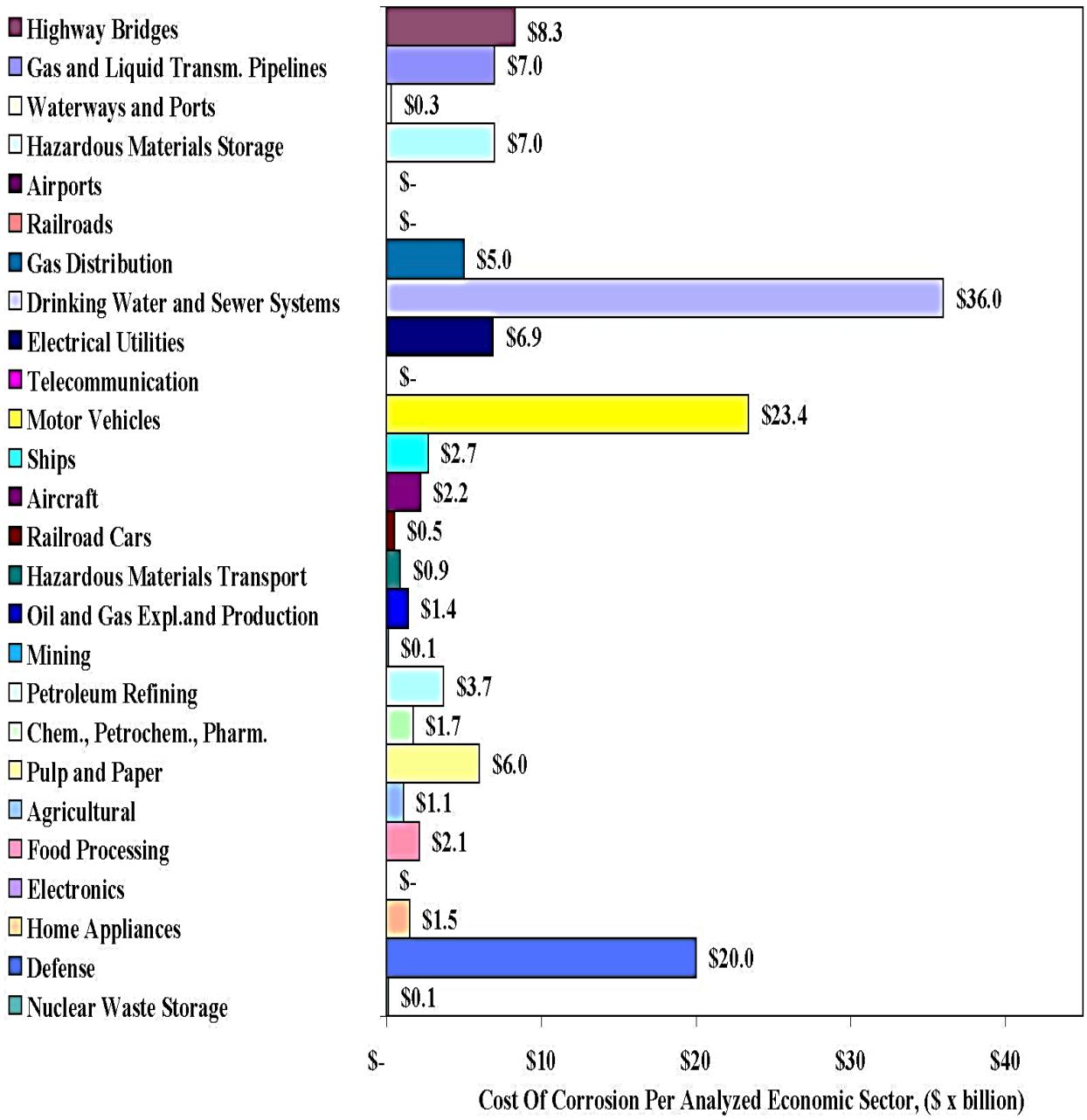

Figure 2.1: Cost of corrosion per major economic sector in 2002 [1].

2.2 Corrosion in the Oil and Gas Industry

In the oil and gas industry in the United States, it is estimated that about $1.4 billion dollars is spent on corrosion maintenance each year [1]. Breaking down the total amount, this accounts

for $589 million in surface pipeline and facility costs, $463 million in down hole tubing expenses and $320 million in capital expenditures related to corrosion [1]. The critical need for coatings in the oil and gas industry as a whole with both on shore and offshore can be seen in Figure 2.2. The off-shore (Figure 2.2A) cost of coatings encompasses about 70% of overall spending and on-shore (Figure 2.2B) comprises of 32.7%. Also, refineries (Figure 2.2C) see a cost of about 50% for coating, which proves coatings have become an issue with a high return rate [2].

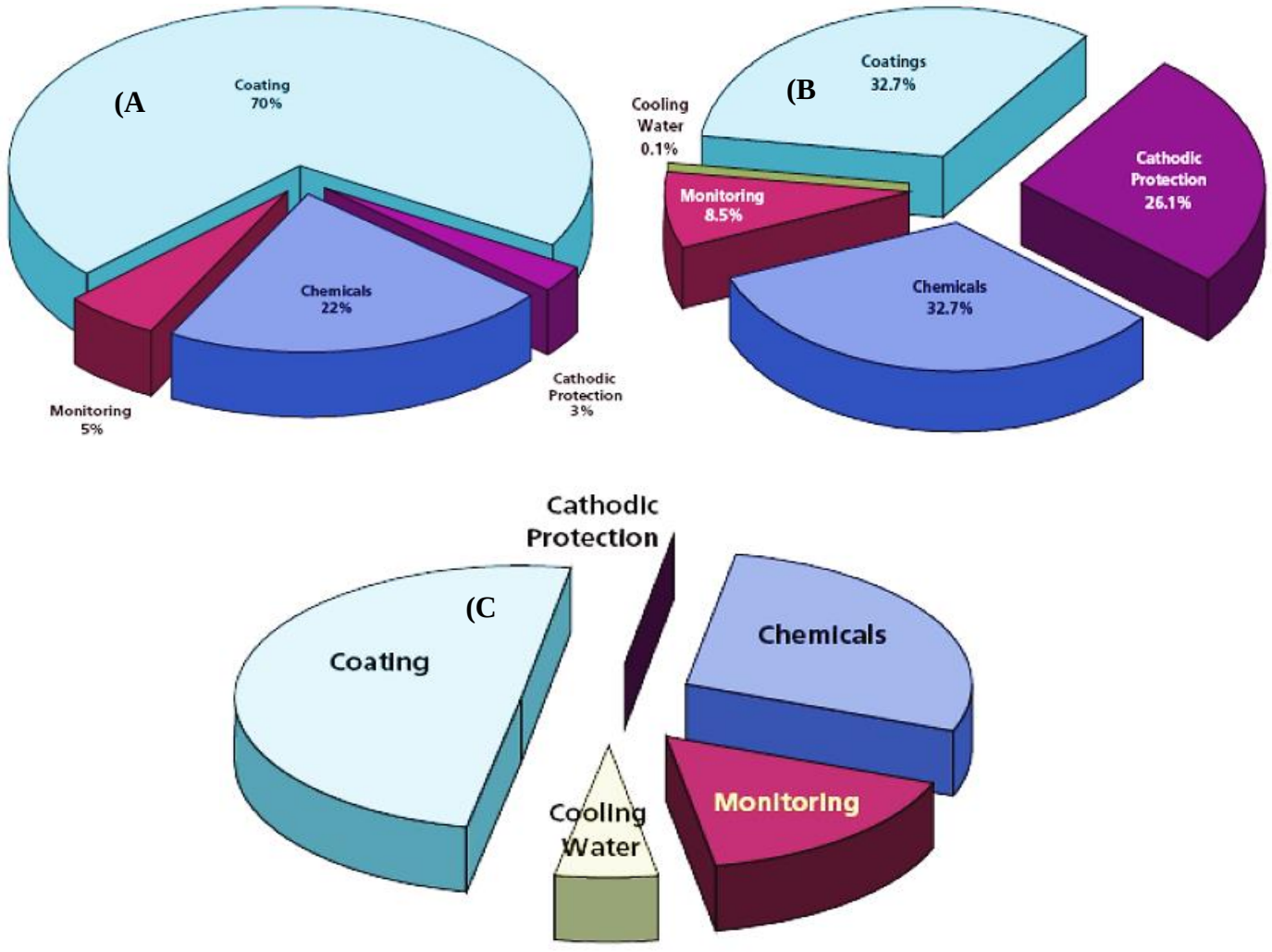

Figure 2.2: (A): Off-shore production for 1998 and 2001. (B): On-shore production for 2000 and 2001. (C): Relative percentage of direct cost for specific corrosion control technologies in refineries [3].

In the oil and gas industry, off-shore drilling structures undergo many different types of corrosion due to the various environmental exposures. Figure 2.3 represents common types of corrosion observed on an off-shore drilling rig in the oil industry. The most corrosive conditions are experienced in the splash zone. This area is located just above the high tide mark, and is constantly becoming wet and dry. Any protective coating applied to this area is repeatedly hit by the passing waves causing erosion corrosion. In this area, coating are applied at a higher thickness to account for the increased metal loss. The second area is the tidal zone, which is exposed to less severe conditions when compared to the splash zone. The tidal zone can be protected with cathodic protection systems. The remainder of the off-shore structure is protected by galvanic protection because of the lessening effect of flowing seawater. Another problem with the off-shore drilling rig is that water particulates, such as seawater and crustaceans often attach to submerged parts of the structure, adding weight which can lead to increased stress-related corrosion of the system. Low-frequency cyclic stress, which results from features such as waves, tides and operating loads, allows time for corrosion within cracks as they form. Understanding, modeling, and accounting for these stress areas are important factors for overall corrosion mitigation [4]. 70-30 Cu-Ni coatings reinforced with montmorillonite (MMT) have been created to be employed in the splash zones where the erosion corrosion is at the highest, which can be found in chapter 4. 90-10 Cu-Ni strengthened with MMT coatings were prepared to protect the lower flow submerged components from microbial induced corrosion, which can be found in chapter 5.

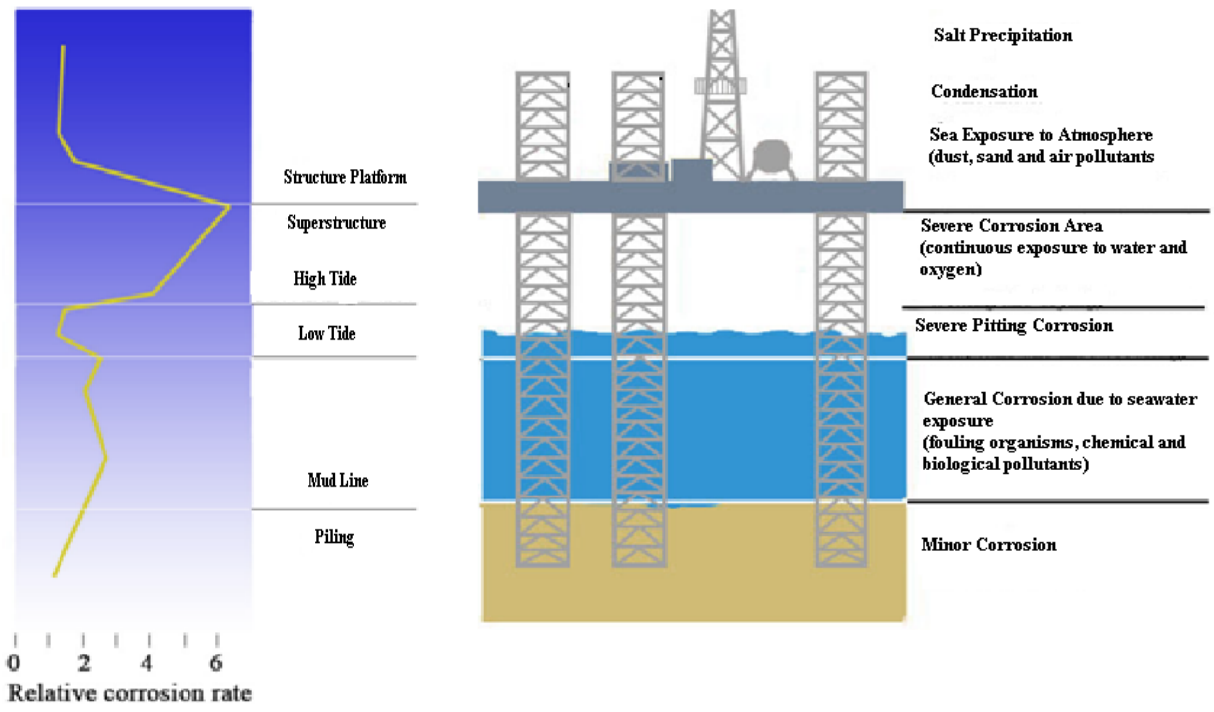

Figure 2.3: Off-shore structure demonstrating common corrosion occurrences [4].

2.3 Basic Corrosion

Corrosion takes place when there is a change in the property of a metal or a deterioration of the metal occurs [5]. The corrosion occurs because reactions with its surroundings and becomes the head of the problem in every stage of the oil and gas industry [5]. The presence of an anode, cathode, electrolyte (environment) and an electrical circuit that connects the cathode to the anode is required for corrosion to occur. The corrosion current enters the electrolyte and flows to the cathode causing dissolution to occur at the anode [6]. The general reaction occurring is as follows:

$$M \rightarrow M^{n-} + e^{n-} \qquad (2.1)$$

Where M = metal involved

n = valence of corroding metal species

e = # of electrons

Oxidation occurs at the anode surface. Electrons lost at the anode flow through the metallic circuit to the cathode, allowing cathodic reaction(s) to occur [6]. The reactions are dependent upon the environment of the material. In alkaline and neutral aerated solutions, the prevalent cathodic reaction is:

$$O_2 + 2H_2O + 4e^- \rightarrow 4OH \quad (2.2)$$

In de-aerated acids, the principal cathodic reaction is:

$$2H^- + 2e^- \rightarrow H_2 \quad (2.3)$$

In aerated acids, the cathodic reaction predominates:

$$O_2 + 4H^- + 4e^- \rightarrow 2H_2O \quad (2.4)$$

The number of electrons lost at the anode is equal to the number of electrons gained at the cathode [6]. In this system, we are trying to control the corrosion of stainless steel, whose main components are iron, nickel, and chromium. Iron naturally corrodes to an iron oxide species over time, seen in Figure 2.4. When iron is exposed to aerated, corrosive water, the anodic reaction can be represented as:

$$2Fe \rightarrow 2Fe^{2+} + 4e^- \text{ (anodic reaction)} \quad (2.5)$$

The accompanying reduction reaction of this system is the reduction of oxygen at the cathode:

$$O_2 + 2H_2O + 4e^- \rightarrow 4OH^- \text{ (cathodic reaction)} \quad (2.6)$$

The overall oxidation-reduction reaction for the corrosion of iron is:

$$2Fe + O_2 + 2H_2O \rightarrow 2Fe^{2+} + 4OH^- \quad (2.7)$$

Once dissolution has occurred, the ferrous ions commonly oxidize further to ferric ions. The ferric ions are able to combine with hydroxide ions which have been formed at the cathode, resulting in the corrosion product commonly known as rust (Fe_2O_3).

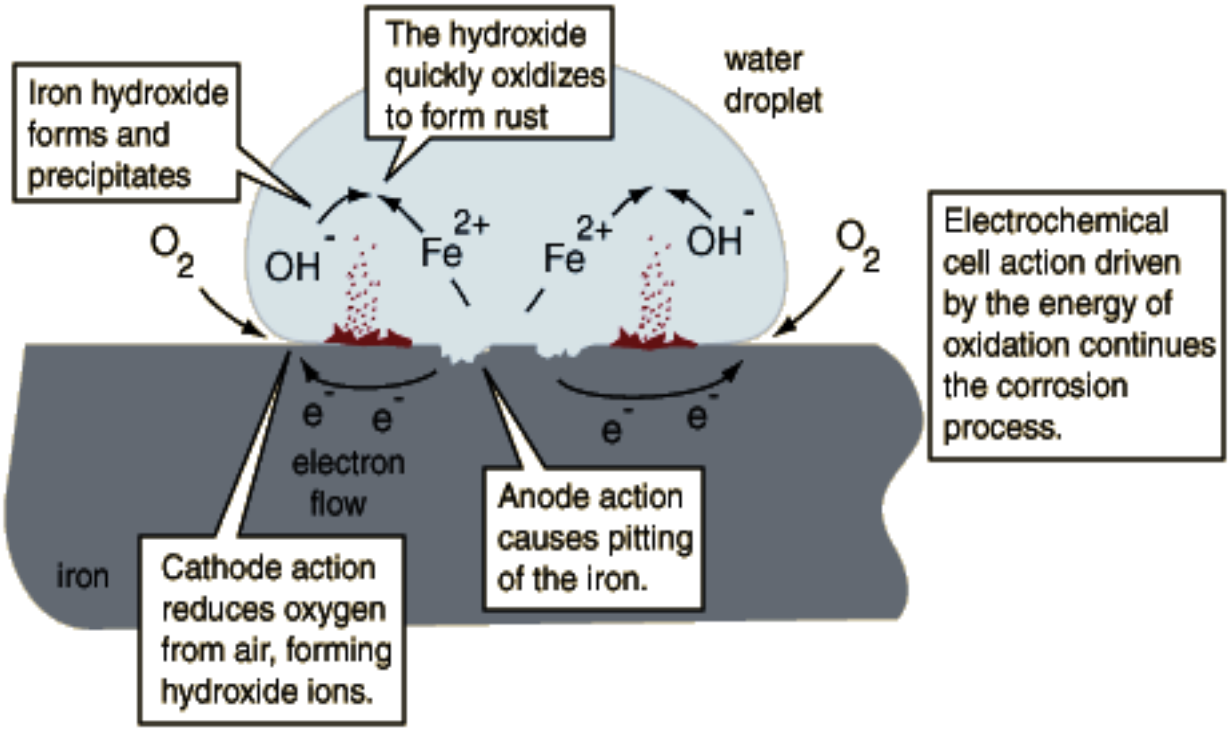

Figure 2.4: The corrosion mechanism for the formation of red rust.

2.4 Types of Corrosion

There are two different categories of corrosion to be evaluated when looking at films for corrosion resistance, which are general and localized corrosion. General uniform corrosion comprises of anodic dissolution occurring across the surface of a metallic film in uniform manner. Localized corrosion encompasses eight main different types of corrosion including pitting, crevice, galvanic, intergranular, de-alloying, erosion, stress cracking, and microbial induced corrosion [6].

2.4.1 General Uniform Corrosion

General uniform corrosion happens when the thickness loss of the coating happens uniformly over the entire surface of the coating. This is known to be the least dangerous form of

corrosion because the thickness loss can be predicted mathematically and with simple experiments to know when a failure is going to occur over time. Also, this is the most common type of corrosion. Iron is one such metal that is vulnerable to this type of corrosion because it does not have a passivating nature [7].

2.4.2 Pitting Corrosion

Seen in Figure 2.5, pitting corrosion is one of the more monitored types of corrosion and is heavily observed for aluminum and steel in the presence of corrosive anions such as SO_4^{2-} and Cl^-. This type of corrosion is described as small pits that initiate at the surface of a metal in a corrosive media. The pitting starts with the adsorption of corrosive anions onto the surface of the metal, which starts to break down the protective oxide layer. The adsorption of the anions leads to an increase in the ion conductivity in the metal-oxide layer, which allows the metal ions from the bulk to migrate to the surface initiating the corrosion process. Over time the passive oxide layer undergoes thinning in localized areas, which leads to the creation of a pit. As the metal ions move towards the surface of the pit, the ions react with OH^- ions produce from the cathodic reaction, which forms metal-hydroxide precipitates that cover the pit. With the corrosion products covering the pits, corrosion starts to take place at an even faster rate because the products covering the pit do not allow for the exchange of the electrolyte leading to an even more corrosive acidic environment. The pits have been known to grow from a range of a few nanometers to several microns [7].

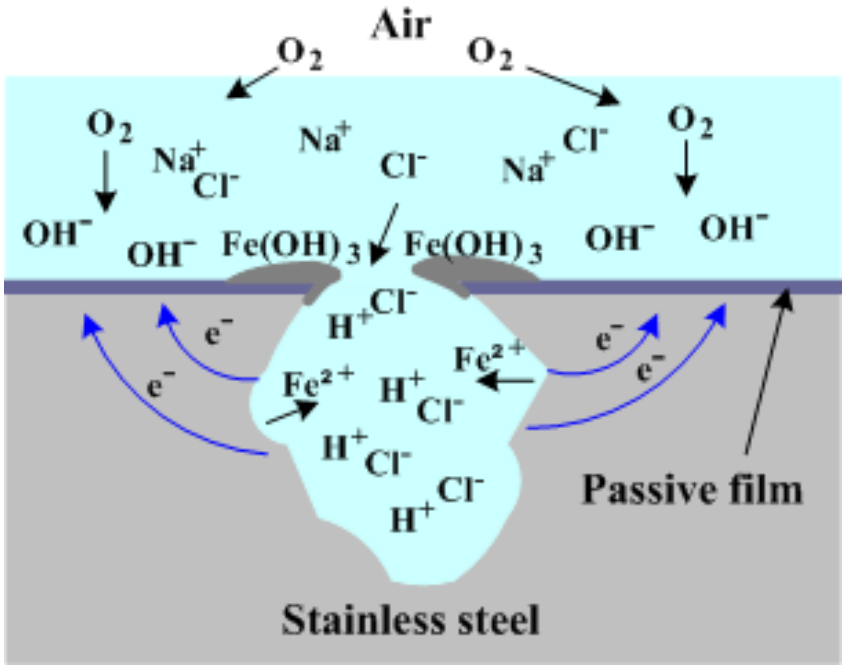

Figure 2.5 Schematic illustrating pitting corrosion.

2.4.3 Crevice Corrosion

Crevice corrosion takes places in areas beneath deposits and in small crevices that have low amount of oxygen present. With low amounts of oxygen present in these environments, the protective oxide layer has difficulty forming, which inhibits the metals natural ability to defend against corrosion. Crevice corrosion starts in a small fissure that is just large enough for liquid to penetrate but too small for liquid to flow. The oxygen in the crevice starts to be consumed inside the fissure faster than the oxygen is transported into the space. The OH^- can no longer be produced as the oxygen becomes completely consumed. Although, the metal dissolution inside the fissure remains because of the oxygen reduction reaction still proceeding outside of the crevice. With the formation of OH^- ions severely hindered, the increased amount of metal ions react with negative anions, such as Cl^-, to maintain electrical neutrality. The metal salts then react with water which creates metal hydroxides that are deposited onto the surface of the crevice and acids, such as HCl. The acid causes the local pH in the crevice to drop between 0-4, whereas the pH outside the crevice

is 9-10, which cause severe corrosion to take place [7]. These crevices are usually created from normal mechanical construction such as sharp corners, spot welds, lap joints, fasteners, flanged fittings, couplings, threaded joints and tube sheet supports [6]. Figure 2.6 displays a schematic for the formation of crevice corrosion.

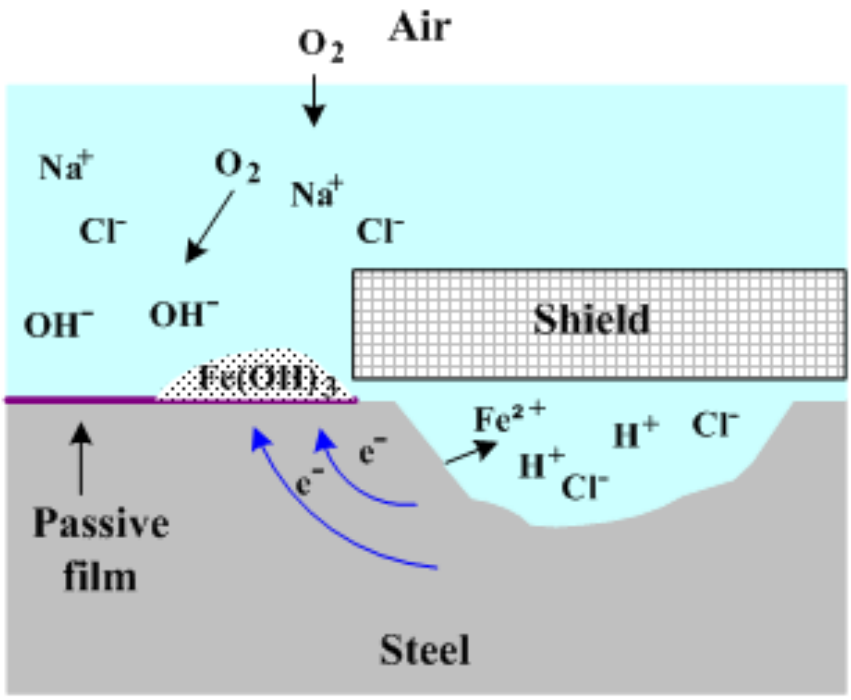

Figure 2.6: Schematic displaying crevice corrosion.

2.4.4 Galvanic Corrosion

Galvanic corrosion is defined by a contact made by two dissimilar metals, which means that one metal is nobler than the other. Also, an electrolyte needs to be present in between the two metals to complete the circuit. A very crucial factor in this type of corrosion is the area ratio of the cathode to the anode. So, if the less noble metal possess a small amount of surface area and the nobler metal maintains a large surface area, the cathodic reaction will be large which needs to be balanced by a large anodic reaction. This produces an increased anodic reaction rate, which in

turn leads to higher corrosion rates because of an increase in metal dissolution. This means that the ratio of cathode size to anode size needs to be kept small [7]. Galvanic corrosion can be disrupted if the electrical contact between the two metals is disrupted, such as with plastic insulators [6]. The galvanic series in seawater seen in Figure 2.7 helps to determine how galvanic corrosion would proceed between certain metals in this environment at 25°C. Simulated seawater at 25°C was the testing solution used in this research.

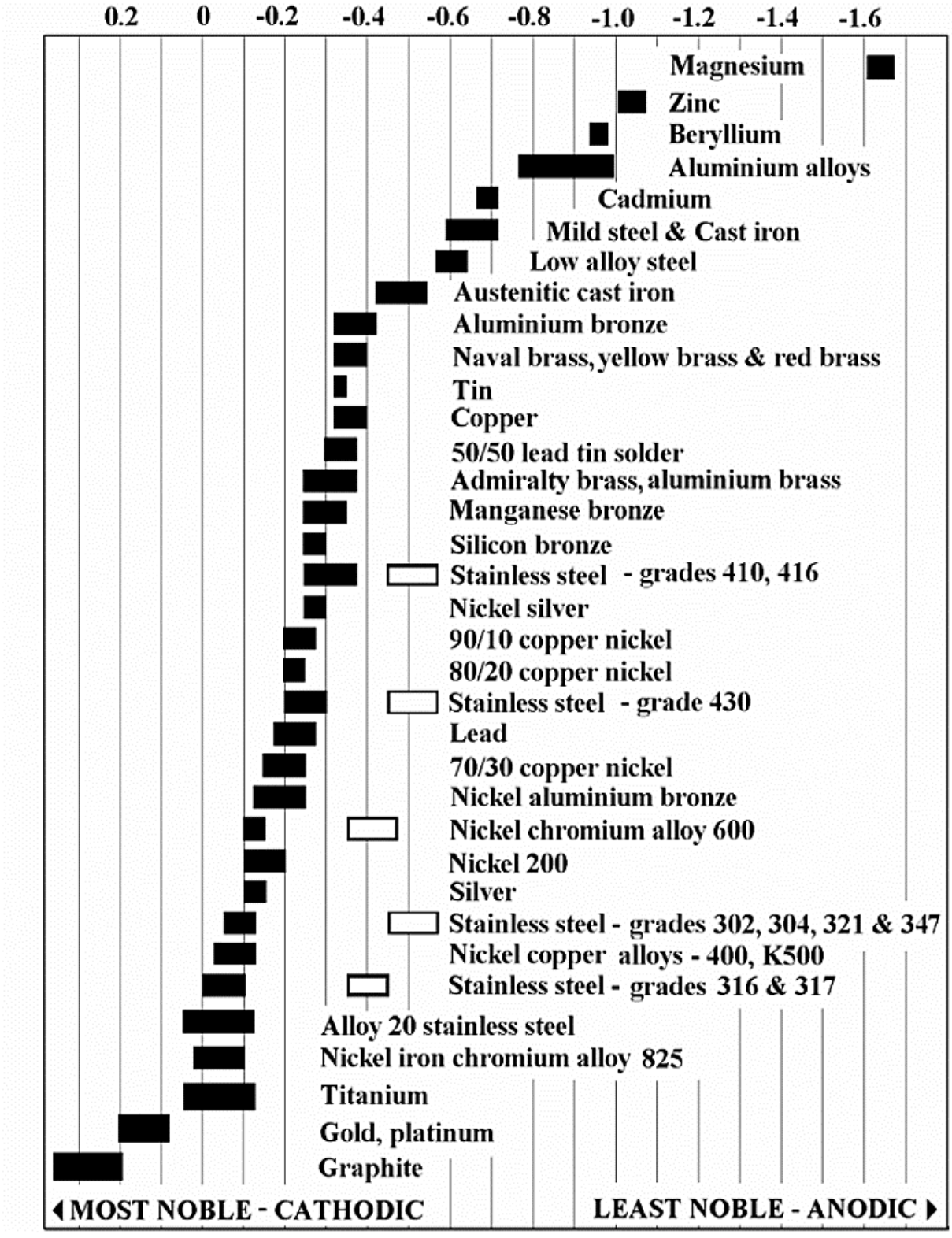

Figure 2.7: Galvanic series for metals in seawater at 25°C.

2.4.5 Intergranular Corrosion

Intergranular corrosion is also a localized form of attack in where the attack takes place in the structure of the material, with little to no corrosion occurring on other parts of the surface. This is caused by a difference in the concentration of the alloyed metals, which create galvanic elements. This usually occurs at the grain boundary when there is a cluster of a less noble metal that starts to act as an anode and the nobler part of the surface acts as the cathode. This leads to the area ratio between the cathode and the anode being quite large, which leads to very high corrosion rates [7]. Welding, stress relief annealing, improper heat treating and overheating can cause small compositional differences, which create an area of susceptibility to intergranular corrosion in the material. The onset of intergranular corrosion can be prolonged by avoiding sharp corners and stagnant areas in the design of the material, using sealants in the material, use welds in place of bolts or rivets, and selection of corrosion resistant materials prior to the creation of the system [6].

2.4.6 De-alloying Corrosion

De-alloying corrosion occurs when one of the elements in an alloy is extremely less noble than the other elements. This results in the less noble metal being completely removed and the material being left in a porous state with drastically reduced mechanical properties. The issue becomes that the material maintains it shape and physical appearance because the corrosion products that form precipitate out onto the surface, which makes this type of corrosion difficult to spot [7].

2.4.7 Erosion Corrosion

Erosion corrosion takes place when a corrosive fluid is moving over a submerged metal substrate. This leads to the surface metal being exposed to wear, which in turn cleans the surface of the metal leading to a more active metal surface. Copper and steels tend to undergo this type of corrosion because their protective oxide layer are only loosely adherent to the surface of the bulk metal, so as the flow increases their protective layer is removed leading to much higher corrosion rates [7].

2.4.8 Stress Cracking Corrosion

Stress cracking corrosion is induced when a crack forms from the effects of a constant load being placed on a certain point on the structure and corrosion taking place in the same instance. This tensile stress may be due to centrifugal forces, temperature changes, welding, and external loads. The cracks tend to form in planes normal to the stress and may branch out intergranularly [7].

2.4.9 Microbial Induced Corrosion

Microbial induced corrosion (MIC) occurs when biological organisms create the flow of electrons, which results in a change in the local environment becoming more corrosive in nature. This happens when small microbial organisms accumulate on the surface of a metal. As the colony of bacteria grows on the surface, the underside becomes the anode and the surface outside the colonized area becomes the cathode. Dissolution of metal will ensue under the colony and resemble that of pitting corrosion, except that the density of the dissolution will match closely to the density of the colonized bacteria. Some microbial colonies also produce byproducts such as

inorganic and organic acids, which change the local pH to more acidic conditions leading to even higher corrosion rates. Also, the production of inorganic acids leads to the formation of the hydrogen ion, which causes problems with hydrogen embrittlement in the colonized areas. In anaerobic environments, sulfate reducing bacteria reduce the sulfate ion, which forms the sulfide ion and oxygen. Ferrous ions then react with the sulfide ions, which further causes dissolution of metal from the metal surface [7]. Figure 2.8 shows the corrosion of iron by sulfate reducing bacteria (SRB). Step 1 illustrates the dissolution of iron, step 2 shows the dissociation of water into OH^- and H^+ ions, step 3 displays the reduction of protons, step 4 demonstrates the reduction sulfate by the bacteria, and step 5 presents the precipitation of the iron sulfide.

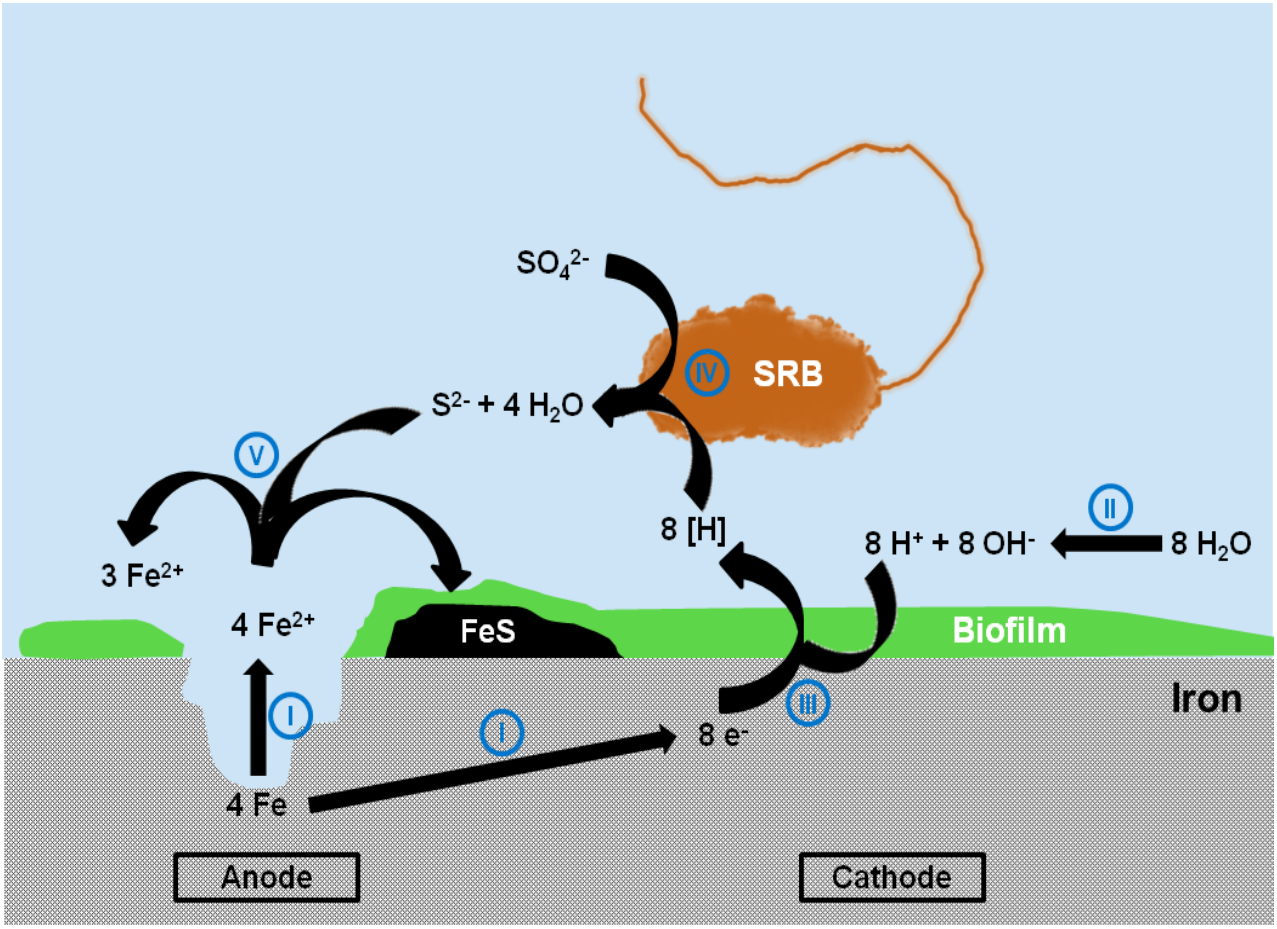

Figure 2.8: Microbial induced corrosion of iron.

Although, the overall electrochemical nature of corrosion holds true for MIC, the incorporation of microorganisms generates several unique features, the most noteworthy being the modification of the metal-solution interface by the formation of a biofilm. A biofilm is an aggregation of microorganisms growing on a solid surface. It is a gel-like substance containing ≥95% water with a matrix of exopolysaccharidic substances (EPS) with suspended microbial cells and inorganic detritus [8]. The formation of this biofilm affects the electrochemical processes occurring at the electrode-electrolyte interface. The treatment of the biofilm holds the key to the inhibition of corrosion [8].

The formation of the biofilm occurs through an accumulation process beginning immediately after metal immersion in an aqueous environment [8, 9]. During the first stage, a thin film (20-80nm thickness) is formed from the deposition of inorganic ions and organic compounds of higher molecular mass. This initial film formation can alter the electrostatic charges and wettability of the metal surface, which aids in further helping bacteria colonize. Microbial growth and EPS production result in the biofilm development. The biofilm is a dynamic system, with the various transport processes and chemical reactions occurring at the biofilm interface extending through the biofilm thickness [8].

For MIC, the coatings being examined are copper and copper alloys. Copper exhibits antimicrobial properties, which can aid in MIC resistance. Commonly, copper and copper-nickel alloys are used for MIC resistance. For copper and copper-nickel alloys, copper affects the biofilm, leading to inhibition of microbial corrosion. The top layer of the initial coating upon submersion into seawater is a fresh copper-nickel surface, which is vulnerable to biofouling. During the initial stages of the exposure, the biofouling resistance of the alloy is controlled through the dissolution of copper ions from the alloy into the surroundings. After exposure to seawater, a weakly adherent

copper oxide layer starts to form on the surface of the alloy. The copper oxide layer is also susceptible to biofouling but is also easily removed preventing large colonization of microorganisms. The remaining freshly exposed film stays adherent to the underlying metal surface and starts to regenerate a new copper oxide layer [8].

The natural corrosion process of copper alloys is subdivided into primary and secondary reactions. A copper oxide film is formed during the primary reaction (Figure 2.9). The anodic reaction occurs at the metal-oxide interface and the cathodic reaction at the water-oxide interface. The copper oxide film is not a dense layer, so the copper-nickel alloy is continuously releasing small amounts of copper ions into the copper oxide layer. These ions are detrimental to many microorganisms, so the biofilm formation rate is significantly decreased.

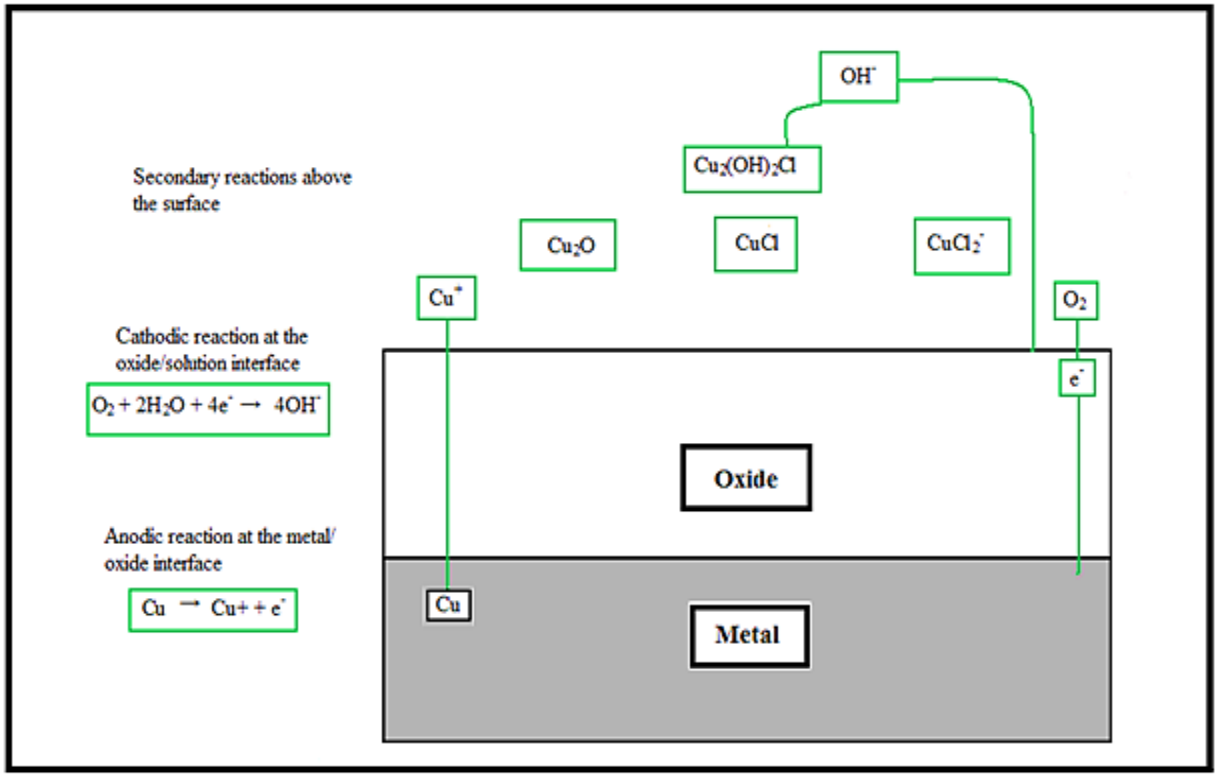

Figure 2.9: Primary and secondary copper alloy reactions [9].

2.5 Corrosion Mitigation

Corrosion mitigation is the reduction of metal damage and loss due to corrosion through the use of protective methods. Since corrosion cannot be completely eliminate, a good economic idea would be to manage the rate at which corrosion occurs. Corrosion can be curbed by five basic approaches which include the selection of materials, chemical inhibitors, a change in the environment, cathodic protection, and coatings [6]. Coatings tend to be one of the most popular choices especially in open environments. Corrosion resistant materials used in coatings can be broken down into four basic components which include metals, ceramics, polymers, and composites [10]. Figure 2.10 shows a bar graph of the amount of patents that were produced in each of these areas from 2005-2009 [10]. Metal and composite coatings show to be favored over their counterparts and are the focus of this work. Although many different methods are used to create protective coatings, such as chemical vapor deposition, physical vapor deposition, screen printing, dip-coating, thermal spraying, sputtering, immersion, welding and roll coating; this work focuses on the electrodeposition of metal matrix composite (MMC) coatings.

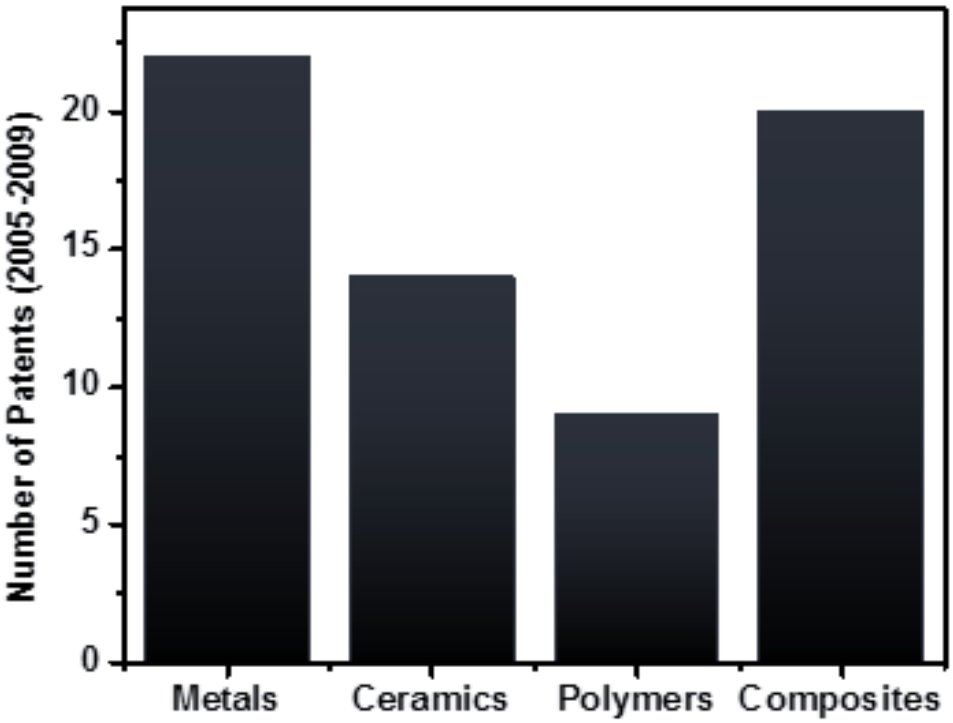

Figure 2.10: The amount of patents for corrosion resistant coating materials from 2005-2009 [10].

One metal typically used to enhance corrosion resistance is nickel because of its high abundance and capability to protect against common types of corrosion [11, 12]. Pure nickel shows a coating-lost/corrosion rate of 45μm per year [13]. Nevertheless, corrosion resistance from pure metal coatings tend to be unsuccessful because of reduced mechanical properties, such as a hardness of 200 HV observed for pure nickel [13]. Forming alloys seems to be the answer to increasing the corrosion resistance with such metals as zinc [14], molybdenum [15], and copper [16]. Alloys have different corrosion potentials than their single elements; therefore, by picking the correct combination of alloys, one can greatly increase the corrosion resistance of the material [17]. Cu-Ni alloys have shown an increased coating-lost/corrosion rate (12.95μm per year) versus pure nickel films [18]. The alloyed coatings tend to enhance the corrosion resistant properties but possess mechanical properties that compare to the individual metals.

Ceramic fortification into the metal coatings can improve mechanical and corrosion properties. Ceramic particles such as SiO_2 have been infused into a nickel matrix and have shown an increased coating-lost/corrosion rate of 37.85µm per year [19], and they also show an increase in hardness to 360 HV [13B]. Also, to increase the hardness and life of nickel coatings, different nanoparticles such as TiO_2, CeO_2, SiC, and Al_2O_3 have been integrated into the matrix of the coating creating nanocomposite films [13, 21-23]. Metal-oxides have valuable properties such as increased mechanical strength, high temperature creep strength, and wear resistance [24]. Metal-oxides tend to show enhanced corrosion resistances with a nano sized grain [24]. Al_2O_3 nanoparticles dispersed into nickel have shown coating-lost/corrosion rates of 5µm per year and hardness values of 545 HV [25]. Work has been done where clays, such as MMT were incorporated into a nickel matrix for better wear and corrosion resistance [26-29]. In this work, MMT is embedded into the Cu-Ni matrix and evaluated for corrosion protection and mechanical properties, which is further discussed in Chapters 3-5. Also, a novel designed flow cell for the electrodeposition of MMC coatings was created to help orient the MMT in the coating to help further increase the mechanical properties and the corrosion protection, which is discussed in Chapter 6.

2.6 References

[1] "Corrosion in the oil and gas industry," 2013. http://www.nace.org/Corrosion-Central/Industries/Oil---Gas-Production/

[2] E. McCafferty, “Introduction to corrosion science” New York: Springer, 2010.

[3] R. Tems, A.M. Al-Zahrani. "Cost of corrosion in oil production and refining," Saudi Aramco Journal of Technology, pp. 2-14, 2006.

[4] D. Brundel, R. Edwards, A. Hayman, D. Hill, S. Mehla, T. Semerad, Oilfield Review, pp. 4-69, 1994.

[5] D. Brondel, R. Edwards, D. Hill, S. Mehta, T. Semerad, "Corrosion in the oil industry," 1994.

[6] Army Publication: EM 1110-2-3400, Corrosion theory and corrosion protection. Ch. 2, 1995.

[7] V. Cicek, B. Al-Numan, "Corrosion chemistry". Wiley-Scrivener, 2012.

[8] H.A. Videla, L.K. Herrera, "International microbiology," 8, pp. 169-180, 2005.

[9] Copper Development Association, Inc, Information on Copper and its alloys, http://www.copper.org, 2012.

[10] Corrosionist, http://www.corrosionist.com/, 2012.

[11] W.Z. Friend, Corrosion of nickel and nickel-base alloys. New York: Willey-Interscience, 1980.

[12] Y.Y. Chang, D.Y. Wang, "Corrosion behavior of electroless nickel-coated AISI 304 stainless steel enhanced by titanium ion implantation," Surface Coating Technologies, vol. 200, pp. 2187-2195, 2005.

[13] R. Sen, S. Das, K. DAS, "Synthesis and properties of pulse electrodeposited Ni-CeO_2 nanocomposite," Metallurgical and Materials Transactions A, vol. 43A, pp. 3809-3823, 2012.

[14] H.A. Conrad, J.R. Corbett and T.D. Golden, "Electrochemical Deposition of γ-Phase Zinc-Nickel Alloys from Alkaline Solution," Journal of the Electrochemical Society, vol. 159, no. 1, pp. C29-C32, 2012.

[15] Y.H. Ahmad, J. Tientong, M. Nar, N. D'Souza, A.M.A. Mohamed and T.D. Golden, "Characterization and corrosion resistance of electrodeposited Ni-Mo-silicate platelet nanocomposite coatings," vol. 259, pp. 517-525, 2014.

[16] I. Baskaran, T.S.N. Sankara Narayanan, A. Stephen. "Cu–Ni alloy films and evaluation of their characteristic properties" Materials Letters, 60, pp. 1990–1995, 2006.

[17] N. Zaki. "Zinc-Nickel Alloy Plating," Metal Finishing, vol. 6, pp. 57-60, 1989.

[18] V.A.R. Boyapti, C.K. Kanukula. "Corrosion Inhibition of Cu-Ni (90/10) Alloy in Seawater and Sulphide-Polluted Seawater Environments by 1,2,3-Benzotriazole," ISRN Corrosion, pp.1-22, 2013.

[19] S. Kasturibai, G.P. Kalaignan. "Physical and electrochemical characterizations of Ni-SiO_2 nanocomposite coatings," Ionics, 2012.

[20] L. Yan, Y. Si-rong, L. Jin-dan, H. Zhi-wu, Y. Dong-sheng. "Microstructure and wear resistance of electrodeposited Ni-SiO2 nano-composite coatings on AZ91HP magnesium alloy substrate," Trans. Nonferrous Met. Soc. China, vol. 21, pp.483-488, 2011.

[21] W. Chen, Y. He, W. Gao, "Synthesis of Nanostructured Ni–TiO_2 Composite Coatings by Sol-Enhanced Electroplating," Journal of the Electrochemical Society, vol. 157, no. 8, pp. E122, 2010.

[22] L. M. Chang, J. H. Liu, R. J. Zhang, "Corrosion behaviour of electrodeposited Ni/Al2O3 composite coating covered with a NaCl salt film at 800 °C," Materials and Corrosion, vol. 62 no. 10, pp. 920-925, 2011.

[23] H. B. Temam, L. Zeroual, A. Chala, S. Rahmane, C. Nouveau, "Microhardness and corrosion behavior of Ni-SiC electrodeposited coatings," Plasma Processed Polymers, vol. 4, pp. S618–S621, 2007.

[24] R. K. Guduru, P. S. Mohanty. "Corrosion of metal-oxide systems," Corrosion Resistance. pp. 271-294, 2012.

[25] A. C. Ciubotariu, L. Benea, M. Lakatos–Varsanyi, V. Dragan, , "Electrochemical impedance spectroscopy and corrosion behaviour of Al2O3–Ni nano composite coatings," Electrochimica Acta, vol. 53, pp. 4557–4563, 2008.

[26] R.A. Horch, T.D. Golden, N.A. D' Souza, L. Riester "Electrodeposition of Nickel/Montmorillonite Layered Silicate Nanocomposite Thin Films" Chemistry of Materials, vol. 14, pp. 3531-3538, 2002.

[27] J. Tientong, C.R. Thurber, N. D'Souza, A.M.A. Mohamed, and T.D. Golden, "Influence of bath composition at acidic pH on electrodeposition of nickel-layered silicate nanocomposites for corrosion protection," Int. J. Electrochem. Vol. 2013 pp 1-8, 2013.

[28] J. Tientong, Y.H. Ahmad, M. Nar, N. D'Souza, A.M.A. Mohamed and T.D. Golden, "Improved mechanical and corrosion properties of nickel composite coatings by incorporation of layered silicates," Mater. Chem. and Phys. Vol. 145, pp. 44-50, 2014.

[29] Y.H. Ahmad, J. Tientong, N. D'Souza, T.D. Golden and A.M.A. Mohamed, "Salt water corrosion resistance of electrodeposited Ni-layered silicate nanocomposite coatings from Watts' Type Solution," Surf. Coat. Tech. vol. 242, pp. 170-176, 2014.

CHAPTER 3

ELECTRODEPOSITION OF COPPER NICKEL COMPOSITE COATINGS

3.1 Introduction

Copper alloys, such as Cu-Ni, have been studied because of their good electrical and thermal properties, machinability, and resistance to corrosion [1-4]. Copper is relatively soft and needs to be alloyed with another metal, such as nickel, to increase the hardness of the material [3, 5]. Also, with the addition of Ni into the Cu matrix during electrodeposition, it is possible to grow films with minimal strain due to both Cu and Ni having face-centered cubic crystal structures and similar lattice parameters [6]. The electroplating of copper alloy films has an instrumental role in many different industry related applications. For instance, electroplating has found a niche in microelectromechanical systems (MEMS) because the process can deposit different alloys onto depressed and oddly shaped geometric substrates [5, 7-9]. Cu-Ni coatings have been evaluated for use as inert anodes in the fabrication of aluminum because of their enhanced electrical and thermal conductivity [10-11]. In marine environments, copper alloys are used to defend against biofouling of materials by inhibiting microbial induced corrosion (MIC) [12-15].

Coatings can be produced by using several different approaches, and electrodeposition remains a prominent technique to produce novel materials for science and engineering applications. Electrodeposition also offers low cost, convenience, ability to work at low temperatures and the ease of application to complex geometries [16, 17]. Other advantages for using electrodeposition include the ability to quickly scale to an industrial setting, uniform coating of large samples, and accurate control of the coating thickness [18]. Other methods for producing MMCs include commercial pressing [19], laser cladding [20], hot pressing [21], plasma transferred-arc surfacing [22], stir casting [23], diffusion bonding [24], powder metallurgy [25],

and chemical vapor deposition [26]. Each of these methods have different advantages and disadvantages. However, some of the drawbacks include production at high temperatures or under vacuum, difficulty in controlling the thickness, and cost.

Metal matrix composite (MMC) coatings engineered using an electrodeposition method are examined in this chapter. The electrodeposition of a composite involves the electrolysis of plating baths where nano- to micro- sized particles are dispersed and various quantities of the particles become imbedded within the plated metal matrix providing special properties to the coating (Figure 3.1) [27]. The process of particle incorporation into metal coatings for electrochemical deposition can be simplified into four steps: (1) particles dispersed in solution form a surface charge, (2) from the bulk solution there is mass transport of the particles to the surface of the electrode typically through convection, (3) there is interaction between the particle and the electrode, (4) the particles become trapped within the growing metallic film [18]. The earliest example of electrodeposited composites dates back to the 1920s where Cu-graphite coatings were developed for automotive bearings [28, 29]. Enhanced corrosion, tribological, and mechanical properties were the main research focus of the automotive and aerospace industries in the 1970s-1990s leading to significant technological advancements. In the early 2000s, some of the focus started to shift to electrical components and electronic devices [7-11, 30]. As the accessibility of nanoparticles continues to rise, the interest in reduced cost and low temperature electrodeposited MMCs continues to escalate [18].

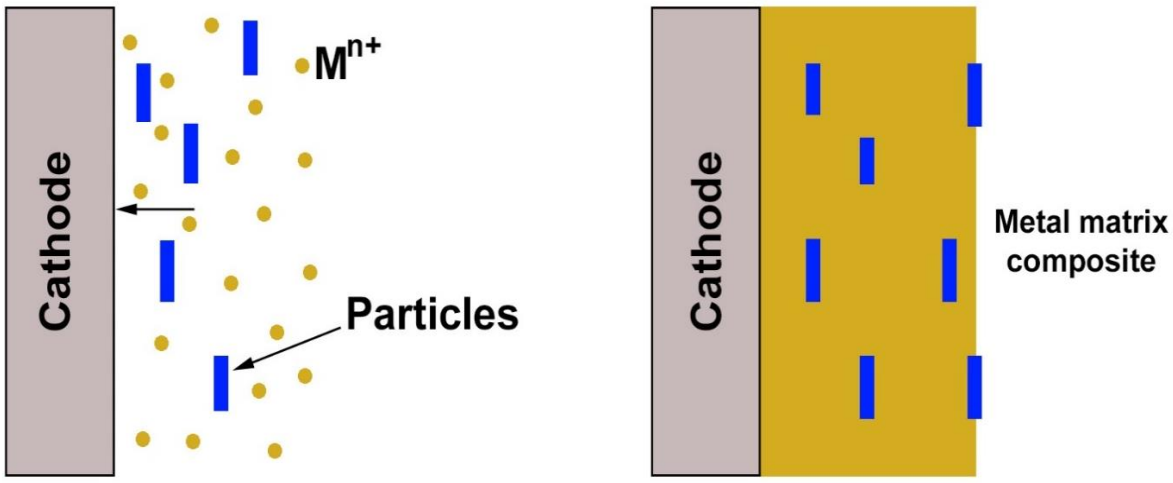

Figure 3.1: Schematic displaying the growth of MMCs by electrodeposition.

MMC coatings combine the advantageous properties of a pure metal and the embedded particle to produce a superior coating [31, 32]. An extensive amount of work has gone into examining copper-based MMCs [33-37] and nickel-based MMCs [38-42] since individual metals can exhibit a limited range of properties. An important route to improving the properties of individual metals is the deposition of alloys such as Zn-Ni, Ni-Mo, and Cu-Ni [43-45]. Successful incorporation of particles into the metal matrix by electrocodeposition relies on many different parameters, including the composition of the electrolyte, pH, current density, and properties of the particles [46]. Incorporating particles such as TiO_2, SiC, Al_2O_3, carbon fibers, Ni, Al, and Cr into the Cu-Ni matrix of different coatings enhances the electrical, mechanical, and corrosion properties of the coatings [7, 8, 10, 11, 30, 31, 47-50].

Understanding the incorporation of particles into these alloys requires mathematical modelling. Early models dating back to the 1960s from Williams and Martin [51] proposed that particles were transported to the cathode surface via a convection transport mechanism facilitated by stirring the plating bath. Brandes and Goldthorpe [52] hypothesized that entrapment by mechanical means was not the only factor at play and decided that an electrostatic force must be

aiding the inclusion of the particles into the metal matrix. In 1972, Guglielmi [53] became the first to propose a mathematical model that explained the inclusion of particles into the metal matrix. The model followed a simple 2 part approach: (a) the particles slowly move towards the surface of the cathode and adsorb very loosely, (b) then the particles become securely adsorbed by shedding their ionic cloud. The derived model equations are [40, 53]:

$$\frac{C(1-\alpha)}{\alpha} = \frac{Wi_o}{nFdv_o} e^{(A-B)\eta}\left(\frac{1}{k} + C\right) \tag{3.1}$$

$$i = (1-\vartheta) i_o e^{A\eta} \tag{3.2}$$

where C is the vol.% of particles in the electrolyte solution and α is the vol.% of particle incorporated in the composite film. W corresponds to the atomic weight of the metal in the coating, F is Faraday's constant, d is the density of the metallic coating, and n is the valence of the metallic coating. η relates to the overpotential, i is the current density, and i_o is the current density from the metallic coating. The υ term is a constant from the deposition of the particle, A is a constant from the deposition of the metal, and B is a constant from the particle inclusion. The ϑ relates to the coverage of the surface by the particle that is incorporated into the metal coating and k is the adsorption coefficient. Although the model has some holes, such as not taking into account the mass transport of the metal ions or the particles and the nature of the particle or the shape, it is still one of the most widely used models to date. In 1987, Celis et al. [54] hypothesized a new 5 part model, which built on the idea of Guglielmi's 2 part model. The drawback of this model is that factors need to be created that are specific to each individual system. As late as 2002, Bercot's group [55] proposed an addition to Guglielmi's original model that included a polynomial for the purpose of correcting for different effects presented by adsorption and flow.

A survey of the literature for the incorporation of particles into Cu-Ni coatings is shown in Table 3.1. The composite coatings described in Table 3.1 are for electrodeposited processing only.

Other Cu-Ni composites have been made using different techniques, but fall outside the scope of this chapter.

Table 3.1: A summary of the work produced on electrodeposited Cu-Ni composite coatings.

Group	Possible Applications	Deposition conditions	Composite	Ref
Panda et al.	Recessed microelectrodes for MEMS devices	1.0 M $NiSO_4 \bullet 6H_2O$ 0.04 M $CuSO_4 \bullet 5H_2O$ 0.3M $Na_3C_6H_5O_7 \bullet 2H_2O$ 3.125-12.5 g/L Al_2O_3 j = 2-50 mA/cm^2 26°C	Cu-Ni alloy incorporated with γAl_2O_3 (~30 nm)	7
Huang et al.	Magnetic Microactuators for MEMS Devices	200-250 g/L $CuSO_4 \bullet 5H_2O$ 45-90 g/L H_2SO_4 Plating rate: ~0.2 µm/min. 40°C	Cu incorporated with Ni nanopowder (~50 nm)	9
Chen et al.	Electrical and Electronics (Speakers)	alkaline noncyanide-based copper-plating solution 2-8.5 g/L Ni 40°C Stir rate: 250 rpm	Cu incorporated with Ni nanoparticles	8
Huang et al.	Electrical and Electronics (MEMS Devices)	120 g/L $Na_3C_6H_5O_7 \bullet 2H_2O$ 25 g/L H_3BO_3 12 g/L $NiCl \bullet 7H_2O$ 100 g/L $NiSO_4 \bullet 7H_2O$ 5-25 g/L $CuSO_4 \bullet 5H_2O$ j = 0.5-2 A/cm^2 35°C	Cu-Ni incorporated with Cr nanoparticles (~40 nm)	10,11
Chrobak et al.	Mechanical and Young's Modulus	150 g/L $CuSO_4 \bullet 5H_2O$ 10 g/L H_2SO_4 Ni 0.1-20 mg/mL j = 1-100 mA/cm^2	Cu incorporated with Ni nanoparticles (~100 nm)	31
Fawzy et al.	Mechanical and Hardness	50 g/dm^3 $Na_3C_6H_5O_7 \bullet 2H_2O$ 25 g/dm^3 H_3BO_3 50 g/dm^3 $Na_2SO_4 \bullet 10H_2O$ 40 g/dm^3 $NiSO_4 \bullet 7H_2O$ 5-25 g/dm^3 $CuSO_4 \bullet 5H_2O$ j = 0.33-1.33 A/dm^2 0-20 g/dm^3 Al_2O_3 and TiO_2	Cu-Ni incorporated with Al_2O_3 and TiO_2	47
Hashemi et al.	Mechanical, hardness, and wear	90 g/L $H_3C_6H_5O_7$ 60 g/L NaOH 60 g/L $Na_2WO_4 \bullet 2H_2O$ 20 g/L $NiSO_4 \bullet 7H_2O$ 1 g/L $CuSO_4 \bullet 5H_2O$ 0-25 g/L SiC	Cu-Ni-W incorporated with SiC (~50 nm)	48

		j = 10-50 mA/cm^2 Stir Rate = 100-600 rpm		
Wan et al.	Mechanical and tensile strength	*Bath Conditions Not Given	Cu-Ni reinforced carbon fibers (6-8 μm)	49
Cui et al.	Electrochemical Study for Magnetic and Mechanical Properties	184 g/dm^3 $NiSO_4$•$6H_2O$ 6.24 g/dm^3 $CuSO_4$•$5H_2O$ 76.47 g/dm^3 $Na_3C_6H_5O_7$•$2H_2O$ 0.2 g/dm^3 Sodium Dodecyl Sulfate 0.5 g/dm^3 Saccharin Stir Rate = 200 rpm j = 10-20 mA/cm^2 30°C	Cu-Ni incorporated with Al nanoparticles (3 μm)	50
Thurber et al.	Mechanical, Hardness, Shear and Corrosion	0.24 M $Ni(NH_4)_2(SO_4)_2$·$6H_2O$ 0.06 M $CuSO_4$•$5H_2O$ 0.25 M $Na_3C_6H_5O_7$•$2H_2O$ MMT 0-0.2% E_{app} = -1.0V 25°C	Cu-Ni incorporated with MMT platelets	68

3.2 Pure Cu-Ni

3.2.1 Electrodeposition of Cu-Ni from a Citrate Bath

Citrate is utilized as a frequent ligand for transition metal ions, and has been successfully complexed for the deposition of Cu-Ni coatings [2, 4, 64-66]. Depending on the pH, an insoluble copper citrate complex can form and precipitate rather quickly [2]. The distribution of citrate in the electrolyte as a function of composition, temperature and pH was analyzed to try and stabilize the bath for extended lengths of time [2]. It was observed that at the native pH of 4.1, the solution was unstable and a precipitate would form within a few days [2]. The citrate solutions at pH 6.0 were found to be stable for several weeks with no precipitate formed [2]. In this work, the pH 6.0 Cu-Ni citrate complex will be evaluated for electrodeposition with montmorillonite because of the proven long term stability.

In this work, the citrate concentration is kept between the total concentrations of copper and nickel in the plating solution. Rode et. al [57] studied the complexion of Cu-Ni in a dual

plating solution. At pH values greater than 5, the heterobinuclear deprotonated species, $CuNiCit_2H_2^{4-}$ appears replacing the binary deprotonated species, $Cu_2Cit_2H_2^{4-}$. With Cu present in the plating solution, less citrate is available to complex with the nickel, resulting in a lower concentration of the species containing 1 nickel and 2 citrate ($NiCit_2H^{3-}$ and $NiCit_2^{4-}$) and an increase in $Nicit^{-}$species. In the copper-nickel solution, the heterobinuclear deprotonated species $NiCit_2^{4-}$ appears at pH values greater than 5. The maximum concentration of this nickel species is determined by the amount of copper present. The binary deprotonated species $Ni_2Cit_2H_2^{4-}$ begins to appear at a pH greater than 7.5 with and without Cu present. The presence of Cu in the electrolytic bath has a catalyzing effect on the nickel deposition [57]. Citrate ions begin to react with nickel ions to form nickel citrate complexes, which adsorb on to the surface of the cathode. This adsorption contributes to the deposition of nickel. The adsorption of citrate onto the cathode surface also helps to inhibit hydrogen evolution [57]. The formation of citrate complexes with bivalent metals is represented by the following general equilibrium equation:

$$pM^{2+} + qCit^{3-} + rH^{+} \leftrightarrow M_pCit_qH_r^{(2p-3q-r)+} \tag{3.3}$$

With a formation constant represented by:

$$\beta_{pqr} = \frac{[M_pCit_qH_r^{(2p-3q+r)+}]}{[M^{2+}]^p\,[cit^{3-}]^q[H^{+}]^r} \tag{3.4}$$

Copper and nickel undergo the following reactions in acidic conditions and in the presence of sodium citrate [56]:

The reactions for copper:

$$Cu^{2+} + Cit^{3-} \rightarrow CuCit^{-} \tag{3.5}$$

$$Cu^{2+} + HCit^{2-} \rightarrow CuHCit \tag{3.6}$$

$$CuCit^{-} + 2e^{-} \rightarrow Cu + Cit^{3-} \tag{3.7}$$

$$CuHCit + 2e^- \rightarrow Cu + CitH^{2-} \quad (3.8)$$

$$Cu^{2+} + 2e^- \rightarrow Cu \quad (3.9)$$

The reactions for nickel:

$$Ni^{2+} + Cit^{3-} \rightarrow NiCit^- \quad (3.10)$$

$$Ni^{2+} + HCit^{2-} \rightarrow NiHCit \quad (3.11)$$

$$NiCit^- + 2e^- \rightarrow Ni + Cit^{3-} \quad (3.12)$$

$$NiHCit + 2e^- \rightarrow Ni + HCit^{2-} \quad (3.13)$$

$$Ni^{2+} + 2e^- \rightarrow Ni \quad (3.14)$$

The reduction reactions of copper and nickel under acidic conditions are as follows:

$$Cu^{2+}_{(aq)} + 2e^- \rightarrow Cu_{(s)} \quad (3.15)$$

E°= +0.340 vs. SHE

$$Ni^{2+}_{(aq)} + 2e^- \rightarrow Ni_{(s)} \quad (3.16)$$

E°= -0.250V vs. SHE

3.2.2 Vegard's Law for Cu-Ni

X-ray diffraction (XRD) is a common crystallographic analysis technique which is applicable across a variety of applications. XRD provides crystalline structure information for the sample being analyzed. This technique is used extensively to examine texture properties of materials of interest, for this work focusing on the electrodeposited coatings on stainless steel substrates. Copper and nickel both have an face centered cubic (fcc) crystal structure and are both similar in atomic size, which should lead to a small amount of strain in the alloy system. The binary phase diagram for Cu-Ni shows complete solubility of copper into nickel in the liquid and

solid state, seen in Figure 3.2 [59]. Hence, continuous fcc equilibrium solid solution can be synthesized in the entire compositional range [59]. If the assumption is made that the ions of an alloy behave like hard spheres packed as close together as possible, then Vegard's law tells us that the alloy lattice constant should vary linearly with composition within the lattice parameters of pure copper and nickel: αalloy = x αCu + (1-x) αNi [60]. The particle size, strain, and lattice parameters were calculated for varying concentrations of the Cu-Ni alloy coatings.

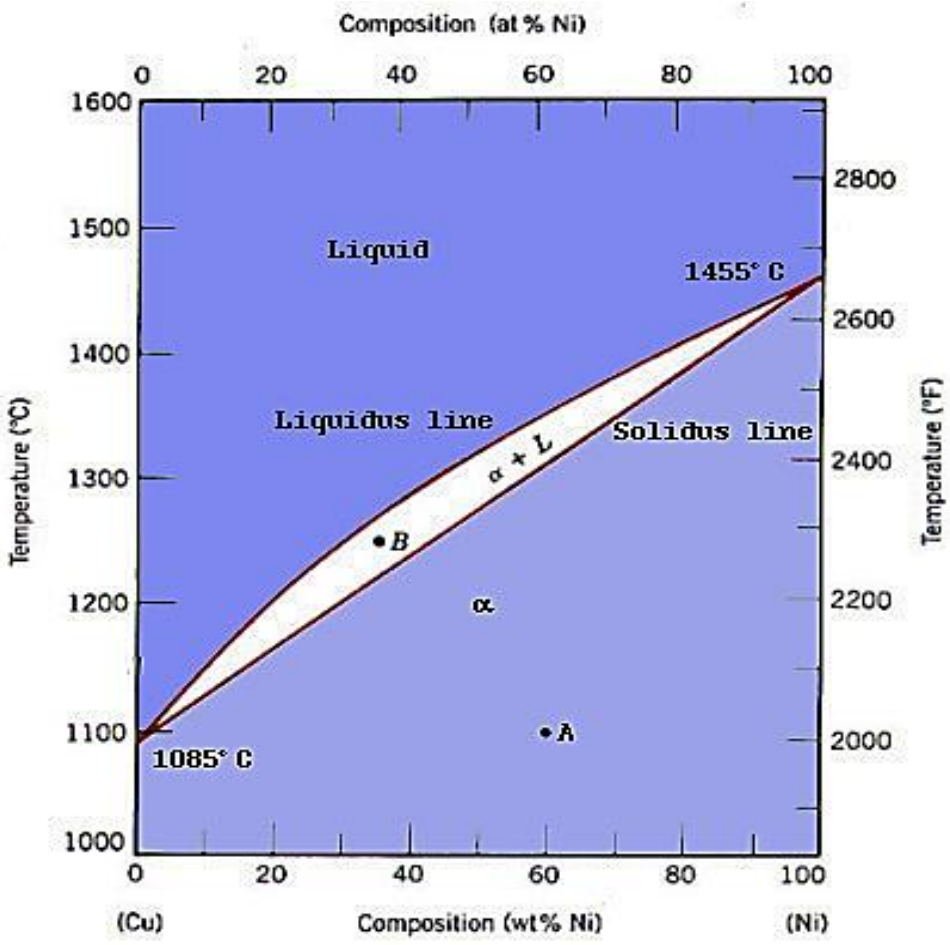

Figure 3.2: Phase diagram for Cu-Ni Alloys [61].

Nickel ammonium sulfate hexahydrate and copper sulfate pentahydrate were the metal salts used in the plating solution. The nickel was varied from 0.15M (Sample A), 0.20 M (Sample B),

0.25 M (Sample C), and 0.30M (Sample D), while the copper was held at 0.03M in the plating solution. Sodium citrate dihydrate (Fisher Scientific) was utilized as the ligand to stabilize the Cu-Ni complex and kept at a concentration of 0.25M for each plating bath. The baths were altered to a pH of 6 with 1.0M ammonium hydroxide. Silicon 325 mesh (Sigma-Aldrich) was used as the standard for XRD. An EG&G Princeton Applied Research Model 273A potentiostat/galvanostat was used for the electrodepositions. The electrochemical system is made up of a three electrode system. The working electrode was a stainless steel disc, the counter electrode was a coiled chromel wire, and the reference electrode was a saturated calomel reference electrode (SCE). The deposition parameters consisted of an $E_{applied}$ of -1.0V until a charge of 20C for the Cu-Ni films. X-ray diffraction (Siemens D-500 Diffractometer) was performed using the Cu Kα radiation λ = 0.15406nm at 35kV and 24mA. The scans were analyzed from 40-100° 2θ for the Cu-Ni films and 40-100° 2θ for the Cu-Ni-MMT films at a step size 0.05 degrees and dwell time of 1 second. Calculations were performed to calculate the particle size, stain, and lattice parameter. Both Williamson-Hall and the Scherrer equation were used to calculate the particle size.

The XRD spectrum for the Cu-Ni alloy film with the varying concentration of nickel and the stainless steel (SS) substrate can be seen in Figure 3.3. The silicon standard XRD spectrum can be seen in Figure 3.4, which was used to help calculate the strain and particle size. The fcc structure is confirmed in the XRD spectrum in Figure 3.3 because of the 2 peak to 1 peak to 2 peak configuration of the peaks. The spectrum also shows a preferred orientation for the (111) peak. Table 3.2 also shows the (111) peak and the (200) peak shifting between the standard value for copper and nickel, which indicates that a true alloy has been synthesized.

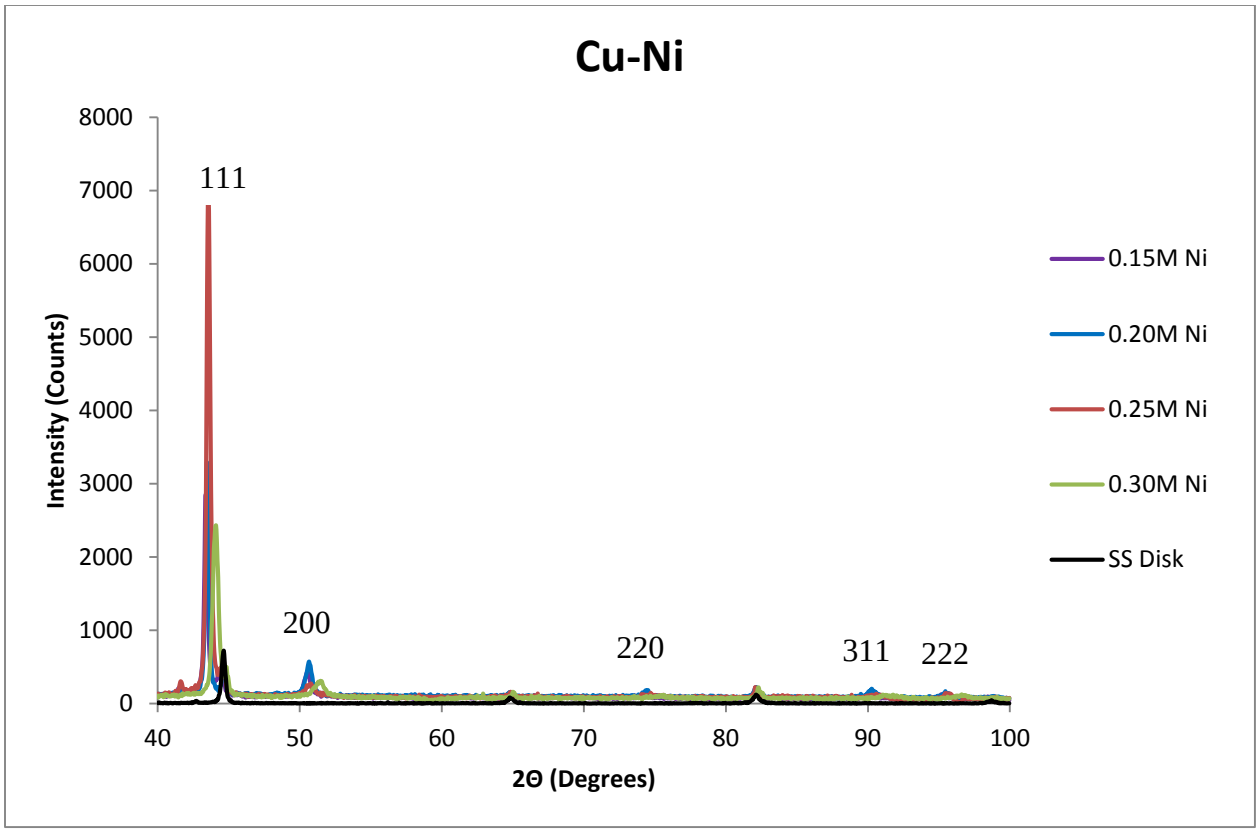

Figure 3.3: XRD spectrum of Cu-Ni with varying concentrations of Nickel 0.15M (Sample A), 0.20 M (Sample B), 0.25 M (Sample C), and 0.30M (Sample D), and of the stainless steel substrate.

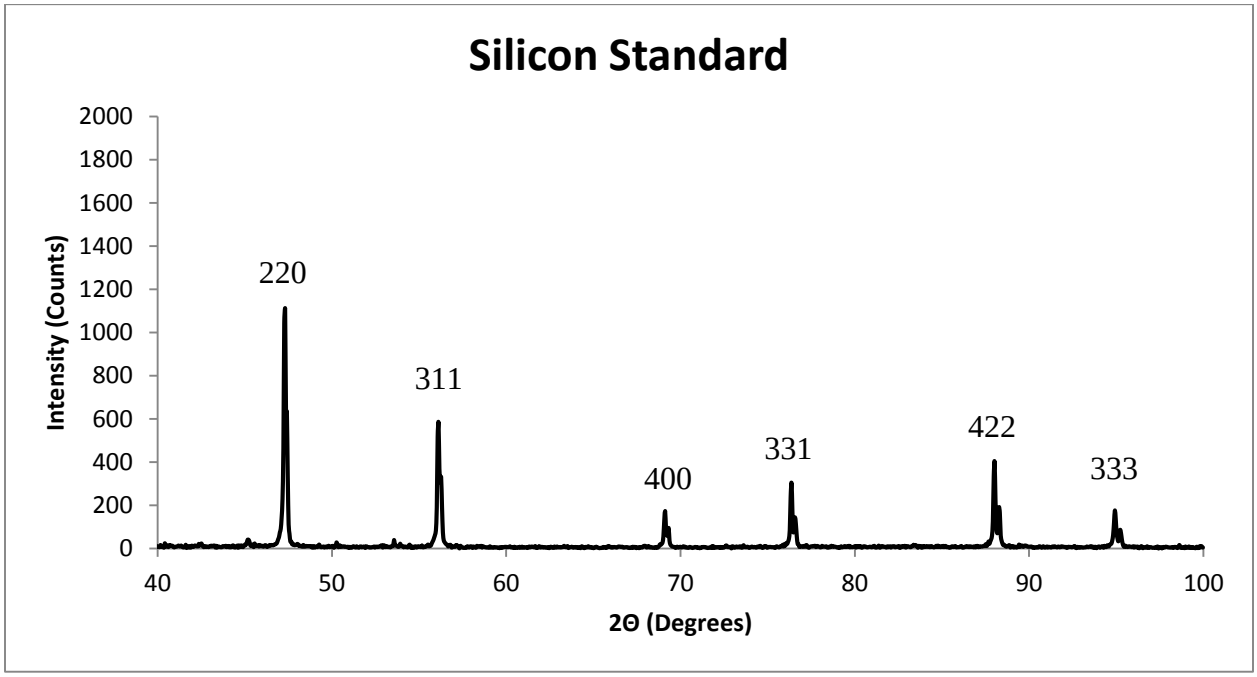

Figure 3.4: XRD spectrum of the standard Silicon 325 Mesh.

Table 3.2: Data from the XRD spectra showing peak shifting at the (111) and (200) peaks as the concentration of nickel is varied in the Cu-Ni alloy.

	Cu (111) (2Θ)	Ni (111) (2Θ)	Cu (200) (2Θ)	Ni (200) (2Θ)
Standard Value	43.297	44.508	50.434	51.847
Sample A	43.401		50.502	
Sample B	43.451		50.652	
Sample C	43.551		50.802	
Sample D	44.101		51.452	
SS Substrate	44.651		No Peak	

The lattice parameter (a) was calculated for the varying concentrations of the Cu-Ni alloy, seen in Table 3.3. Figure 3.5 is a graphical representation of the lattice parameter versus the varying concentration of nickel. The lattice parameter was calculated using the equation $a = \frac{\lambda}{2\sin\theta}\sqrt{h^2 + k^2 + l^2}$ [62]. The true value for the lattice parameter of copper is 0.3615 nm and for nickel is 0.3524 nm [60]. Table 3.3 and Figure 3.5 shows that the lattice parameter starts closer to copper with the lower concentration of nickel at 0.15M (0.3610 nm) and shifts towards nickel as the concentration increases to 0.30M (0.3561 nm). The result also confirms the formation of a true isomorphous alloy.

Table 3.3: Calculations for the lattice parameter (a) for samples A-D.

Sample A					λ=	0.154056
2Θ	Θ	SinΘ	h	k	l	a
43.401	21.700	0.36975	1	1	1	0.3608
50.502	25.251	0.42658	2	0	0	0.3611
74.257	37.128	0.60360	2	2	0	0.3609
90.210	45.105	0.70840	3	1	1	0.3606
95.161	47.580	0.73822	2	2	2	0.3614
					Average	0.3610
Sample B					λ=	0.154056
2Θ	Θ	SinΘ	h	k	l	a
43.451	21.725	0.37015	1	1	1	0.3604
50.652	25.326	0.42776	2	0	0	0.3601
74.507	37.253	0.60534	2	2	0	0.3600
90.260	45.130	0.70871	3	1	1	0.3605

95.461	47.730	0.73999	2	2	2	0.3606
					Average	0.3603
Sample C					λ=	0.154056
2Θ	Θ	SinΘ	h	k	l	a
43.551	21.775	0.37097	1	1	1	0.3596
50.802	25.401	0.42895	2	0	0	0.3591
74.707	37.353	0.60673	2	2	0	0.3591
90.610	45.305	0.71086	3	1	1	0.3594
95.611	47.806	0.74087	2	2	2	0.3602
					Average	0.3595
Sample D					λ=	0.154056
2Θ	Θ	SinΘ	h	k	l	a
44.101	22.050	0.37542	1	1	1	0.3554
51.452	25.726	0.43407	2	0	0	0.3549
75.657	37.829	0.61330	2	2	0	0.3552
91.260	45.630	0.71484	3	1	1	0.3574
96.611	48.306	0.74670	2	2	2	0.3573
					Average	0.3561

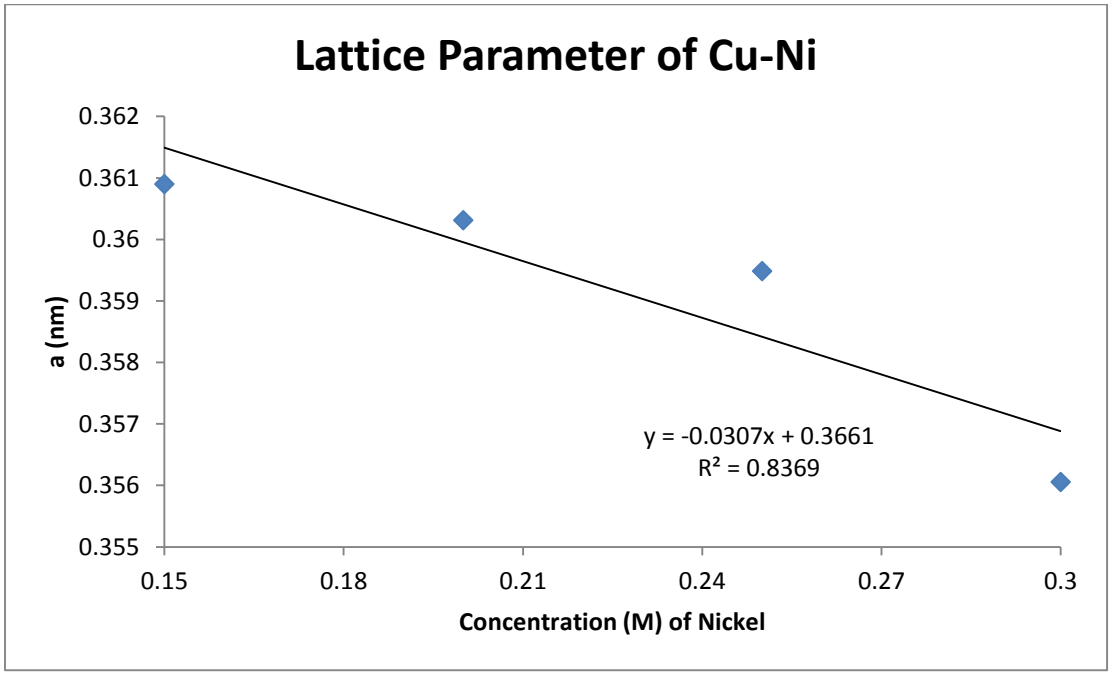

Figure 3.5: A graph of the lattice parameter versus the varying concentration of nickel.

The particle size and strain was calculated via the Williamson-Hall method, $B_r \cos\theta = k\lambda/L + \eta \sin\theta$, where k is the proportionality constant assumed to be 1, $\lambda = 0.15406$ nm from the Cu Kα radiation, η is the strain, L is the particle size, and B_r is the adjusted peak broadening. The Gaussian peak fit method of $B_r^2 = B_o^2 - B_i^2$ was used to calculate the peaks, where B_o is the peak broadening of the coating and the B_i is the instrumental broadening calculated using a 325 mesh silicon standard. [62]. Table 3.4 shows the calculations and Figure 3.6-3.9 show the graphical representation of the calculations. The full width at half max (FWHM) for B_i and B_o was calculated by taking the intensity and dividing it in half, subtracting out the baseline, and finding the width via excel. The strain (η) was the slope of the line calculated in Figures 3.6-3.9 and was found to be between 0.0024-0.0047, which shows little strain for the system. The particle size (L) was calculated by the y-intercept (kλ/L) which was found to be between 28.0-37.6 nm for the Cu-Ni alloy films.

Table 3.4: Calculations for the Williamson-Hall method to determine particle size (L) and strain (η).

Silicon Standard							
Peak #	2Θ (°)	hkl	FWHM (°)	FWHM (rad) = B_i			
1	47.307	220	0.20215	0.00353			
2	56.109	311	0.15954	0.00278			
3	76.363	331	0.16003	0.00279			
4	88.015	422	0.14479	0.00253			
5	94.917	333	0.16370	0.00286			
Sample A							
Peak #	2Θ (°)	Sin Θ	hkl	B_o (°)	B_o (rad)	$B_r^2=B_o^2 - B_i^2$	$B_r \cos\Theta$
1	43.401	0.36975	111	0.28988	0.00506	1.31E-05	0.00337
2	50.502	0.42658	200	0.65013	0.01135	1.21E-04	0.00995
3	74.257	0.60360	220	0.55011	0.00960	8.44E-05	0.00732
4	90.210	0.70840	311	0.60002	0.01047	1.03E-04	0.00717
5	95.161	0.73822	222	0.63014	0.01010	9.38E-05	0.00653

Sample B							
Peak #	2Θ (°)	Sin Θ	hkl	B_o (°)	B_o (rad)	$B_r^2=B_o^2 - B_i^2$	B_r cos Θ
1	43.451	0.37016	111	0.28008	0.00489	1.15E-05	0.00314
2	50.652	0.42777	200	0.59459	0.01038	1.00E-04	0.00903
3	74.507	0.60534	220	0.57042	0.00996	9.14E-05	0.00761
4	90.260	0.70871	311	0.59137	0.01032	1.00E-04	0.00705
5	95.461	0.73999	222	0.62209	0.01086	1.09E-04	0.00704
Sample C							
Peak #	2Θ (°)	Sin Θ	hkl	B_o (°)	B_o (rad)	$B_r^2=B_o^2 - B_i^2$	B_r cos Θ
1	43.551	0.37097	111	0.30098	0.00525	1.51E-05	0.00360
2	50.802	0.42895	200	0.61587	0.01075	1.08E-04	0.00938
3	74.707	0.60673	220	0.56138	0.00980	8.83E-05	0.00746
4	90.610	0.71086	311	0.61037	0.01065	1.07E-04	0.00727
5	95.611	0.74087	222	0.57961	0.01012	9.42E-05	0.00652
Sample D							
Peak #	2Θ (°)	Sin Θ	hkl	B_o (°)	B_o (rad)	$B_r^2=B_o^2 - B_i^2$	B_r cos Θ
1	44.101	0.37542	111	0.28843	0.00503	1.28E-05	0.00332
2	51.452	0.43407	200	0.62883	0.01098	1.13E-04	0.00956
3	75.657	0.61330	220	0.58013	0.01013	9.48E-05	0.00769
4	91.260	0.71484	311	0.60887	0.01063	1.07E-04	0.00721
5	96.611	0.74670	222	0.60231	0.01051	1.02E-04	0.00672

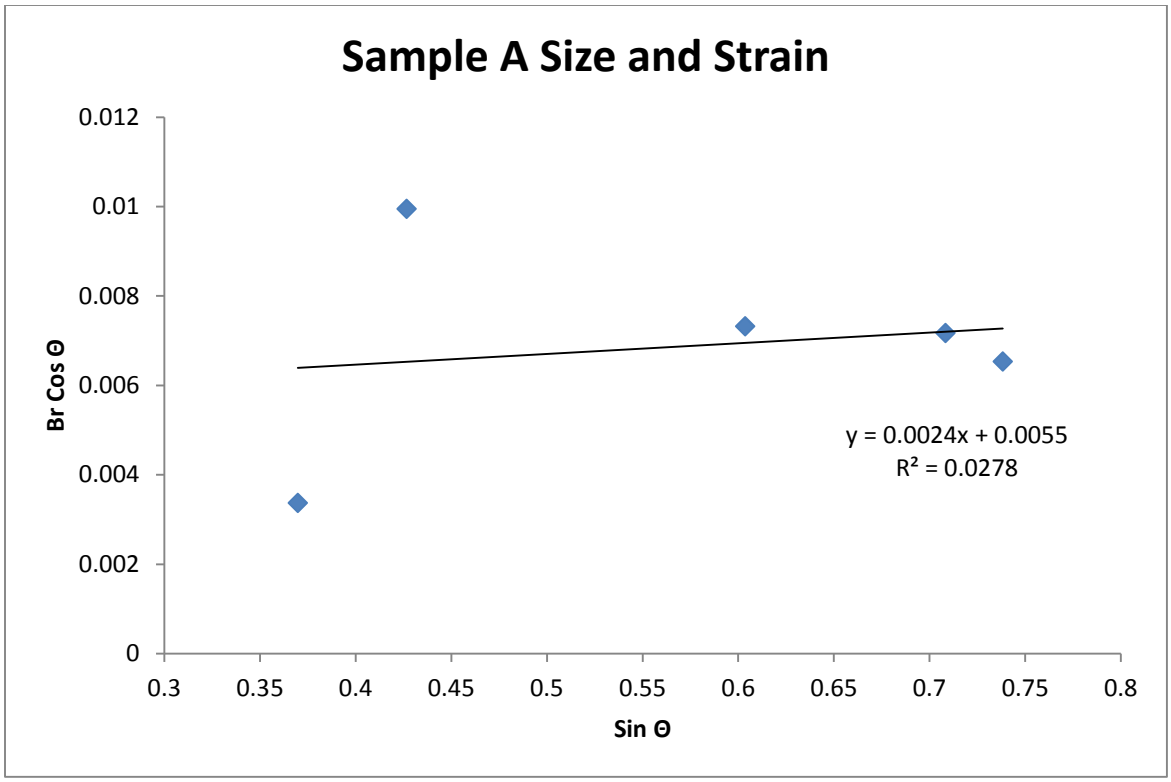

Figure 3.6: Williamson-Hall plot for Sample A.

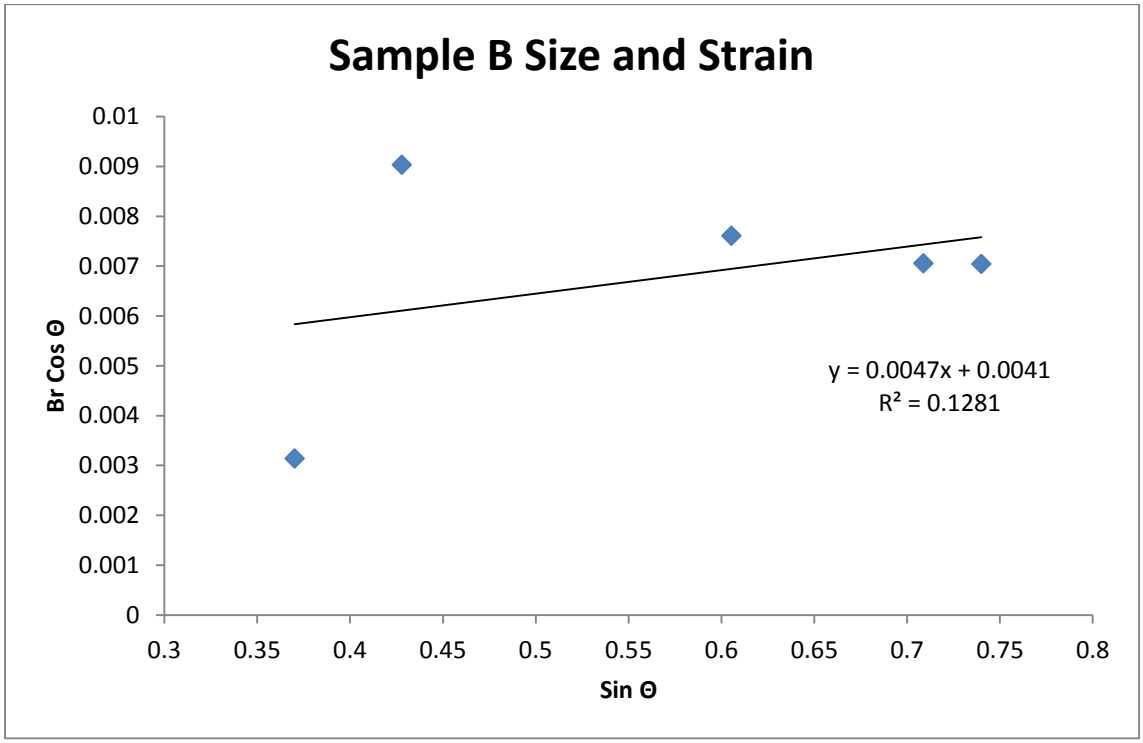

Figure 3.7: Williamson-Hall plot for Sample B.

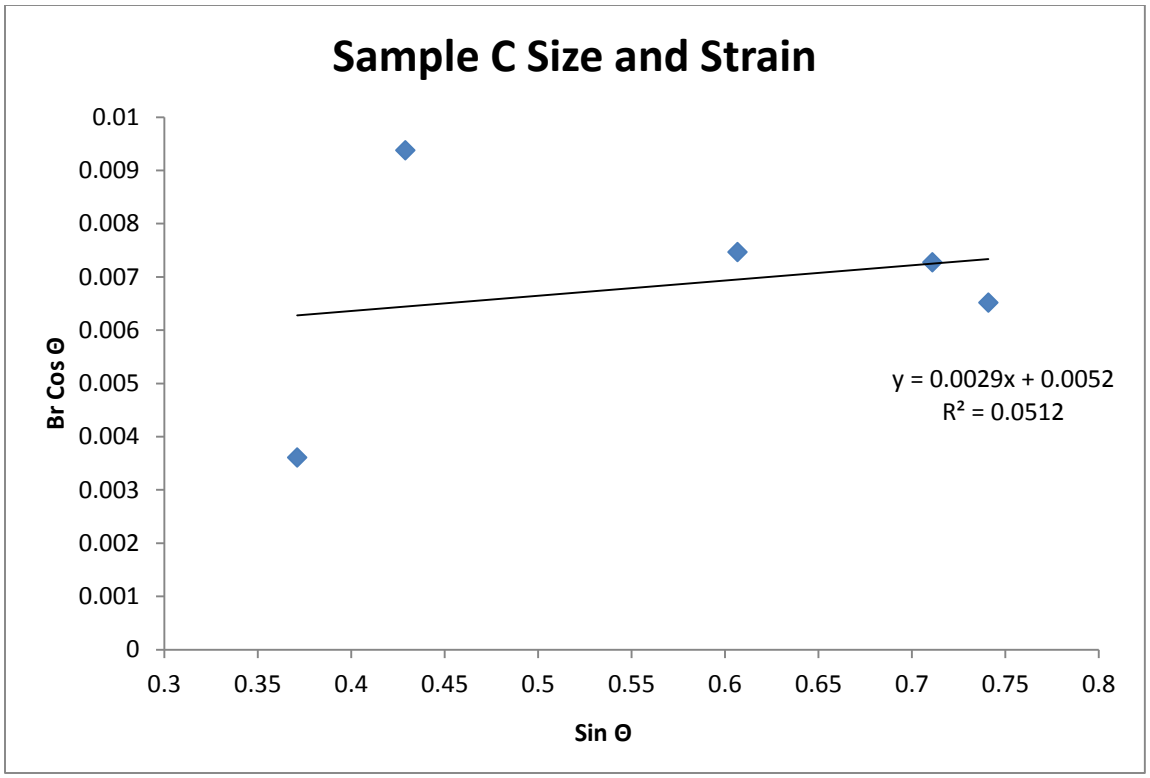

Figure 3.8: Williamson-Hall plot for Sample C.

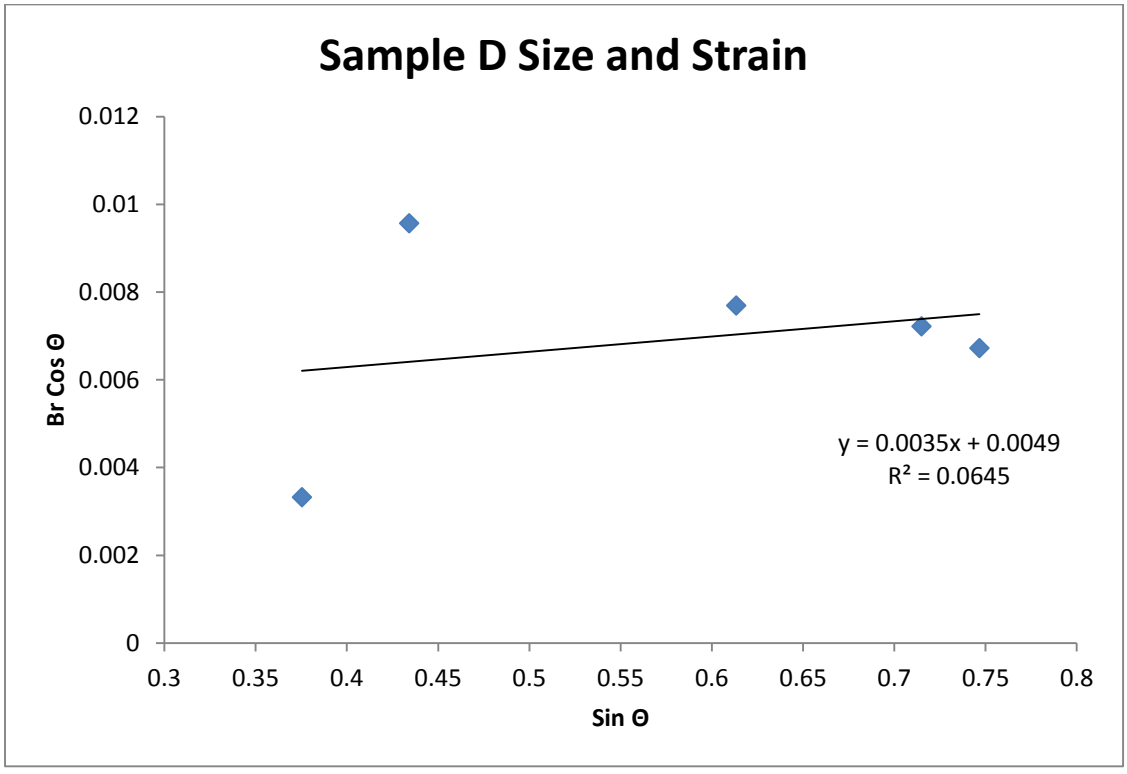

Figure 3.9: Williamson-Hall plot for Sample D.

The particle size was also calculated using the Scherrer equation, $B_r = k\lambda/L \cos\Theta$, seen in Table 3.5. This analysis was also preformed because the film showed a strong preferred (111) orientation leading to small peak intensities for the other peaks in the XRD spectrum, which caused a difficulty in calculating the FWHM values with certainty. Although, the values were in a similar range when compared to the Williamson-Hall method.

Table 3.5: Particle size calculated from the Scherrer equation for the Cu-Ni alloys.

Coating	Particle Size (nm)
Sample A	45.7
Sample B	49.0
Sample C	42.7
Sample D	46.4

3.2.3 Quality, Composition, and Adhesion of the Cu-Ni Alloys

The two copper alloys that are most commonly examined are Cu-Ni 90-10 (Alloy 70600) and Cu-Ni 70-30 (Alloy C71500) [63]. Cu-Ni 90-10 coatings give better protection in more stagnant conditions, whereas the Cu-Ni 70-30 coatings are used in higher flow conditions because of the increased hardness provided by the higher concentration of nickel [63]. Several different deposition and adhesion conditions were performed to obtain viable 70-30 and 90-10 Cu-Ni coatings, which can be seen in Table 3.6. After all of the experimentation, the final plating conditions used for this work are shown in Table 3.7.

Table 3.6: Different experimental conditions that were explored and the results.

Condition	Result
Low concentrations of copper and nickel 0.03M $Ni(NH_4)_2(SO_4)_2 \cdot 6H_2O$ 0.01M $CuSO_4 \cdot 5H_2O$ 0.025M $Na_3C_6H_5O_7 \cdot 2H_2O$ E_{app}= -1.1V	The film had poor adhesion and the surface was rough. Also, the coatings contained high amounts of Ni vs. Cu.
Higher concentrations of copper and nickel 0.3M $Ni(NH_4)_2(SO_4)_2 \cdot 6H_2O$ 0.03M $CuSO_4 \cdot 5H_2O$	The film had poor adhesion and the surface was rough.

0.25M $Na_3C_6H_5O_7 \cdot 2H_2O$ E_{app}= -1.1V	
Changed E_{app} = -1.0V (Previous Condition) 0.3M $Ni(NH_4)_2(SO_4)_2 \cdot 6H_2O$ 0.03M $CuSO_4 \cdot 5H_2O$ 0.25M $Na_3C_6H_5O_7 \cdot 2H_2O$ E_{app}= -1.0V	The surface was smooth and adhesion was stronger (still not usable). Also, the coatings contained higher amounts of Ni vs. Cu.
Varied the concentration of Ni from 0.15M to 0.4M and kept the concentration of Cu and Citrate the same, while monitoring composition with AAS. Also, the charge deposited on the substrate was varied from 15.00 C to 30.00 C.	The analysis revealed a composition range from 93% Cu to 7% Ni to 18% Cu to 82% Ni. Also, found that the amount of charge deposited on the substrate changed the composition. It seemed as though copper was limiting and was exhausted during longer depositions. The films also still had poor adhesion.
Concentration of Cu was raised to 0.06M	It was found that the increase in copper stabilized the coatings and there was no change in the composition from 15.00C to 30.00 C giving a consistent wide range for deposition thicknesses. Conditions were found through AAS for a 70-30 Cu-Ni film and a 90-10 Cu-Ni film.
Tried to increase the adhesion with a copper seed pretreatment	The copper pretreatment helped with adhesion of the coating to the substrate but still failed the scotch tape test.
Tried to increase adhesion with a Ni-MMT seed pretreatment at pH 2.5 condition with 0.5% MMT	The Ni-MMT pretreatment added superior adhesion of the film to the substrate. The coating passed the tape test and is difficult to remove even with mechanical polishing.
All previous conditions were ran in potentiostatic condition. Tried to run in galvanostat conditions.	The coatings had poor adhesion and showed bubbled surface roughness from H_2 evolution.
Added small amounts of MMT to the Cu-Ni plating bath solutions between 0.01% and 0.05%	Found that the only film showing incorporation of MMT into the Cu-Ni matrix was 0.05% using the results from EDS.
Added higher concentrations of MMT between 0.05% to 0.5%	Found that any concentration over 0.2% MMT, the solution was viscous and caused the deposition rates to drop below 1 mA/cm^2 and the coatings were poor.
All previous conditions were ran on the inverted cell design using nitrogen for agitation (Figure 3.10). Tried running the deposition with the substrate hanging sideways and using mechanical stirring.	The result showed little to no incorporation of MMT with the use of EDS.

Table 3.7: The final electrodeposition parameters determined for 70-30 and 90-10 Cu-Ni-MMT.

Solution Composition	
$Ni(NH_4)_2(SO_4)_2 \cdot 6H_2O$	0.32M (70-30 Cu-Ni)
$Ni(NH_4)_2(SO_4)_2 \cdot 6H_2O$	0.24M (90-10 Cu-Ni)
$CuSO_4 \cdot 5H_2O$	0.06M
$Na_3C_6H_5O_7 \cdot 2H_2O$	0.25M
MMT	0.05 - 0.2%
pH	6.0
Working Electrode	430 Stainless Steel disc
Counter Electrode	Pt Mesh
E_{app}	-1.0V

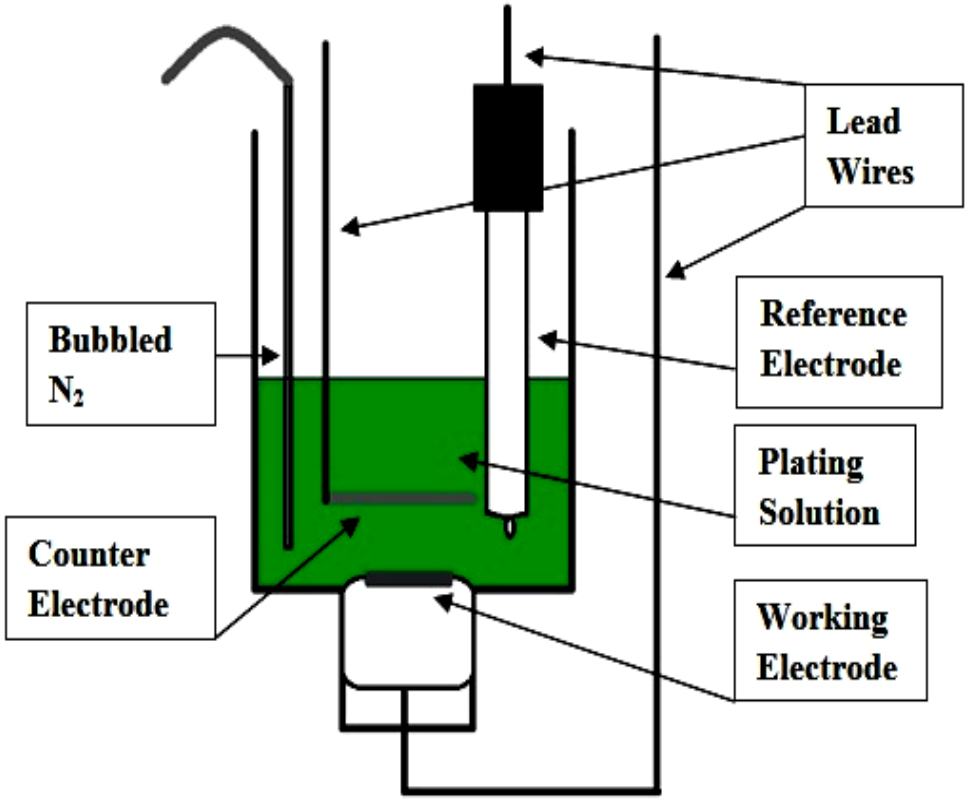

Figure 3.10: Inverted cell design for incorporation of particles into a metal matrix.

Through previous studies, it was noted the electrochemical cell design has a large effect on the overall coating quality through morphology, adhesion and covering of the metal substrate. Figure 3.10 shows the working electrode in an inverted manner to the plating solution. With this design, a slurry of electrolytic solution and clay develops on top to the working electrode, allowing for easier intercalation of the MMT platelets into the depositing metallic matrix. Other cell designs were experimented with but were not found to produce the optimal MMC coating.

3.3 Cu-Ni MMCs

3.3.1 Cu-Ni MMCs in MEMS and Electronics

Cu-Ni composites have shown to be beneficial in the area of MEMS devices, microactuators, and electronics. Al_2O_3, Ni nanoparticles, and Cr particles have been incorporated into the metal matrix to produce improved mechanical properties, magnetic properties, and chromia scale for oxidation resistance [7-11].

Panda et al. [7] evaluated the electrodeposition of graded Ni-Cu alloys and Ni-Cu-γ-Al_2O_3 composites into deeply depressed electrodes made using X-ray lithography for use in MEMS devices. The rotating cylinder experiment showed that the current efficiency was below 100% for the deposition over a diverse range of current densities. With the inclusion of 12.5 g/L of alumina at a rotation rate of 1000 rpm, it was found that the current efficiency was drastically lowered by the incorporation of the nanoparticles below 20 mA/cm^2, but produced deposits with higher copper content which was preferred. At the greater current densities (30-50 mA/cm^2), the current efficiency was less effected but lead to coatings with higher nickel content. The Cu weight ratio was studied at different heights on the micropost for pure Cu-Ni and Cu-Ni-Al_2O_3 at current densities of 10 and 15 mA/cm^2, seen in Figure 3.11 and 3.12, respectively. A rise in the

concentration of Cu along the post was expected due to the reduction of boundary layer thickness because of the diffusion controlled reaction mechanism of copper. The composite micropost showed a sharp increase in the Cu concentration starting at about a height of 300 μm with the incorporation of alumina, which suggests that the incorporated nanoparticles into the plating bath helped to improve the mass transport at the site of the recess [7].

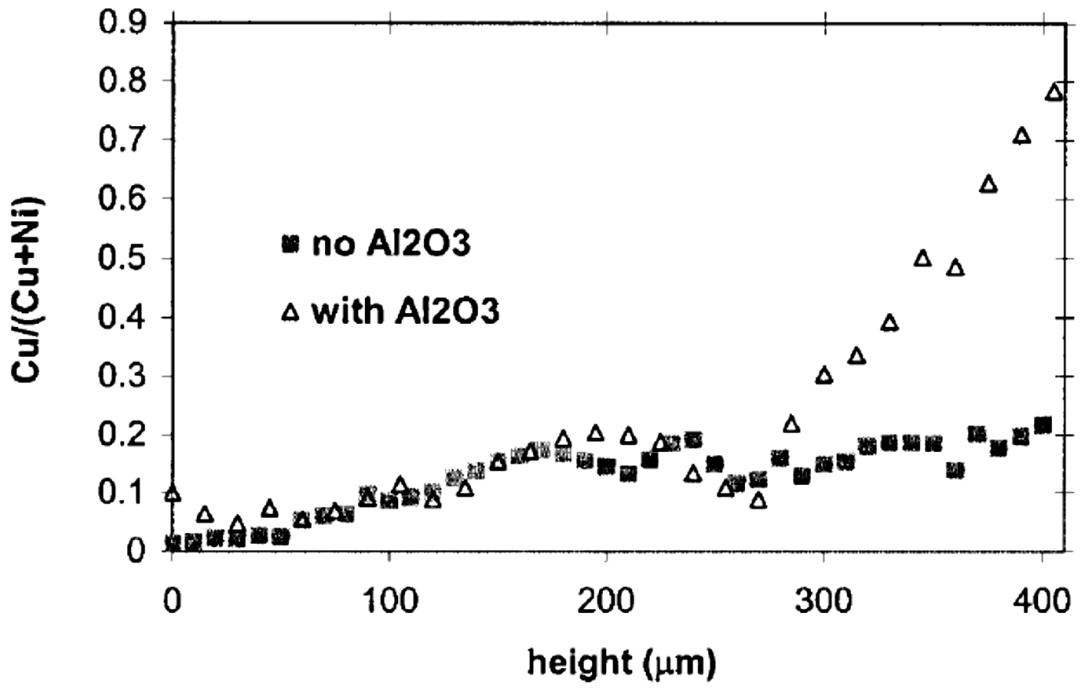

Figure 3.11: The copper weight ratio versus the height of the micropost with and without alumina for current density of 10 mA/cm^2 and a duty cycle of 0.125. "Reproduced by permission of The Electrochemical Society." [7].

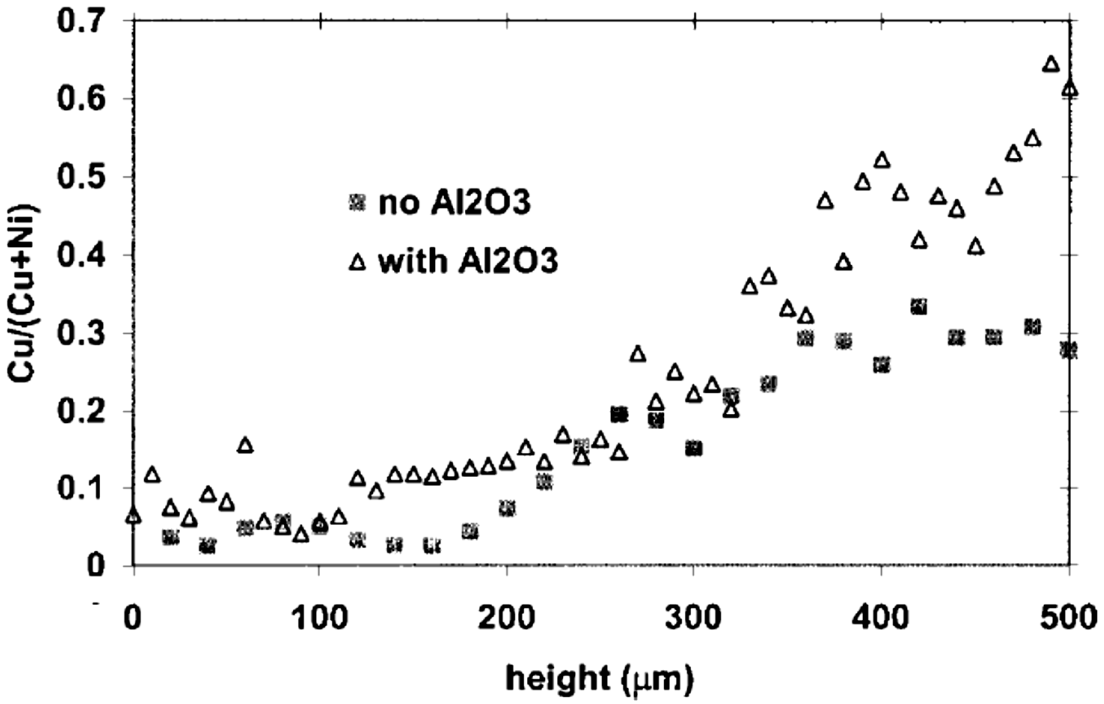

Figure 3.12: The copper weight ratio versus the height of the micropost with and without alumina for current density of 15 mA/cm^2 and a duty cycle of 0.125. "Reproduced by permission of The Electrochemical Society." [7].

Huang et al. [9] experimented with a Cu-Ni composite from a plating bath consisting of an alkaline copper solution incorporated with 2-5 g/L of ~50 nm nickel nanoparticles to increase the performance in magnetic microactuators for MEMS. The superconducting quantum interference device (SQUID) measurements for magnetism seen in Figure 3.13 demonstrates that with the inclusion of ferromagnetic Ni particles into the copper matrix the film shifts from diamagnetic to ferromagnetic in nature as the curve become larger. The vertical displacement of the magnetic microactuator was measured for the actuator coils fabricated from copper and Cu-Ni composite materials. Figure 3.14 indicates that under the same experimental conditions, the Cu-Ni composite coil possessed a greater vertical displacement versus the pure Cu film, leading to about a 9% increase in the actuation enlargement performance [9].

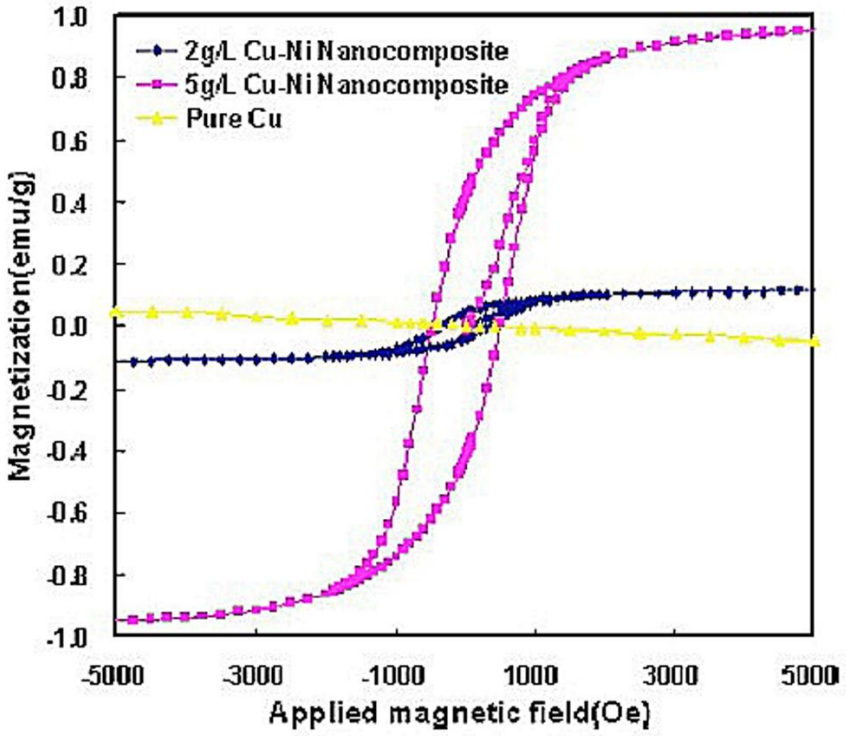

Figure 3.13. The SQUID measurements of copper versus the Cu-Ni composite electrodeposited from a bath that contained 2-5 g/L of nickel nanopowder [9].

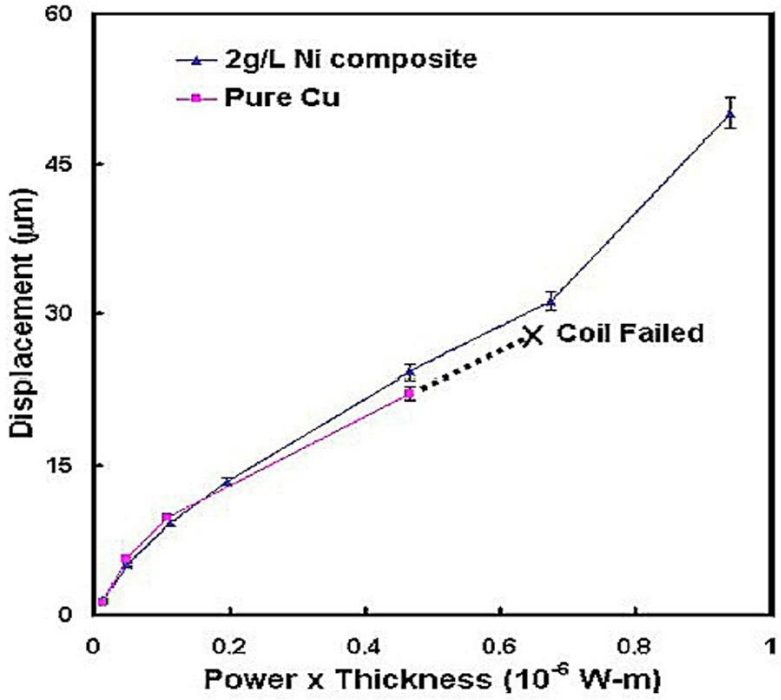

Figure 3.14. The vertical displacement results of the diaphragms compared to the normalized input experienced by the driving coils, which consists of the copper and Cu-Ni composite [9].

Chen et al. [8] proposed a new coil material for a reduced power electromagnetic microactuation device using Cu-Ni nanocomposites from an alkaline Cu-plating bath integrated with 2-8.5 g/L 100 nm nickel nanoparticles. Different coil widths ranging from 10-500 μm were examined with SQUID and resistivity measurements to determine the optimal power saving microspeaker device. The SQUID and resistivity analysis found that the 200 μm wide inductive coil from the bath containing 2 g/L of Ni nanoparticles had optimal ferromagnetic characteristics with low resistivity. The sound pressure level was then evaluated for the pure copper and optimal Cu-Ni nanocomposite wire for a frequency ranging from 1-6 kHz, which resulted in a 40% power savings for the Cu-Ni nanocomposite versus the pure copper coil [8].

A crucial problem for extending the applications of Cu-Cr MMCs is poor resistance to oxidation, specifically in high temperature environments for the electrical and electronic industries [10, 11]. This is due to the fact that at high temperatures chromium has a low solubility into copper, which greatly decreases the chromium amount diffusing to the surface of the copper matrix, preventing growth of the protective Cr_2O_3 scale. Nickel can be added into the matrix to increase the solubility of Cr into the composite to help increase the resistance to oxidation [11]. Huang et al. [10] discussed the electrodeposition of Cu-Ni-Cr, where copper and nickel were at a 1:1 ratio. They found that incorporating 15-20 wt.% Cr nanoparticles (~40 nm) into the Cu-Ni matrix allowed for a good chromia scale to form during the oxidation process in atmosphere at 800°C. It was found that incorporating less than 15 wt.% Cr lead to non-uniform growths of the chromia scale. Huang et al. [11] also examined the electrodeposition of Cu-30Ni-20Cr and Cu-50Ni-20Cr for the formation of the Cr_2O_3 protective scale. Figure 3.15 displays an X-ray diffraction pattern for the two electrodeposited coatings plus two commercially available alloys of the same composition after oxidation in atmosphere at 800°C. The result shows that the

commercial alloys mainly consist of more NiO, Cu_2O, and CuO after oxidation, whereas the electrochemically prepared coatings consists primarily of Cr_2O_3 and $NiCr_2O_4$. Figure 3.16 shows SEM pictures of the Cr_2O_3 scale created from the oxidation process at 800°C. It was discovered that for the electrodeposited samples the Cr_2O_3 scale quickly formed in the initial stage of growth and continued through the steady-state stage, where the coating acts as a reservoir for Cr to maintain the chromia scale growth. The commercially available sample Cu-50Ni-20Cr showed a similar result to the electrodeposited coatings but the Cu-30Ni-20Cr showed virtually no growth of the Cr_2O_3 scale, which showed that the commercial grade relied on an increase in Ni content to grow the Chromia scale [11].

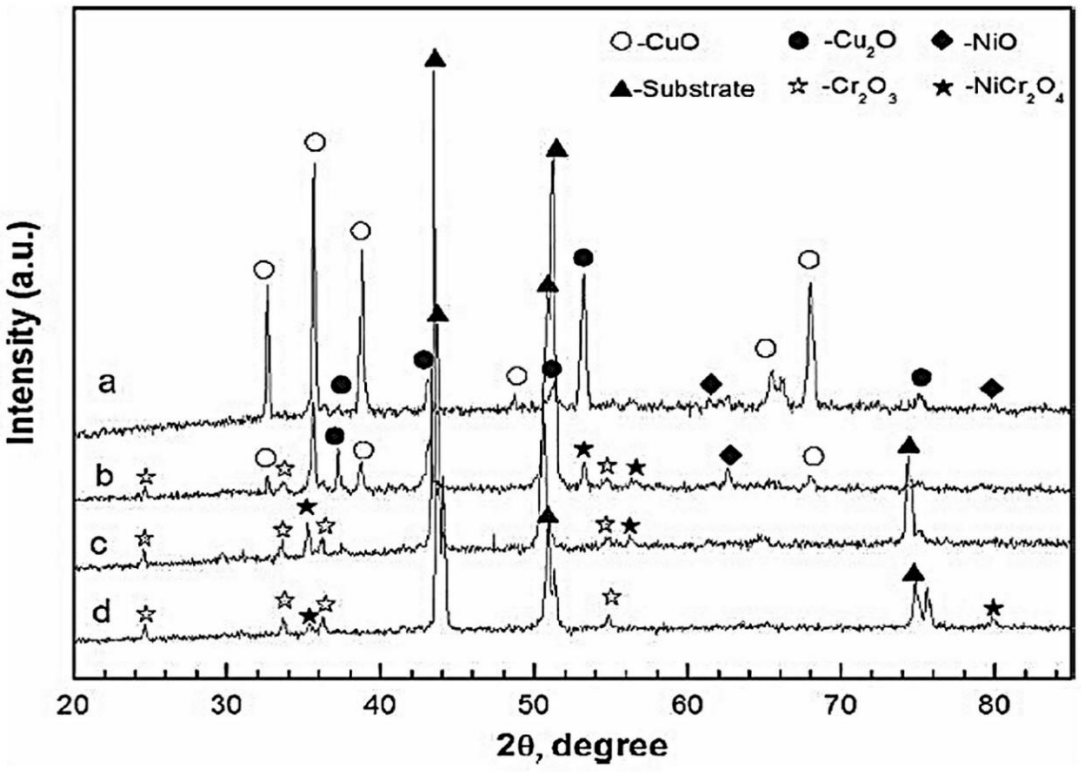

Figure 3.15: The stacked x-ray diffraction patterns of the Cr_2O_3 scale generated on four different samples after oxidation in atmosphere at 800 °C for 20 hours: [a] commercial grade Cu-30Ni-20Cr, [b] commercial grade Cu–50Ni–20Cr, [c] electrodeposited Cu–30Ni–20Cr composite, and [d] electrodeposited Cu–50Ni–20Cr composite [11]. "Reprinted with the permission of Cambridge University Press."

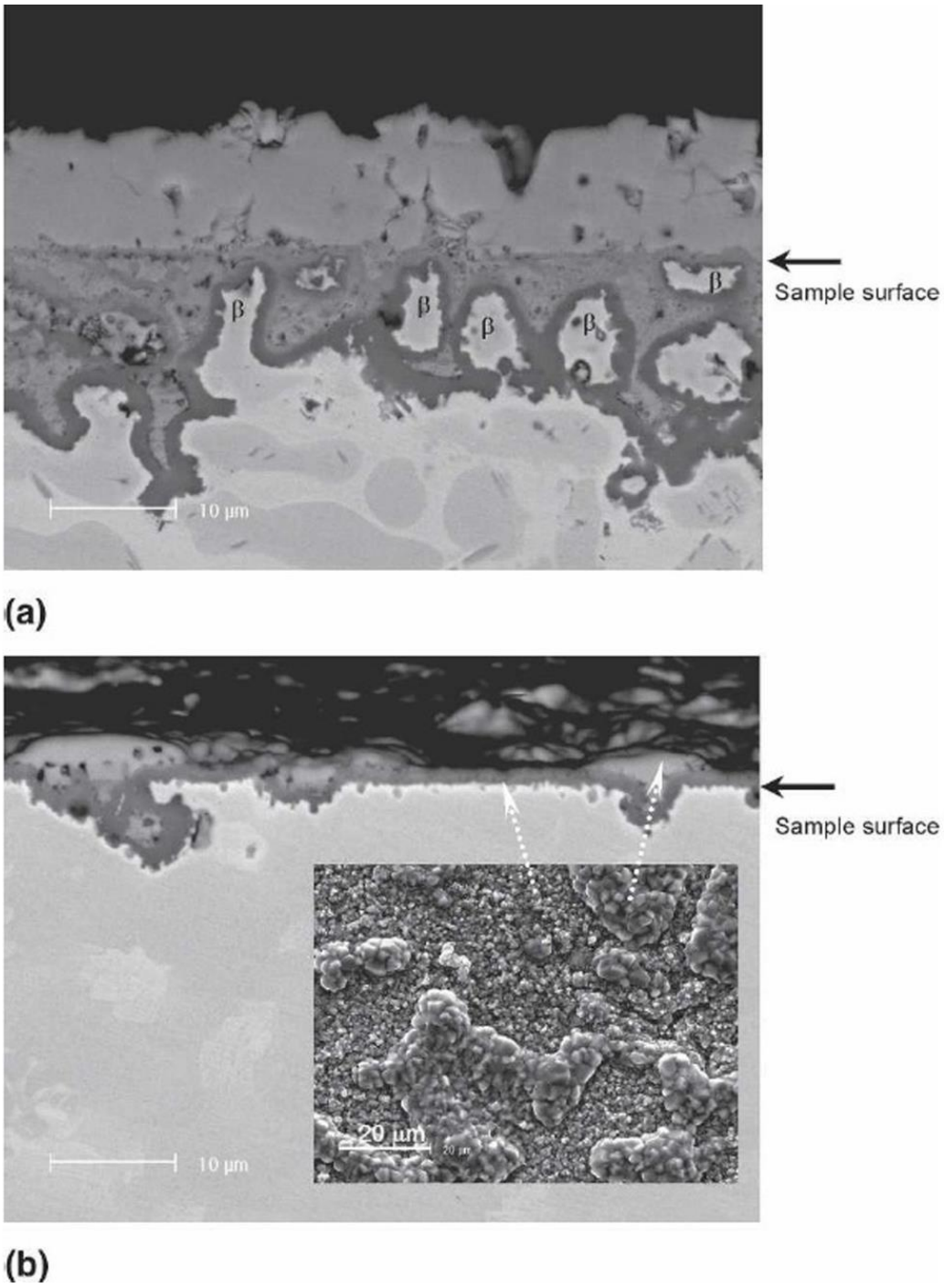

Figure 3.16: The Cross-sectional SEM of the Cr_2O_3 scales formed on the surface of the Cu-Ni-Cr alloys of [a] Cu–30Ni–20Cr and [b] Cu–50Ni–20Cr, which was oxidized for 20 hours in atmosphere at 800 °C and the inset displays the structure of the different oxides at the surface, which are designated by arrows [11]. "Reprinted with the permission of Cambridge University Press."

3.3.2 Cu-Ni MMCs for Enhanced Mechanical Properties

Particle incorporation can be used to improve mechanical properties for MMC coatings over that of the pure metal matrix. The Cu-Ni matrix has been incorporated with Ni particles, TiO_2, Al_2O_3, SiC, carbon fibers, and montmorillonite to increase the hardness, wear resistance, shear adhesion, and tensile strength [31, 47-49, 68].

Chrobak et al. [31] examined electrodeposited copper incorporated with Ni powder (~100 nm) at varying current densities to examine the effects to Young's modulus. They experimented with current densities ranging from 1-100 $mAcm^{-2}$ and found that the concentration of Ni in the coating increases linearly with current density but the thickness of the coating decreases because the transport of Cu to the electrode surface is suppressed by the Ni particles. They also discovered that adding 25 vol.% of glycerol to the bath helped reduce agglomeration and decrease the grain size of the MMC coatings. The Young's modulus was found to decrease when the Ni concentration was increasing. This trend was even more drastic as the current density was increased because an increased current density leads to higher concentrations of Ni [31].

The Fawzy group [47] examined how the current density, concentration of ceramic particles in the electroplating solution, and pH of the plating bath affected the hardness for Cu-Ni, Cu-Ni-αAl_2O_3, and Cu-Ni-TiO_2 composite coatings. By increasing the current density from 0.33 to 1.33 Adm^{-2} for the Cu-Ni-αAl_2O_3 and Cu-Ni-TiO_2 depositions, an increase in the Ni percentage in the coating and hardness was observed versus the pure Cu-Ni coating, but the percentage of the ceramic particles in the coating decreased. Increasing the pH of the plating solutions from 2.5 to 4.05 lead to an escalation in the Ni percentage in the film, loading percentage of the ceramic particles, and hardness. The hardness increased as the Al_2O_3 and TiO_2 increased in the plating solution from 170 to 248 kgf mm^{-2} for the addition of αAl_2O_3 particles with no effect to the Ni

concentration in the coating, whereas the addition of TiO_2 particles produced an increase from 170 to 231 kgf mm^{-2} and helped to increase the Ni percentage in the coating. The optimal coating parameters were determined to be 1.33 A dm^{-2} for the current density, at pH 4.05, and incorporating 20 g dm^{-3} of the ceramic particles into the plating bath [47].

Hashemi et al. [48] studied the electrodeposition of Cu-Ni-W incorporated with SiC nanoparticles. They investigated the effects of different concentrations of SiC ranging from 0 to 25 g/L, stir rates ranging from 100 to 600 rpm, and the change in current density from 10 to 50 $mAcm^{-2}$. They optimized the plating conditions to obtain the best wear protection and hardness for the coatings. With the change in concentration from 0 to 25 g/L SiC in the plating solution, 15 g/L was found to have the highest incorporation of SiC into the coating. Also, the 15 g/L incorporation of SiC into the Cu-Ni matrix increased hardness and had the lowest weight loss factor and friction factor from the wear results. It was hypothesized that any amount over 15 g/L caused agglomeration of the SiC particles, which produced observable voids on the surface of the coating in the SEM pictures. A 400 rpm stir rate and the 20 $mAcm^{-2}$ current density proved to be the optimal conditions for the best wear resistance and hardness. The SEM of the coating incorporated with 15 g/L of SiC, stirred at 400 rpm, and electrodeposited with a current density of 20 mA cm^{-2} showed the least amount of visible wear on the surface after testing [48].

Wan et al. [49] developed a continuous three step deposition process to produce Cu, Cu-Fe, and Cu-Ni reinforced carbon fiber (6-8 μm in diameter) composites. Cu-C, Cu-Fe-C, and Cu-Ni-C composites display similar strength vs. temperature graphs to each other, but the decreasing trend seen in the tensile strength is controlled by a different mechanism. A decrease in the tensile strength for the Cu-C composite was due to interfacial bonding at the carbon fiber interface. Interfacial debonding was found to be absent for Cu-Ni-C and Cu-Fe-C composites because it's

larger interfacial bonding strength is due to a diffusion reaction and a chemical reaction at the interface of the fiber-metal matrix. The maximum tensile strength value was obtained with the addition of Cu-Ni onto the carbon fiber interface, but the optimal tensile strength value was not found to be proportional to the interfacial bonding strength, whereas the highest bonding strength was found for the Cu-Fe-C composite [49].

Our group studied electrodeposited 70-30 and 90-10 Cu-Ni coatings incorporated with a platelet-clay known as montmorillonite (MMT) from a citrate bath. Layered silicates have several advantageous properties to be utilized for composites, such as a high surface area, chemical inertness, resistance to extreme temperatures, and resistance to pH changes. The inclusion of layered silicates, such as MMT, has shown an increase in hardness, adhesion, and corrosion resistance in Ni and Ni-Mo coatings [64-67]. MMT has a 2:1 layered structure, with two layers of the silicon tetrahedral sandwiching one layer of an aluminum octahedral. Seen in Figure 3.17, MMT is a hydrous aluminum silicate with the formula $(Na,Ca)(Al, Mg)_6(Si_4O_{10})_3\text{-}(OH)_6 \bullet nH2O$ and measures 1 nm in height and 1-2 microns in width [17]. The Al^{3+} and Si^{4+} locations can be replaced by lower valent cations, causing the montmorillonite structure to have an excess of electrons. The negative charge is compensated through loosely held cations from the associated water. Within aqueous solutions, MMT can be completely delaminated and incorporated into other materials, forming continuous, crack free films, which is a necessary requirement of corrosion resistant coatings [17]. For this work, a solution of MMT was stirred vigorously for 24-48 hours to exfoliate the layered silicates. When dealing with the electrocodeposition of a MMC, understanding the particle stability in the colloidal plating solution is vital because the properties of composites increase significantly with the preferential inclusion of individual particles [18]. The exfoliated MMT platelets are stable in solution and easily dispersed into aqueous solutions,

while the non-exfoliated MMT precipitates [60]. Once exfoliated and freely dispersed throughout the electrolytic bath, the MMT platelets can slowly settle down onto the surface of the electrode and be incorporated into the forming alloy coating structure as shown in Figure 3.17.

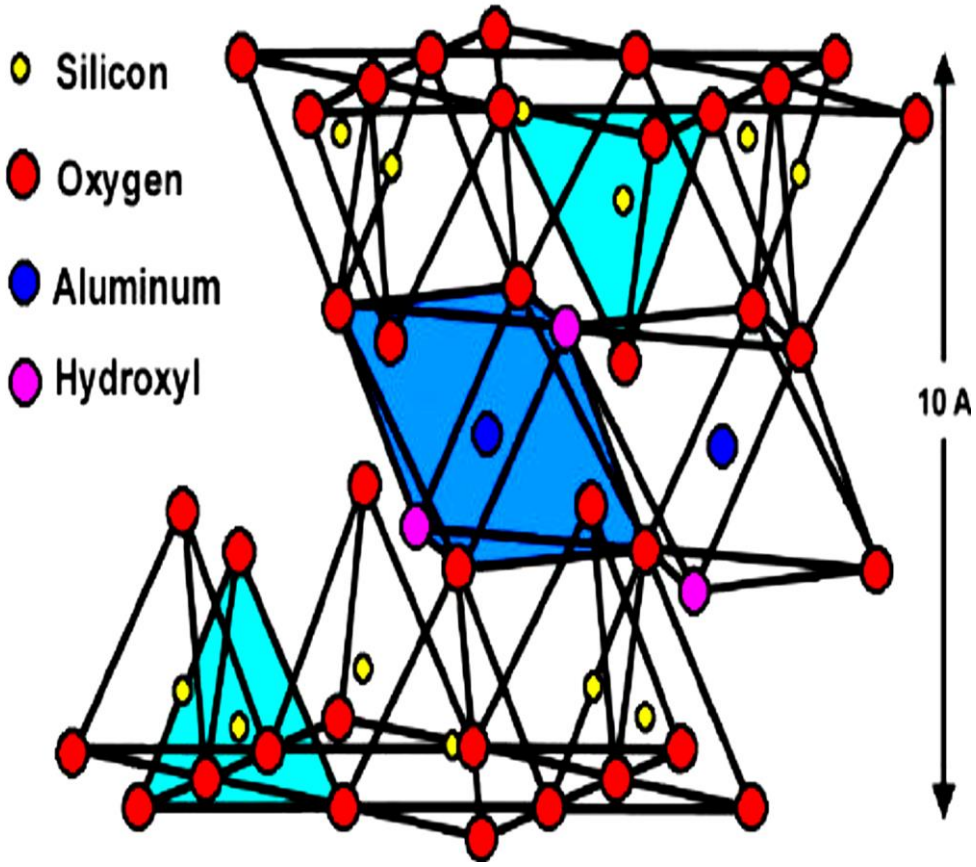

Figure 3.17: The structure and thickness of montmorillonite [17].

Copper-nickel alloys of the ratios 70-30 and 90-10 were electrochemically deposited from a citrate bath and compared to a composite coating incorporated with 0.05-0.2% MMT to study the effects of the mechanical properties. The adhesion shear strength and the microhardness hardness for the MMC coatings were investigated. With the addition of MMT, the adhesion shear strength showed an improvement of the 85-300% and the microhardness increased by 17-25% [68]. Details of the experiments and the results are further discussed in chapters 4 and 5.

3.3.3 Cu-Ni MMCs in Electrochemistry and Improved Corrosion Protection

Understanding the relationship between the electrochemical deposition parameters and resulting corrosion properties is of great importance for creating optimal coatings that will endure harsh environments. MMC coatings that reduce the rate of corrosion at a lower cost have been extensively studied. Exposing films to an unfavorable environment accelerates the degradation of the coating which can lead to many different types of occurring corrosion phenomena [69, 70]. The rate of corrosion can be slowed using five universal approaches which include the choice of materials, chemical inhibitors, altercations in the environment, cathodic protection, or coatings [71]. Al particles and MMT were incorporated into the Cu-Ni matrix to understand how magnetic particles affect the metal matrix and MMT to observe how platelets affect the corrosion resistance of the Cu-Ni coating [50, 68].

Cui et al. [50] successfully codeposited Cu-Ni-Al MMCs and noted that high amounts of Al (~3 μm) particles, 29 vol. %, could be deposited into the Cu-Ni coating matrix. They investigated whether the conductive Al particles would behave similar to inert particle codeposition according to the Guglielmi's model. Adding the conductive aluminum particles into the Cu-Ni matrix caused the polarization curve to shift to more negative potentials, which was credited to the non-active surface of the aluminum metal particles during the deposition of Cu-Ni following a similar codeposition path for inert particles defined by Guglielmi. The parameters used in Guglielmi's model for the codeposition of non-conductive inert particles can also model the deposition of charged particles presented in this research [50].

In addition to the mechanical properties, our group studied the corrosion behaviors of the 70-30 and 90-10 Cu-Ni-MMT coatings by the use of Tafel polarization and electrochemical impedance spectroscopy (EIS). The polarization resistance showed a 65-183% increase with the

addition of MMT, which was consistent with the EIS results. This confirms that embedding of layered silicate particles into the Cu-Ni metallic matrix increases its corrosion resistance [68]. The details of the corrosion experiments are discussed in chapters 4 and 5.

3.4 Conclusions

Electrodeposition provides a versatile and convenient route for controlled coating of composites (i.e., materials having more than one phase) containing nano- to micro- particles dispersed in a metal matrix for material science and engineering applications. Enhancement of the electrical, mechanical, and corrosion properties of the coatings is observed with the inclusion of different particles into the Cu-Ni matrix. With the increase in availability of micro and nanoparticles, more research needs to be performed in the area of Cu-Ni MMCs to further explore their beneficial properties. Chapter 4 and 5 further discusses the results and conclusions from the mechanical and corrosion experiments for the 70-30 and 90-10 MMC coatings incorporated with MMT.

3.5 References

[1] S. Mohan and N. Rajasekaren, Influence of electrolyte pH on composition, corrosion properties and surface morphology of electrodeposited Cu-Ni alloy, Surf. Eng. 7 (2011) 519-523.

[2] T.A. Green, A.E. Russell and S.J. Roy, The development of a stable citrate electrolyte for the electrodeposition of copper-nickel alloys, J. Electrochem. Soc. 145 (1998) 875-881.

[3] A. Varea, E. Pellicer, S. Pané, B.J. Nelson, S. Suriñach, M.D. Baró and J. Sort, Mechanical properties and corrosion behavior of nanostructured Cu-rich CuNi electrodeposited films, Int. J. Electrochem. Sci. 7 (2012) 1288-1302.

[4] S. Rode, C. Henninot, C. Vallières and M. Matlosz, Complexation chemistry in copper plating from citrate baths, J. Electrochem. Soc. 151 (2004) C405-C411.

[5] R. Orniakova, A. Turonova, D. Kladekova, M. Galova, and R.M. Smith, Recent developments in the electrodeposition of nickel and some nickel-based alloys, J. Appl. Electrochem. 36 (2006) 957–972.

[6] M. Alper, H. Kockar, M. Safak, M. C. Baykul, Comparison of Ni-Cu alloy films electrodeposited at low and high pH levels, J. Alloys Compd. 453 (2008) 15-19.

[7] A. Panda and E. J. Podlaha, Nanoparticles to improve mass transport inside deep recesses, Electrochem. Solid St., 6 (11) (2003) C149-C152.

[8] Y. C. Chen, W. Liu, T. Chao, and Y. T. Cheng, An optimized Cu-Ni nanocomposite coil for low-power electromagnetic microspeaker fabrication, Transducers (2009) 25-28.

[9] Y. W. Huang, T. Chao, C. C. Chen, and Y. T. Cheng, Power consumption reduction scheme of magnetic microactuation using electroplated Cu–Ni nanocomposite, App. Phys. Letters 90 (2007) 1-3.

[10] Z. Huang, X. Peng, and F. Wang, Preparation and oxidation of novel electrodeposited Cu–Ni–Cr nanocomposites, Oxid. Met. 65 (3/4) (2006) 223-235.

[11] Z. Huang, X. Peng, C. Xu, and F. Wang, On the exclusive growth of external chromia scale on the novel electrodeposited Cu–Ni–Cr nanocomposites, J. Mater. Res. 22 (11) (2007) 3166-3177.

[12] M. Metikos-Hukovic, I. Skugor, Z. Grubac and R. Babic, Complexities of corrosion behaviour of copper–nickel alloys under liquid impingement conditions in saline water, Electrochim. Acta 55 (2010) 3123-3129.

[13] V.A.R. Boyapati, C.K. Kanukula, Corrosion inhibition of Cu-Ni (90/10) alloy in seawater and sulphide-polluted seawater environments by 1, 2, 3-Benzotriazole, ISRN Corros. 2013 (2013) 1-22.

[14] B.E.T. Bautista, M.L. Carvalho, A. Seyeux, S. Zanna, P. Cristiani, B. Tribollet, P. Marcus and I. Frateur, Effect of protein adsorption on the corrosion behavior of 70Cu-30Ni alloy in artificial seawater, Bioelectroch. 97 (2014) 34-42.

[15] I. Milosev and M. Metikos-Hukovic, The behaviour of Cu-xNi (x = 10 to 40 wt%) alloys in alkaline solutions containing chloride ions, Electrochim. Acta 42 (1997) 1537-1548.

[16] A.J. Bard and L.R. Faulkner, Electrochemical Methods: Fundamentals and Applications, New York, 2000.

[17] R.A. Horch, T.D. Golden, N.A. D' Souza and L. Riester, Electrodeposition of nickel/montmorillonite layered silicate nanocomposite thin films, Chem. Mater. 14 (2002) 3531-3538.

[18] A. Gomes, I. Pereira, B. Fernández, and R. Pereiro, Electrodeposition of metal matrix nanocomposites: Improvement of the chemical characterization techniques, Advances in Nanocomposites - Synthesis, Characterization and Industrial Applications 21 (2011) 503-526.

[19] W.C. Harrigan, Commercial processing of metal matrix composites, Mater. Sci. Eng. A244 (1998) 75–79.

[20] X. Zeng, Z. Tao, B. Zhu, E. Zhou and K. Cui, Investigation of laser cladding ceramic-metal composite coatings: processing modes and mechanisms, Surf. Coat. Tech. 79 (1996) 209-217.

[21] V. K. Lindroos and M. J. Talvitie, Recent advances in metal matrix composites, J. Mater. Process. Tech. 53 (1995) 273-284.

[22] R. L. Deuis, J. M. Yellup and C. Subramanian, Metal-matrix composite coatings by PTA surfacing, Compos. Sci. Technol. 58 (1998) 299-309.

[23] J. Hashim, L. Looney and M.S.J. Hashmi, Metal matrix composites: production by the stir casting method, J. Mater. Process. Tech. 92-93 (1999) 1-7.

[24] M. Muratoglu, O. Yilmaz and M. Aksoy, Investigation on diffusion bonding characteristics of aluminum metal matrix composites (Al/SiCp) with pure aluminum for different heat treatments, J. Mater. Process. Tech.178 (2006) 211–217.

[25] M.J. Tan and X. Zhang, Powder metal matrix composites: selection and processing, Mater. Sci. Eng. A244 (1998) 80–85.

[26] N. Popovskaa, H. Gerhard, D. Wurm, S. Poscher, G. Emig, R. F. Singer, Chemical vapor deposition of titanium nitride on carbon fibres as a protective layer in metal matrix composites, Mater. Design 18 (4/6) (1997) 239-242.

[27] M. Musiani, Electrodeposition of composites: an expanding subject in electrochemical materials science, Electrochim. Acta 45 (2000) 3397–3402.

[28] F. C. Walsh and C. Ponce de Leon, A review of the electrodeposition of metal matrix composite coatings by inclusion of particles in a metal layer: an established and diversifying technology, Trans. Inst. Met. Finish. 92 (2) (2014) 83-98.

[29] A. Hovestad and L. J. J. Jansen, Electrochemical codeposition of inert particles in a metallic matrix, J. Appl. Electrochem. 25 (1995) 519-527.

[30] H. Chiriac, A. E. Moga, and V. A. Constantin, Synthesis and magnetic properties of Fe-Ni and Cu-Ni composite coatings, J. Optoelectron Adv. M. 9 (4) (2007) 1161-1164.

[31] A. Chrobak, M. Kubisztal, J. Kubisztal, E. Chrobak, and G. Haneczok, Microstructure, magnetic and elastic properties of electrodeposited Cu+Ni nanocomposites coatings, J. Achieve. Mater. Manufac. Engineering 49 (1) (2011) 17-26.

[32] M. Rosso, Ceramic and metal matrix composites: Routes and properties, J. Mater. Process. Tech. 175 (2006) 364–375.

[33] A.K. Pradhan and S. Das, Pulse-reverse electrodeposition of Cu–SiC nanocomposite coating: Effect of concentration of SiC in the electrolyte, J. Alloy Compd. 590 (2014) 294–302.

[34] I. Zamblau, S. Varvara and L.M. Muresan, Corrosion behavior of Cu–SiO_2 nanocomposite coatings obtained by electrodeposition in the presence of cetyl trimethyl ammonium bromide, J. Mater. Sci. 46 (2011) 6484–6490.

[35] S. Ramalingam, V. S. Muralidharan and A. Subramania, Electrodeposition and characterization of Cu-TiO_2 nanocomposite coatings, J. Solid State Electrochem. 13 (2009) 1777–1783.

[36] Y. Gan, D. Lee, X. Chen and J.W. Kysar, Structure and properties of electrocodeposited Cu–Al_2O_3 nanocomposite thin films, J. Mater. Process. Tech. 127 (2005) 451-456.

[37] V. Mangam, S. Bhattacharya, K. Das and S. Das, Friction and wear behavior of Cu–CeO_2 nanocomposite coatings synthesized by pulsed electrodeposition, Surf. Coat. Tech. 205 (2010) 801–805.

[38] D.E. Rusu, P. Cojocaru, L. Magagnin, C. Gheorghies and G. Carac, Study of Ni-TiO_2 nanocomposite coating prepared by electrochemical deposition, J. Optoelectron Adv. M. 12 (2010) 2419-2422.

[39] R. Sen, S. Das and K. Das, Synthesis and properties of pulse electrodeposited Ni-CeO_2 nanocomposite, Metall. Mater. Trans. A 43A (2012) 3809-3823.

[40] M.R. Vaezi, S.K. Sadrnezhaad and L. Nikzad, Electrodeposition of Ni–SiC nano-composite coatings and evaluation of wear and corrosion resistance and electroplating characteristics, Colloids and Surf. A 315 (2008) 176-182.

[41] L.M. Chang, J.H. Liu and R.J. Zhang, Corrosion behaviour of electrodeposited Ni/Al_2O_3 composite coating covered with a NaCl salt film at 800 °C, Mater. Corros. 62 (2011) 920-925.

[42] S. Kasturibai and G.P. Kalaignan, Physical and electrochemical characterizations of Ni-SiO_2 nanocomposite coatings, Ionics (2012) 1-8.

[43] H.A. Conrad, J.R. Corbett and T.D. Golden, Electrochemical deposition of γ-phase zinc-nickel alloys from alkaline solution, J. Electrochem. Soc. 159 (2012) C29-C32.

[44] Y.H. Ahmad, A.M.A. Mohamed, T.D. Golden, and N. D'Souza, Electrodeposition of nanocrystalline Ni-Mo alloys from alkaline glycinate solutions, Int. J. Electrochem. Sci. 9 (2014) 6438-6450.

[45] S.J. Yuan and S.O. Pehkonen, Surface characterization and corrosion behavior of 70/30 Cu–Ni alloy in pristine and sulfide-containing simulated seawater, Corros. Sci. 49 (2007) 1276-1304.

[46] C.T.J. Low, R.G.A. Wills and F.C. Walsh, Electrodeposition of composite coatings containing nanoparticles in a metal deposit, Surf. Coat. Tech. 201 (2006) 371–383.

[47] M. H. Fawzy, M. M. Ashour, and Abd El-Halim, Effect of some operating variables on the characteristics of electrodeposited Cu-Ni alloys with and without α-$A1_2O_3$ and TiO_2 inert particles, J. Chem. Tech. Biotechnol. 66 (1996) 121-130.

[48] M. Hashemi, Sh. Mirdamadi, H.R. Rezaie, Effect of SiC nanoparticles on microstructure and wear behavior of Cu-Ni-W nanocrystalline coating, Electrochim. Acta 138 (2014) 224–231.

[49] Y.Z. Wan, Y.L. Wang, H.L. Luo, X.H. Dong, G.X. Cheng, Effects of fiber volume fraction, hot pressing parameters and alloying elements on tensile strength of carbon fiber reinforced copper

matrix composite prepared by continuous three-step electrodeposition, Mater. Sci. Eng. A288 (2000) 26–33.

[50] X. Cui, W. Wei, H. Liu, and W. Chen, Electrochemical study of codeposition of Al particle—Nanocrystalline Ni/Cu composite coatings, Electrochim. Acta 54 (2008) 415–420.

[51] R. V. Williams and P. W. Martin; Electrodeposited composite coatings, Trans. Inst. Met. Finish. 42 (1964) 182-187.

[52] E. A. Brandes and D. Goldthorpe, Co-deposition of metals and ceramic particles, Metallurgia. 76 (1967) 195–198.

[53] N. Guglielm, Kinetics of the deposition of inert particles from electrolytic baths, J. Electrochem. Soc., 119 (8) (1972) 1009-1012.

[54] J.P. Celis, J.R. Roos and C. Buelens, A mathematical model for the electrolytic codeposition of particles with a metallic matrix, J. Electrochem. Soc. 134 (1987) 1402–1408.

[55] P. Bercot, E. Pena-Munoz and J. Pagetti, "Electrolytic composite Ni PTFE coatings: An adaptation of Guglielmi's model of the phenomena of incorporation, Surf. Coat. Technol. 157 (2002) 282–289.

[56] E.J. Podlaha, C. Bonhôte and D. Landolt, A mathematically model and experimental study of the electrodeposition of Ni-Cu alloys from complexing electrolytes, Electrochim. Acta 39 (1994) 2649-2657.

[57] S. Rode, C. Henninot and M. Matlosz, Complexation chemistry in nickel and copper-nickel alloy plating from citrate baths, J. Electrochem. Soc. 152 (2005) C248-C254.

[58] R.Y. Ying, P.K. Ng, Z. Mao and R.E. White, Electrodeposition of Cu-Ni alloys from citrate solutions on a rotating disk electrode, J. Electrochem. Soc. 135 (1988) 2964-2971.

[59] A. Karimbeigi1, A. Zakeri1, A. Sadighzadeh. Iranian Journal of Materials Science & Engineering 10 (3) (2013) 27.

[60] X-ray Diffraction in Powders. http://www.physics.rutgers.edu/ugrad/389/xrays/xrays.pdf

[61] V. Williams. (1996), http://www.eng.vt.edu/eng/materials/classes/MSE2094_NoteBook/96ClassProj/examples/cu-ni.html

[62] Suryanarayana C.; Norton, M.G. X-Ray Diffraction: A Practical Approach. Plenum Press, New York, 1998.

[63] W. Schleich, R. Feser, G. Schmitt, S. Haarmann and K. Schnier, Eurocorr, CDA Publication (2007) 1-14.

[64] J. Tientong, C.R. Thurber, N. D'Souza, A.M.A. Mohamed, and T.D. Golden, Influence of bath composition at acidic pH on electrodeposition of nickel-layered silicate nanocomposites for corrosion protection, Int. J. Electrochem. 2013 (2013) 1-8.

[65] J. Tientong, Y.H. Ahmad, M. Nar, N. D'Souza, A.M.A. Mohamed and T.D. Golden, Improved mechanical and corrosion properties of nickel composite coatings by incorporation of layered silicates, Mater. Chem. and Phys. 145 (2014) 44-50.

[66] Y.H. Ahmad, J. Tientong, N. D'Souza, T.D. Golden and A.M.A. Mohamed, Salt water corrosion resistance of electrodeposited Ni-layered silicate nanocomposite coatings from Watts' Type Solution, Surf. Coat. Tech. 242 (2014) 170-176.

[67] C.R. Thurber, M.C. Calhoun, Y.H. Ahmad, N. D'Souza, A.M.A. Mohamed, T.D. Golden, Electrodeposition of Cu-Ni incorporated with layered silicates for corrosion protection, ECS Trans. 61 (20) (2014) 49-60.

[68] C.R. Thurber, Y.H. Ahmad, S.F. Sanders, A. Al-Shenawa, N. D'Souza, A.M.A. Mohamed and T.D. Golden, Electrodeposition of 70-30 Cu-Ni nanocomposite coatings for enhanced mechanical and corrosion properties, Curr. Appl. Phys., 16 (2016) 387-396.

[69] Y.Y. Chang, D.Y. Wang, Corrosion behavior of electroless nickel-coated AISI 304 stainless steel enhanced by titanium ion implantation, Surf. Coat. Tech. 200 (2005) 2187-2191.

[70] P.T. Tang, Pulse reversal plating of nickel alloys, Institute of Metal Finishings 85 (2007) 51-56.

[71] Painting: New Construction and Maintenance, U.S Army Corps of Engineers EM 1110-2-3400, 2-1 1995.

CHAPTER 4

ELECTRODEPOSITION OF 70-30 COPPER NICKEL NANOCOMPOSITE COATINGS FOR ENHANCED MECHANICAL AND CORROSION PROPERTIES

*Parts of this chapter have been previously published, either in part or in full, from C.R. Thurber, Y.H. Ahmad, Stephen F. Sanders, Amaal Al-Shenawa, N. D'Souza, A.M.A. Mohamed, T.D. Golden "Electrodeposition of 70-30 Cu-Ni Nanocomposite Coatings for Enhanced Mechanical and Corrosion Properties" Current Applied Physics, 16 (2016) 387-396. Reproduced with permission from Elsevier.

4.1 Introduction

Composite coatings that slow the rate of corrosion at a reduced cost have been extensively studied over the past several years. Exposing films to an unfavorable environment accelerates the degradation of the film which can lead to multiple types of corrosion [1-4]. The rate of corrosion can be reduced using five general approaches which include the selection of materials, chemical inhibitors, changes in the environment, cathodic protection, or the addition of coatings [5]. Coatings can be produced by several different methods, and electrodeposition remains a prominent technique to produce novel materials for science and engineering applications because of low cost, convenience, ability to work at low temperatures and the ease of treatment to large and complex geometries [6, 7].

One important route to increase the corrosion resistance of materials is the deposition of metallic alloys such as Zn-Ni, Ni-Mo, and Cu-Ni [8-10]. The alloyed coatings typically enhance the corrosion resistant properties but they possess mechanical properties that relate to the individual metals. Incorporating ceramic nanoparticles such as TiO_2, CeO_2, SiC, Al_2O_3, and ZrO_2 into the matrix of different coatings enhances the lifetime and performance of the coating [11-15]. However, addition of ceramics can lead to problems with delamination and brittleness producing shorter service times. Some silicates that have been used in composites are layered silicates [16-20]. Layered silicates have several advantageous properties such as a high surface area, chemical inertness, resistance to extreme temperatures, and resistance to pH changes [16-20]. MMT is the

layered silicate being evaluated in this study, which is a platelet that measures ~1 nm in height and 1-2 microns in width [7]. One of the benefits of MMT over traditional spherical particles is its larger surface area, which helps to provide a more tortuous mean free path of corrosion. Also, MMT is a cationic clay with a negatively charged surface, which allows positively charged metal ions to be attracted to the surface, which helps to increase incorporation of the platelets into the metal matrix during the electrodeposition process. The addition/embedding of MMT into a pure nickel matrix was associated with an increase in hardness, adhesion, and corrosion resistance as shown in our previous work [4, 21, 22].

Alloys involving copper have been studied because of their machinability and resistance to biofouling [23]. Cu-Ni coatings used for several applications, such as decoration, microelectronics, corrosion resistant films, piping materials for the ship building industry, condensers, and heat exchangers have been analyzed over the years [24-31]. In the off-shore oil industry, two important properties, high corrosion resistance and hardness, are needed to extend the lifetime of coatings experiencing exposure to high stress and salt environments. Copper alloys are used in marine environments to defend against biofouling of materials by inhibiting microbial induced corrosion (MIC) [30-34]. Copper ions resist the growth of bacteria, viruses, fungi, algae and other microbes on the surface of the coating by reducing adhesion [29]. A popular alloy used is the 70-30 Cu-Ni (Alloy C71500) [31, 35, 36]. These alloys exhibit good corrosion resistance due to the growth of a protective layer at the surface of the coating [32, 35]. The coating is comprised of a thin, strongly adherent inner Cu_2O layer acting as a barrier, in contact with the outer solution through a porous dense outer Cu(II) hydroxide/oxide layer [24].

In this work, Cu-Ni-MMT coatings were electrodeposited to improve corrosion and mechanical properties of the copper-nickel alloys. Citrate was utilized as the ligand to stabilize

the electrolyte system. Citrate is a regularly used ligand for transition metal electrodeposition, and has been used effectively as a complexing agent for the deposition of Cu-Ni coatings [37-41]. There are pH restrictions when using citrate, due to an insoluble citrate complex forming and precipitating out of solution [37]. The distribution of citrate in the electrolyte as a function of composition, temperature and pH has been analyzed to try and stabilize the bath for longer periods of time [37]. It was observed that at the native pH of 4.1, the solution was unstable and a precipitate formed within a few days [37]. Solutions with citrate at pH 6.0 were found to be stable for several weeks with no precipitate formation [37]. For our study, the Cu-Ni citrate complex at pH 6.0 was used for the electrodeposition with MMT because of the proven long term stability.

4.2 Materials and Methods

4.2.1 Materials and Electrodeposition Procedure

The layered silicate used in the coatings was MMT from Southern Clay Products. The MMT (0.05, 0.1, 0.2%) was stirred over a 24 hour period to achieve exfoliated layered silicate platelets. 0.25 M trisodium citrate dihydrate (Fisher Scientific) was utilized as the ligand to stabilize the 70-30 Cu-Ni complex. 0.32 M nickel ammonium sulfate hexahydrate (Alfa Aesar) and 0.06 M copper sulfate pentahydrate (Fisher Scientific) were used as the metal salts. The prepared baths were adjusted to a pH of 6 with 2.0 M sodium hydroxide. The 1.8 cm^2 430 stainless steel substrates (Ted Pella) were polished with 600, 800, and 1000 grit silicon carbide paper, then with a 3 μm diamond suspension on a felt cloth. The polished electrodes were then sonicated in deionized water for 10 minutes and soaked in 5.0 M H_2SO_4 for 30 seconds before use.

An EG&G Princeton Applied Research Model 273A potentiostat/galvanostat was used for the electrodeposition, cyclic voltammetry, immersion test and Tafel analysis. The electrochemical

system was made up of a three electrode system. The working, counter and reference electrodes were a stainless steel substrate, coiled chromel wire, and a saturated calomel reference (SCE), respectively. The solution was purged with N_2 for 15 minutes before deposition. Green *et. al.* [37] reported that the stainless steel should be pre-treated prior to deposition of the copper-nickel coating to attain good adhesion. For the pretreatment, a Ni-MMT bath was used from a previous method to deposit a very thin layer [4]. The deposition conditions were 25°C with E_{app} at -1.0 V until 30 coulombs of charge were obtained for the Cu-Ni films. The adhesion of the Cu-Ni and Cu-Ni-MMT coatings were measured on a DeFelsko, PosiTest AT-A (automatic) Pull-Off Adhesion Tester, and were all found to be greater than 75 N/mm^2. The Cu-Ni coatings were immersed in a 3.5% NaCl solution at 25°C for 14 days while monitoring open circuit potential. The film thickness over different charge amounts for the coatings were measured using a Veeco Dektak 8 Stylus Profilometer.

4.2.2 Characterization Studies

The zeta potential and particle size of the Cu-Ni plating solutions were measured using a Delsa Nano-C (Beckman-Coulter Instruments). The Cu-Ni solutions were allowed to adjust to 25°C for 60 seconds using a peltier device in the instrument before data collection.

Atomic absorption spectroscopy (AAS) (Perkin Elmer Analyst 300) analysis was performed using the standard addition method to determine the optimal ratio of 70-30 Cu-Ni. X-ray diffraction (XRD) was used to analyze the crystal structure and particle size of the films. XRD (Siemens D-500 Diffractometer) was performed using the Cu Kα radiation $\lambda = 0.15406$ nm at 35 kV and 24 mA. The scans were obtained from 40-100° 2θ for the Cu-Ni coatings.

Scanning electron microscopy (SEM) and atomic force microscopy (AFM) were chosen to analyze the morphology and roughness of the electrodeposited coatings. The micrographs of the coatings were obtained using an Environmental FEI Quanta 200 scanning electron microscope with an Everhart Thornley detector. Energy dispersive spectroscopy (EDS) was used to determine the elemental composition of Cu-Ni and the layered silicate (Al and Si) in the composite coatings. A 3D surface topography of pure Cu-Ni and Cu-Ni-MMT coatings with various MMT concentrations was recorded by an AFM analyzer at a scan rate of 1.00 Hz and scan size 1.0 μm. AFM measurements were performed under ambient conditions using standard topography AC air (tapping mode in air).

The mechanical properties of the films was analyzed using microhardness and sheer strength testing. Microhardness was measured using a HMV-M Shimadzu microhardness testing machine model M3 (Kyoto, Japan). The applied load was 300 g for 10 s. For each test, three readings were done to represent the average value of microhardness. Sheer adhesion tests were measured using the XYZTEC instrument paired with a 2 mm wide knife. The knife was placed at 5 μm above the substrate-coating interface and moved 2 mm horizontally at a velocity 150 μm/s without hold time. The force to move as a function of distance was noted. The adhesive strength is the maximum recorded force divided by the area width of the knife X test distance. The test was repeated 6 times for each sample and the average of the values and standard deviation were calculated.

Corrosion behavior was analyzed by linear polarization techniques and electrochemical impedance spectroscopy (EIS) after a 2 week immersion in 3.5% NaCl at 25°C. A three electrode electrochemical cell was used as the corrosion testing system which comprised of the working electrode films, two counter graphite rods, and a SCE as the reference electrode. A ±150 mV

potential range was applied to the cell with a scan rate of 1 mV/s; the resulting current densities were then measured. EIS was performed in a three-electrode cell (where the working electrode is the coating layer) using a Bio-Logic Potentiostat/Galvanostat equipped with a software EC-Lab version 10.2. In the impedance measurements, an input signal of 10 mV peak to peak was applied in the frequency domain of 0.1-10^5 Hz.

4.3 Results and Discussion

4.3.1 Cyclic Voltammetry and Electrodeposition

Cyclic voltammetry (CV) was utilized to evaluate the effect of MMT on the reduction potential and the current response at the reduction potential. CV was run at scan rates of 5, 20, 50, and 100 mV/s. The CVs in Figure 4.1 (run at 50 mV/s) for the Cu-Ni 70-30 baths with and without MMT, showed that there was no observed change in the reduction potential (-0.49 V) of copper or in the i_{pc} (cathodic peak current) when 0.05 to 0.2% MMT was loaded into the Cu-Ni plating bath. MMT did not change the reduction potential or current for copper deposition at the other scan rates also. The reduction peak for nickel is not observed due to hydrogen evolution. The anodic peak present at 0.32 V relates to the dissolution of the Cu-Ni complex. Varea *et. al.* [26] discovered a large deviation in the amount of copper in Cu-Ni depositions by varying the voltage from -1.0 to -1.075 V, which lead to the conclusion that Cu deposition is diffusion-controlled and Ni deposition is charge transfer-controlled. The main difference in the voltammograms was that the MMT slightly pushed the hydrogen evolution more cathodic. This result revealed that the MMT platelets do not disrupt the redox potential for the deposition of the Cu-Ni.

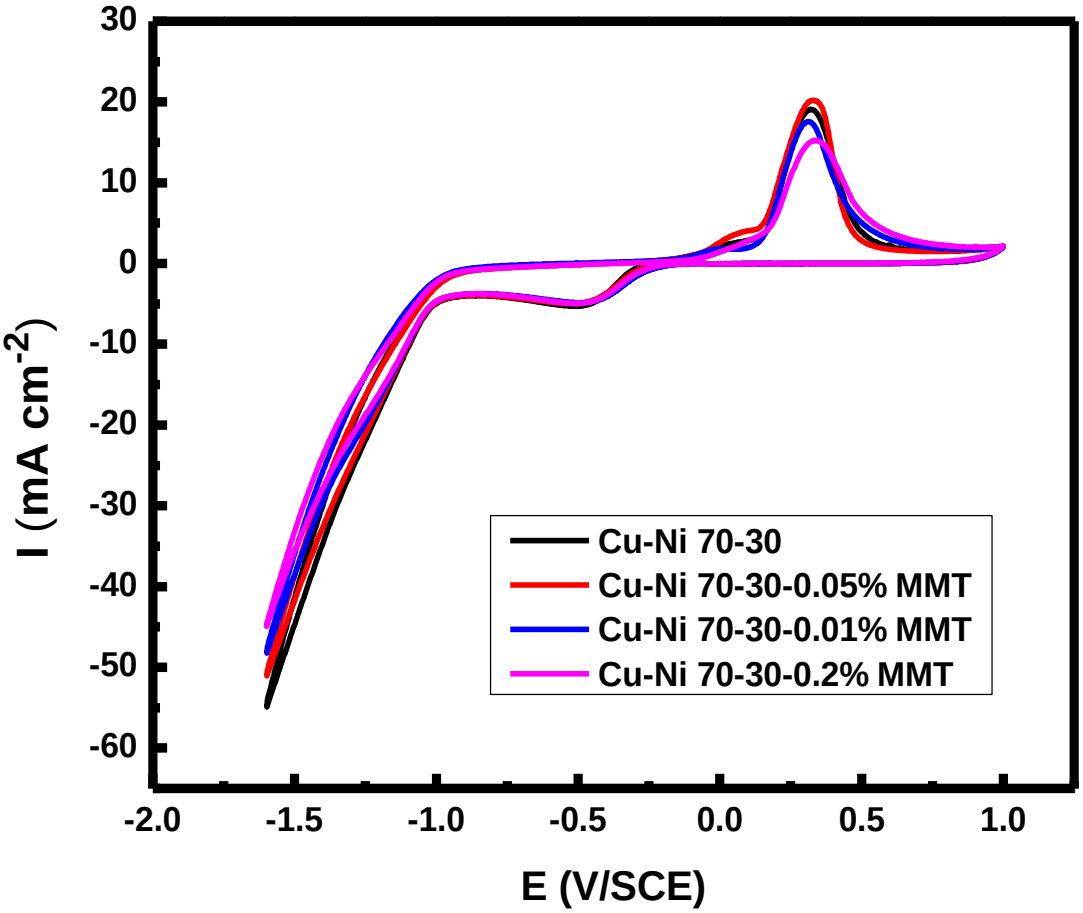

Figure 4.1: Cyclic voltammograms of the 70-30 Cu-Ni films incorporated with MMT run at a scan rate of 50 mV/s.

Film thickness was measured over different charge amounts for pure Cu-Ni and Cu-Ni-MMT coatings to see if the MMT affected the deposition efficiency of the coatings. Table 4.1 shows coatings at 10 C, 20 C, and 30 C of charge for 70-30 Cu-Ni and 70-30 Cu-Ni-0.2% MMT. Graphical analysis revealed a linear increase in thickness for the pure Cu-Ni (R^2 = 0.9985) and Cu-Ni-MMT (R^2 = 0.9979) over the three charge amounts. The data showed that the growth of

the film was the same for pure Cu-Ni and Cu-Ni incorporated with MMT, which meant MMT also had no effect on the deposition efficiency.

Table 4.1: Thickness of the film versus total deposition charge to plate the film for 70-30 Cu-Ni and 70-30 Cu-Ni-0.2% MMT.

Cu-Ni Coatings		Cu-Ni-0.2% MMT Coatings	
Deposition Charge (C)	Film Thickness (μm) (n=3)	Deposition Charge (C)	Film Thickness (μm) (n=3)
10	2.42 ± 0.03	10	2.42 ± 0.04
20	4.27 ± 0.04	20	4.26 ± 0.05
30	6.39 ± 0.07	30	6.42 ± 0.05

4.3.2 Particle Size and Zeta Potential

The particle size and zeta potential (Table 4.2) of the Cu-Ni solutions were measured to test the stability of the plating solution (dispersion) after addition of MMT. The particle sizes of MMT in aqueous solution ranged from 440 to 540 nm for the three different concentrations. The particle size for the 70-30 Cu-Ni solutions increased as the concentration of MMT increased in the solution due to MMT platelet agglomeration. The metal ions in solution associate with the charged MMT platelets and promote agglomeration. This has been noted previously for nickel ions and MMT in solution [7]. Size of the MMT platelets can also be affected by the exfoliation method. In a previous study, a 0.5% MMT solution was prepared by stirring for 24 hours giving a particle size of 591 nm and then the solution was ultrasonicated for one hour, which decreased the particle size to 231 nm [21]. The exfoliated MMT solutions of 0.05%, 0.1%, and 0.2% had zeta potentials around -39 mV. The exfoliated MMT is stable and able to disperse into the aqueous solution while the non-exfoliated MMT precipitates. For more stable suspensions, the ideal zeta potential would be a value more negative than -25 mV. The Cu-Ni-MMT plating solutions were around -19 to -20 mV. The adsorption of the Ni and Cu at the surface of the MMT platelet, moves the zeta potential towards a more positive value and helps to increase the particle size, which slightly

decreases the electrostatic stabilization of the dispersion compared to pure MMT solution. However, the plating solutions still had enough stability for deposition purposes to stay suspended in solution throughout the deposition cycle producing viable coatings every 9 out of 10 times. Understanding the surface forces and tuning of the charges between the platelets and the electrode surface are essential for the incorporation of clay particles into the metal matrix during deposition [21]. To understand the complete mechanism for these metal composite films, further studies need to be examined.

Table 4.2: Particle Size and Zeta Potential for MMT in aqueous solution and the 70-30 Cu-Ni-MMT Plating Solutions.

Solutions	Particle Size (nm) (n=3)	Zeta Potential (mV) (n=3)
0.05% MMT	440 ± 15	-38.8 ± 0.5
0.1% MMT	500 ± 20	-39.2 ± 0.5
0.2% MMT	540 ± 10	-38.7 ± 0.4
Cu-Ni-0.05% MMT	2680 ± 80	-20.2 ± 0.7
Cu-Ni-0.1% MMT	2930 ± 70	-19.5 ± 0.6
Cu-Ni-0.2% MMT	3260 ± 60	-19.2 ± 0.7

4.3.3 X-ray Diffraction

Copper and nickel both have a face centered cubic (fcc) crystal structure and are both similar in atomic size. The binary phase diagram for Cu-Ni shows complete solubility of copper into nickel in the liquid and solid state [42]. Hence, the Cu-Ni alloy is known as an isomorphous binary alloy, which means the two metals are completely soluble in one another and have one type of crystal structure. Varea *et.al.* [26] showed that the (111) and (200) reflections shifted towards higher angles as the amount of copper decreased in the coating indicating an increase in the lattice parameter, which falls in agreement with Vegard's law.

XRD patterns were analyzed to evaluate the crystal structure and the particle size of the Cu-Ni and Cu-Ni-MMT composite coatings. Figure 4.2A shows that deposition conditions favor a

(111) preferred orientation. Only one major peak is present for the Cu-Ni alloy at a 2θ value of 43.6°, which is shifted between values for pure copper at 43.297° (PDF # 00-004-0836) and pure nickel at 44.508° (PDF # 00-004-0850). The peak present for the 70-30 Cu-Ni alloy at 43.6° corresponds to the preferred (111) orientation. Figures 4.2B-D show peak broadening of the (111) peak with the addition of MMT, which indicates a decrease in particle size and that the Cu-Ni structure is becoming amorphous. The particle size (L) for each film was calculated using the Scherrer equation:

$$B_r = k\lambda/L \cos \theta \quad (4.1)$$

The Gaussian peak fit method of $B_r^2 = B_o^2 - B_i^2$ was used to calculate the peak broadening, where B_o is the peak broadening of the coating and the B_i is the instrumental broadening calculated using a silicon standard. The proportionality constant k was assumed to be 1, $\lambda = 0.15406$ nm from the Cu Kα radiation, and θ is the position of the (111) peak. The calculated particle sizes listed in Table 4.3, showed the particle size decreased for the coatings incorporated with MMT. The decrease in particle size with the incorporation of MMT strengthens the grain refinement contribution to hardness, which explains the increase in the hardness of the coatings with embedded MMT.

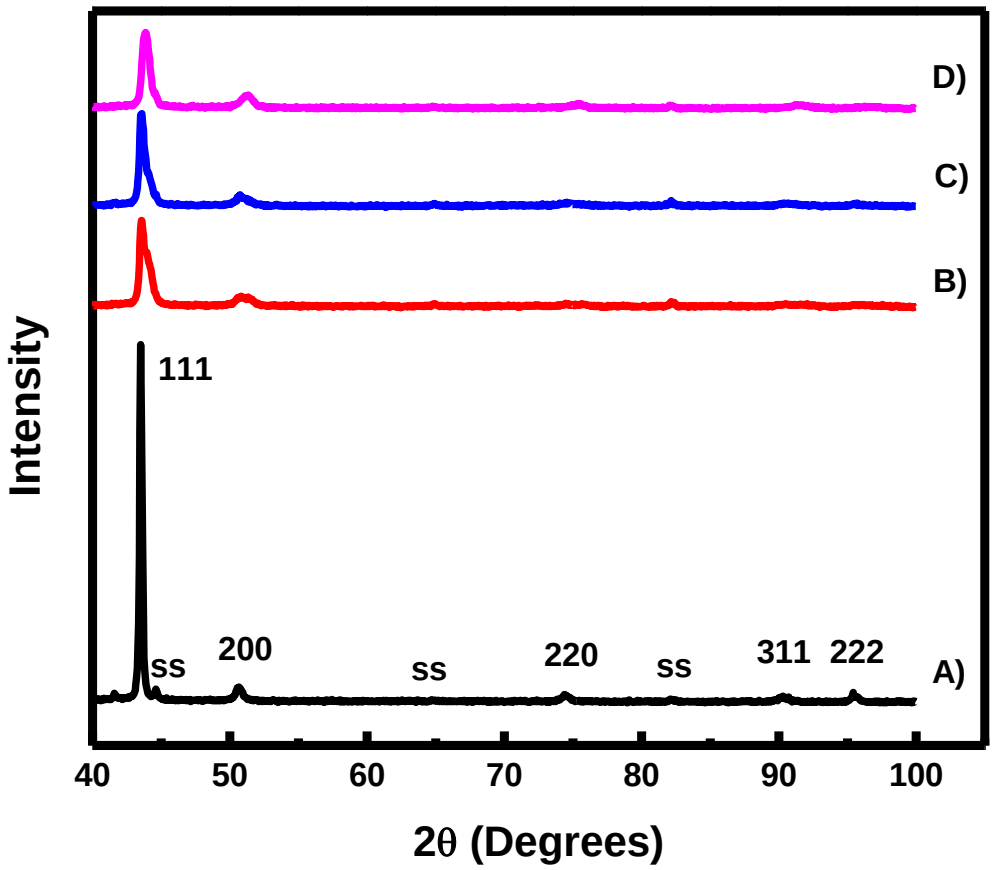

Figure 4.2: X-ray diffraction patterns of: A) 70-30 Cu-Ni, B) 70-30 Cu-Ni-0.05 % MMT, C) 70-30 Cu-Ni-0.1 % MMT, and D) 70-30 Cu-Ni-0.2 % MMT run from 40-100 2θ at a step size of 0.05° and dwell time of 1 sec (SS – stainless steel substrate).

Table 4.3: Particle Sizes of the 70-30 Cu-Ni Coatings Calculated from the Scherrer Equation using X-ray Diffraction.

Coatings	Particle Size (nm) (n=3)
Cu-Ni	62 ± 6
Cu-Ni – 0.05% MMT	16 ± 5
Cu-Ni – 0.1% MMT	15 ± 4
Cu-Ni – 0.2% MMT	15 ± 5

4.3.4 Atomic Absorption Spectroscopy and Energy Dispersion Spectroscopy

Atomic absorption spectroscopy was used to determine the composition of the Cu-Ni coatings. The analysis showed that the composition of 70-30 Cu-Ni was maintained during

deposition at values of copper (71 ± 3%) and nickel (29 ± 3%). Also, EDS was performed to evaluate the Cu, Ni, Si, and Al composition of the coating. The Si and Al were evaluated because they are major components present in MMT. The EDS results in Table 4.4 showed that for the Cu-Ni 70-30 with 0.05% MMT, silicon content was 1.68% and aluminum was 1.09%. For the Cu-Ni 70-30 with 0.1% MMT, silicon content was 2.46% and aluminum was 1.50%. In the Cu-Ni 70-30 with 0.2%, the silicon content was 3.11% and 1.97% for aluminum, which confirmed the presence of MMT in the coatings. Also with the incorporation of MMT into the Cu-Ni matrix, the amount of Cu in the film slightly decreased and Ni slightly increased, indicating that MMT influenced a minor change in the Cu-Ni ratio during the deposition of the alloy. Previous data has shown that Ni adheres to the surface of MMT [7]. Nickel ions are in excess in the solution because of the deposition conditions and most of the copper is complexed with citrate. The slight increase in Ni concentration (and corresponding decrease in Cu) can be attributed to nickel ions adhering to the surface of MMT platelets as they are incorporated into the film.

Table 4.4: Energy Dispersive Spectroscopy of the 70-30 Cu-Ni Coatings incorporated with MMT showing the main elements of MMT (Si and Al) present in the composite coatings.

Coatings	Copper (%)	Nickel (%)	Silicon (%)	Aluminum (%)
Cu-Ni	68.96	31.04	---	---
Cu-Ni – 0.05% MMT	64.15	33.08	1.68	1.09
Cu-Ni – 0.1% MMT	63.91	32.13	2.46	1.50
Cu-Ni – 0.2% MMT	63.54	31.38	3.11	1.97

4.3.5 Scanning Electron Microscopy and Atomic Force Microscopy

Scanning electron microscopy was performed to examine the morphology of the prepared coatings. In Fig. 3, the pure Cu-Ni coating shows a tightly packed and uniform surface with well-defined grain boundaries. The pure Cu-Ni morphology also shows a corner like structure growth indicating a (111) preferred orientation which was observed in the XRD results. Figure 4.3 also

shows that with the incorporation of MMT into the Cu-Ni matrix, a smaller grain size was produced and the grain boundaries became less defined. With the increase in MMT concentration, additional small MMT platelets (red circles) can be observed on the surface, which were confirmed in the EDS results. The platelets at the surface of the coating may also contribute to the surface becoming slightly rougher in the AFM analysis.

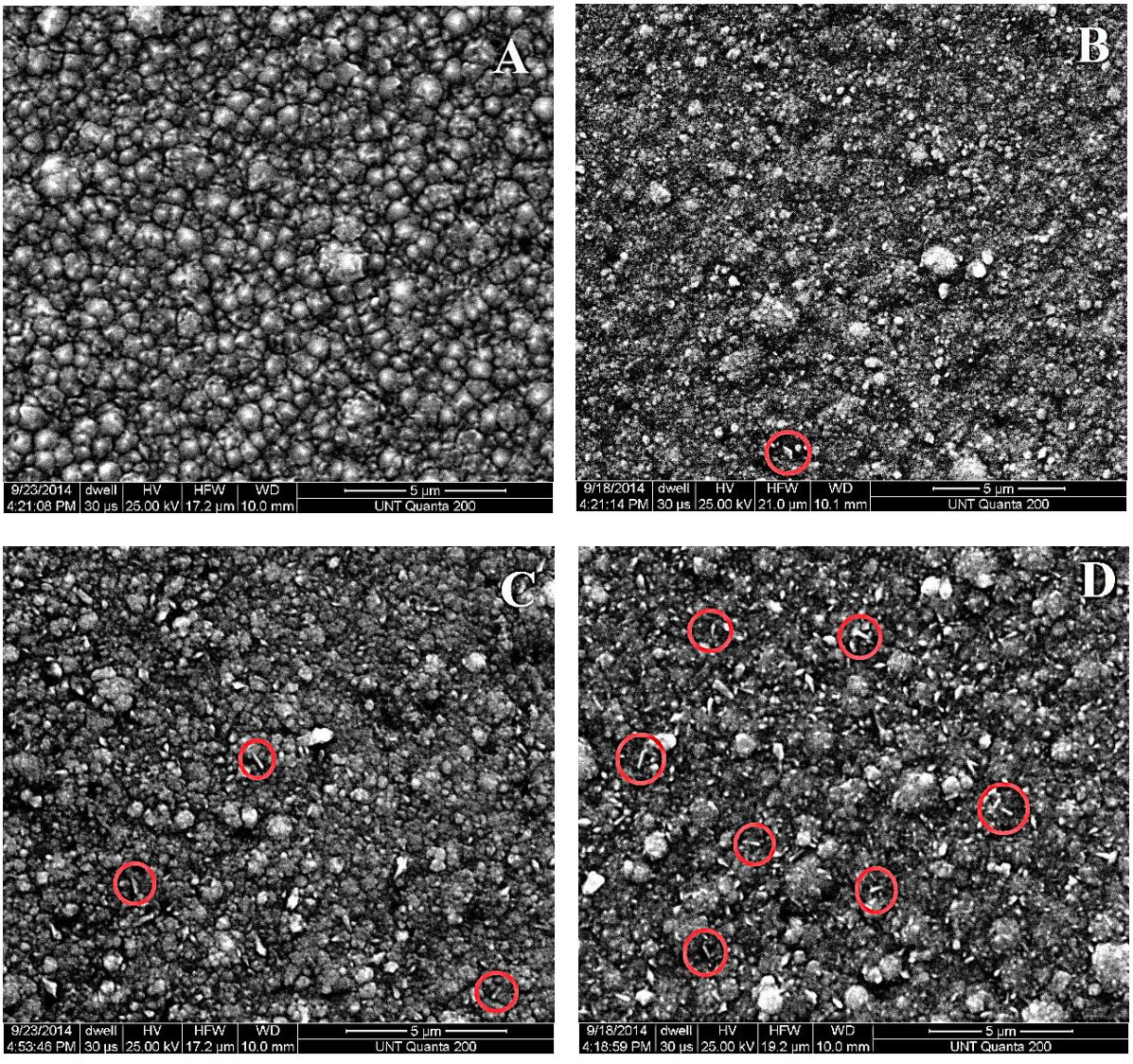

Figure 4.3: SEM micrographs of: A) 70-30 Cu-Ni, B) 70-30 Cu-Ni-0.05 % MMT, C) 70-30 Cu-Ni-0.1 % MMT, and D) 70-30 Cu-Ni-0.2 % MMT. Red circles indicate MMT platelets.

In order to investigate the effect of incorporation of layered silicate into Cu-Ni metallic matrix on the surface roughness, AFM (Figure 4.4) was performed on the surface of the coatings. The surface roughness of different samples were expressed by an average deviation parameter (R_a). The value of this parameter represents the average height of the surface irregularities in the direction perpendicular to the surface. The measured value of R_a of the pure 70-30 Cu-Ni was found to be 15.11 nm whereas the values in case of Cu-Ni-0.05%MMT, Cu-Ni-0.1%MMT and Cu-Ni-0.2%MMT are 17.25, 19.40 and 20.20 nm, respectively. The AFM results show that embedding MMT particles into the Cu-Ni metallic matrix resulted in a slight increase in the surface roughness of the coating.

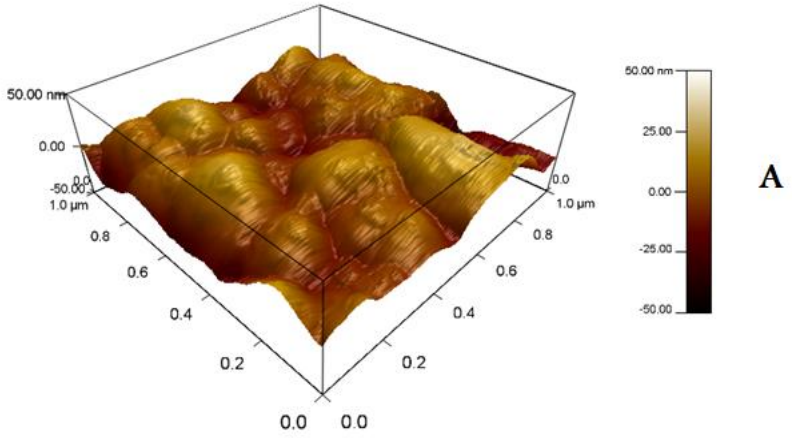

A

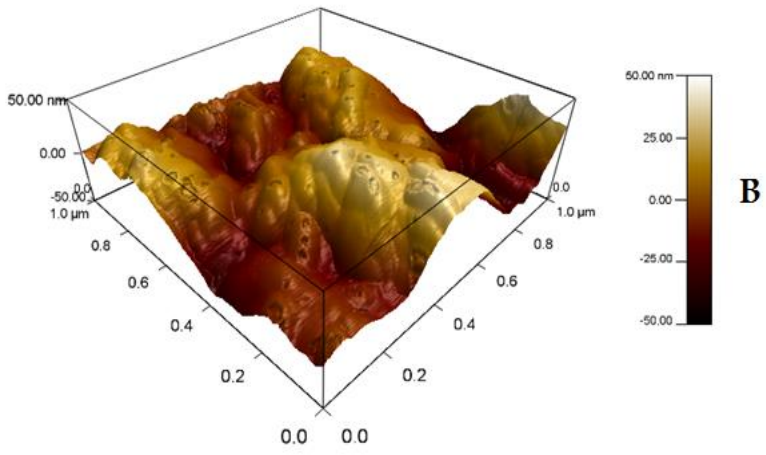

B

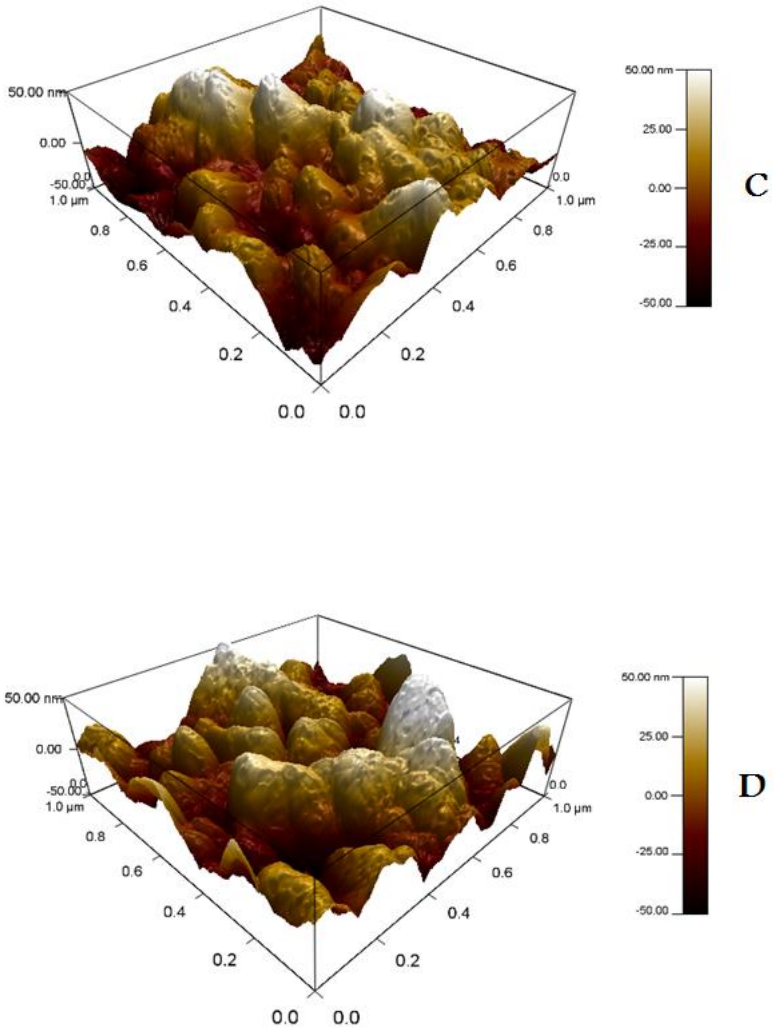

Figure 4.4: AFM micrographs of: A) 70-30 Cu-Ni, B) 70-30 Cu-Ni-0.05 % MMT, C) 70-30 Cu-Ni-0.1 % MMT, and D) 70-30 Cu-Ni-0.2 % MMT.

4.3.6 Hardness

The hardness of metallic matrix composite is mainly governed by two factors; the microstructure of the metallic matrix and the amount of material embedded into the matrix. The microstructure of the metallic matrix is controlled by the parameters of the electrodeposition process including bath concentration of metallic ion, pH, applied voltage and the current density.

Whereas, the amount of the material embedded into the matrix is dependent on its bath concentration, size of particles, solution pH and type of material. MMT has shown the ability to increase the hardness substantially in a pure nickel matrix [21].

The influence of MMT incorporation into the Cu-Ni matrix on microhardness was studied for the composite coatings. Table 4.5 represents the variation of the Cu-Ni-MMT film microhardness with the bath concentration of MMT. The microhardness of the composite coatings increased about 25% with the addition of MMT into the metallic layer. No statistical difference was observed between the different percentages of MMT embedded into the Cu-Ni matrix. This behavior may be attributed to the grain refinement caused by the embedding process which was evident in the particle size measurement from the XRD patterns.

Table 4.5: Vickers Microhardness for the 70-30 Cu-Ni Coatings incorporated with and without MMT.

Coatings	Microhardness (HV) (n=3)
Cu-Ni	185 ± 5
Cu-Ni – 0.05% MMT	219 ± 10
Cu-Ni – 0.1% MMT	221 ± 10
Cu-Ni – 0.2% MMT	232 ± 8

4.3.7 Shear Adhesion strength

The adhesion strength for the coatings are shown in Figure 4.5. As can be seen, the shear adhesion strength of all the nanocomposite coatings exceeds that of the Cu-Ni matrix alone. The presence of the platelets provides enhanced resistance to the knife movement. The approximately 300% improvement in magnitudes for the 0.05% MMT point to the value of the presence of the platelets at low loadings. With increased MMT, the shear resistance decreases. This indicates that the increased amount of platelets in the coating lead to more substrate-platelet contact which would

decrease the effective area of the matrix-substrate contact and lead to decreased adhesion strength. However, the adhesion strength is greater for all MMT loadings compared to the pure Cu-Ni film.

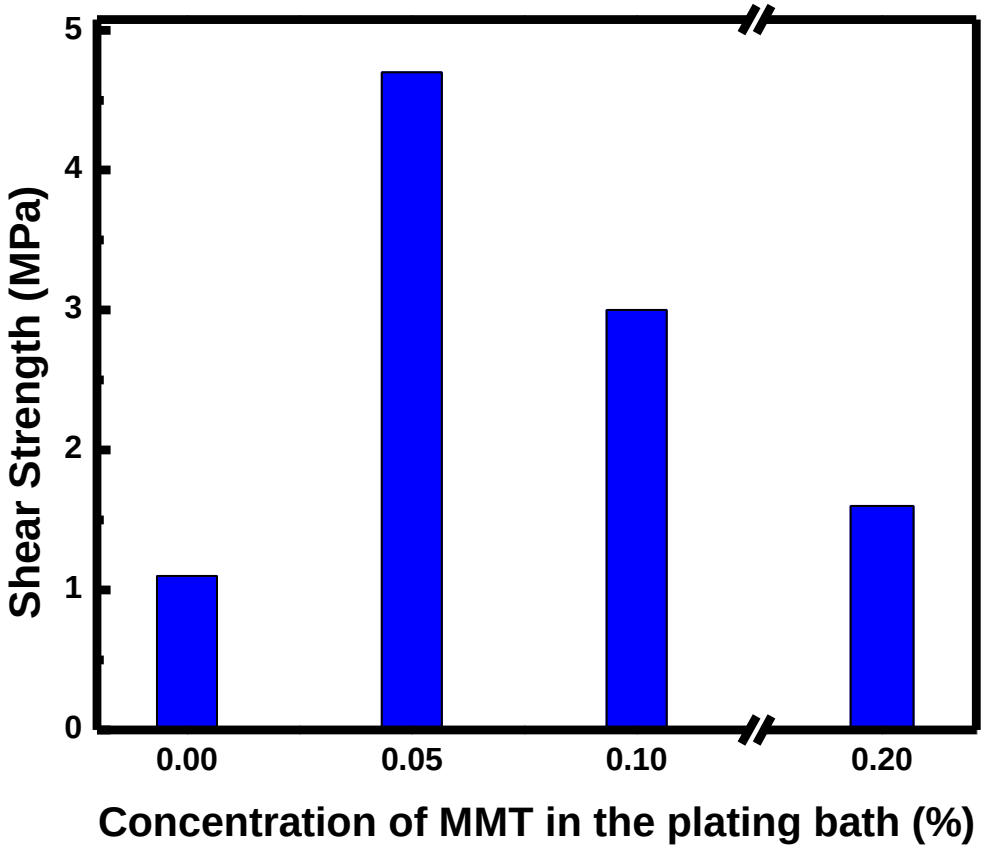

Figure 4.5: The shear adhesion strength of the 70-30 Cu-Ni with different percentages of MMT in the plating solution.

4.3.8 Immersion Study

An immersion test of open circuit potential (OCP) vs. time was performed to evaluate the stability of the Cu-Ni coatings incorporated with and without MMT. Figure 4.6 shows that in a 3.5% NaCl solution, the OCP of the pure Cu-Ni film shifted cathodically after five days followed by the Cu-Ni-0.05% MMT at seven days and the Cu-Ni-0.1% MMT at eleven days. The OCP of Cu-Ni-0.2% MMT stayed stable over the extended period of 14 days. The higher the amount of

MMT in the coating, the more barrier type protection provided as seen in the OCP results. Incorporation of MMT helps slow the mean free path to corrosion. Al-Muhanna *et.al.* [43] also observed a cathodic shift in OCP for 70-30 Cu-Ni in the first 10-15 days of study. Newly deposited Cu-Ni coatings have higher corrosion rates and then the rate drops as an oxide layer builds over time. The protective Cu_2O layer that forms on the surface of Cu-Ni during submersion is a p-type semiconductor with mobile cation vacancies as the main charge carriers. Nickel ions can diffuse into the layer interacting with vacancies to form neutral complexes [24, 44, 45]. Nickel has been found to segregate from the Cu-Ni alloy into the Cu_2O layer of Cu-Ni 70-30 with concentrations increasing up to 45% [24, 44]. With nickel segregated into the outer layers of the film, it may help explain the cathodic shifts observed in the OCP with the pure Cu-Ni, Cu-Ni-0.05% MMT, and Cu-Ni-0.1% MMT because pure nickel is less noble than Cu-Ni, therefore it is observed at more negative potentials. This result shows that MMT slows the rate of nickel segregation into the Cu_2O layer and provides protection with grain refinement and surface area which lessens the mean free path of corrosion for the Cu-Ni matrix, which stabilizes and increases the corrosion resistance. The Cu-Ni-0.2% MMT film has definite enhanced stability for corrosion resistance.

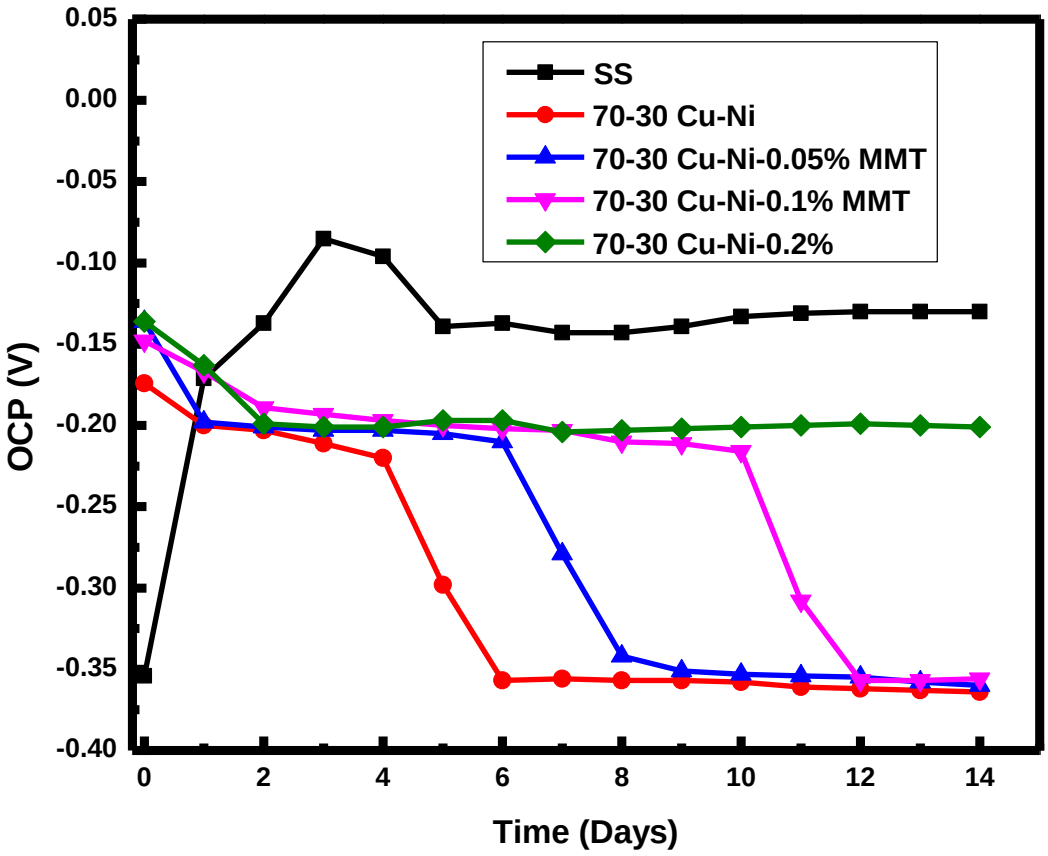

Figure 4.6: Plot of the immersion test for the 70-30 Cu-Ni coatings with and without MMT measured by OCP vs. time for 2 weeks in a 3.5% NaCl solution.

4.3.9 Tafel Analysis

The corrosion resistance of Cu-Ni and Cu-Ni-MMT composite coatings were evaluated using Tafel polarization, as seen in Figure 4.7. The corrosion parameters were measured after immersing the prepared coatings for two weeks in a 3.5% NaCl solution at 25°C. Table 4.6 lists the corrosion results for the Tafel plots. The E_{corr} values for the coatings matched the OCP values from day 14 of the immersion study. The i_{corr} values decreased, 1.24×10^{-6} to 5.60×10^{-7} A/cm^2, as the concentration of MMT increased in the Cu-Ni matrix. These values are similar to the values

obtained by Varea *et.al.* [26] for the i_{corr} of electrodeposited 70-30 Cu-Ni at $1.8x10^{-6}$ A/cm^2. The polarization resistance (R_p) was also calculated using the Stern-Geary equation:

$$Rp = \frac{\beta_a \ \beta_c}{2.303(\beta_a+\beta_c)} \left(\frac{1}{i_{corr}}\right) \quad (4.2)$$

β_a and β_c are the respective anodic and cathodic Tafel slopes. In Table 4.6, the R_p values of the 70-30 Cu-Ni incorporated with 0.05%, 0.1%, 0.2% MMT were 208.1, 239.7, and 314.3 kΩ•cm^2, respectively, compared to 190.7 kΩ•cm^2 in the case of the pure Cu-Ni film. The addition of MMT into the Cu-Ni matrix helped increase the corrosion resistance.

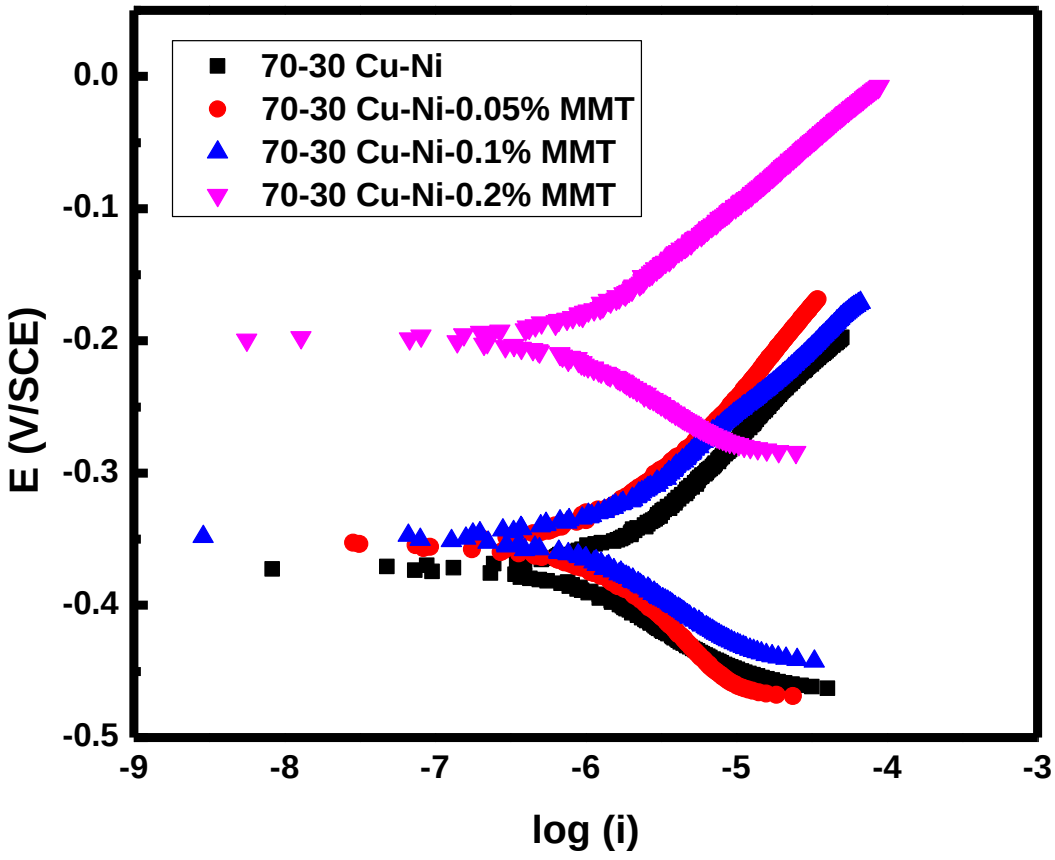

Figure 4.7: Tafel plots for the 70-30 Cu-Ni coatings with and without MMT after being immersed in a 3.5 % NaCl solution for 2 weeks.

Table 4.6: E_{corr}, I_{corr}, and polarization resistance (R_p) of 70-30 Cu-Ni coatings incorporated with and without MMT.

Coatings	E_{corr} (V)	i_{corr} (Acm^{-2})	R_p ($k\Omega \bullet cm^2$)
Cu-Ni	-0.376	1.24×10^{-6}	190.7
Cu-Ni-0.05% MMT	-0.354	8.27×10^{-7}	208.1
Cu-Ni-0.1% MMT	-0.349	7.20×10^{-7}	239.7
Cu-Ni-0.2% MMT	-0.197	5.60×10^{-7}	314.3

Before the active metal dissolution, the anodic part of the polarization curve relates to the creation of $CuCl^-$ adsorbed on the surface of the film. Due to copper dissolution, the current density rises with a rise in the potential by the direct creation of copper (I) chloride (3) or by Cu^+ dissolution to produce CuCl (4-5) [24, 25, 44]:

$$Cu + Cl^- \rightarrow CuCl + e^- \quad (4.3)$$

$$Cu \rightarrow Cu^+ + e^- \quad (4.4)$$

$$Cu^+ + Cl^- \rightarrow CuCl \quad (4.5)$$

The creation of $CuCl_2^-$ is observed at greater concentrations of chloride:

$$CuCl + Cl^- \rightarrow CuCl_2^- \quad (4.6)$$

The corrosion of copper alloys in chloride environments takes place through the cathodic reaction:

$$O_2 + 2H_2O + 4e^- \rightarrow 4OH^- \quad (4.7)$$

and the anodic and chemical reactions seen in equations (3-6) [24, 25, 46]. The transport rate of $CuCl_2^-$ is slowed by an increase in pH close to the surface and begins to favor the creation of Cu_2O at the surface [24, 25, 46]:

$$2CuCl_2^- + 2H_2O \rightarrow Cu_2O + 2H^+ + 4Cl^- \quad (4.8)$$

Hence, the mass transport processes surrounding $CuCl_2^-$ and O_2 going back and forth from the corroding surface controls the corrosion mechanism [24, 25].

A thick inner layer of Cu_2O and an outer layer of $Cu_2(OH)_3Cl$ have been confirmed to be the passivation components in chloride environments for Cu-Ni alloys, where the concentration of

nickel does not exceed 40% [44]. Cu_2O is known to be the main constituent for good corrosion resistance because of its low electronic conductivity. The Cu_2O layer can incorporate different ions, such as nickel and iron because of the presence of vacancies [24, 44, 45]. The nickel products have been observed in the inner oxide layer by x-ray photoelectron spectroscopy [47]. The $Cu_2(OH)_3Cl$ layer forms by precipitation from the dissolution of Cu^{2+} after the formation of the Cu_2O layer [44, 45]. The presence of the layered silicates for this mechanism helps with grain refinement and provides more surface area, thereby slowing the mean free path of corrosion.

4.3.10 Electrochemical Impedance Spectroscopy

The corrosion resistance of Cu-Ni and Cu-Ni-MMT composite coatings were also examined using EIS. Figure 4.8 part A) and part B) are the Bode plots of 70-30 Cu-Ni and different Cu-Ni-MMT composite coatings after immersion in 3.5 % NaCl solution for 14 days at 25 °C. The plots display two maximum phase lags, confirming the presence of two time constants corresponding to the corrosion/passivation processes taking place on the surface. The maximum value phase shift φ_{max} increases with increasing the amount of MMT imbedded into the Cu-Ni matrix which indicates more enhanced stability for the coating layer. The total resistance also increases as a result of embedding of MMT in the metallic matrix which confirms higher passivity of the composite film.

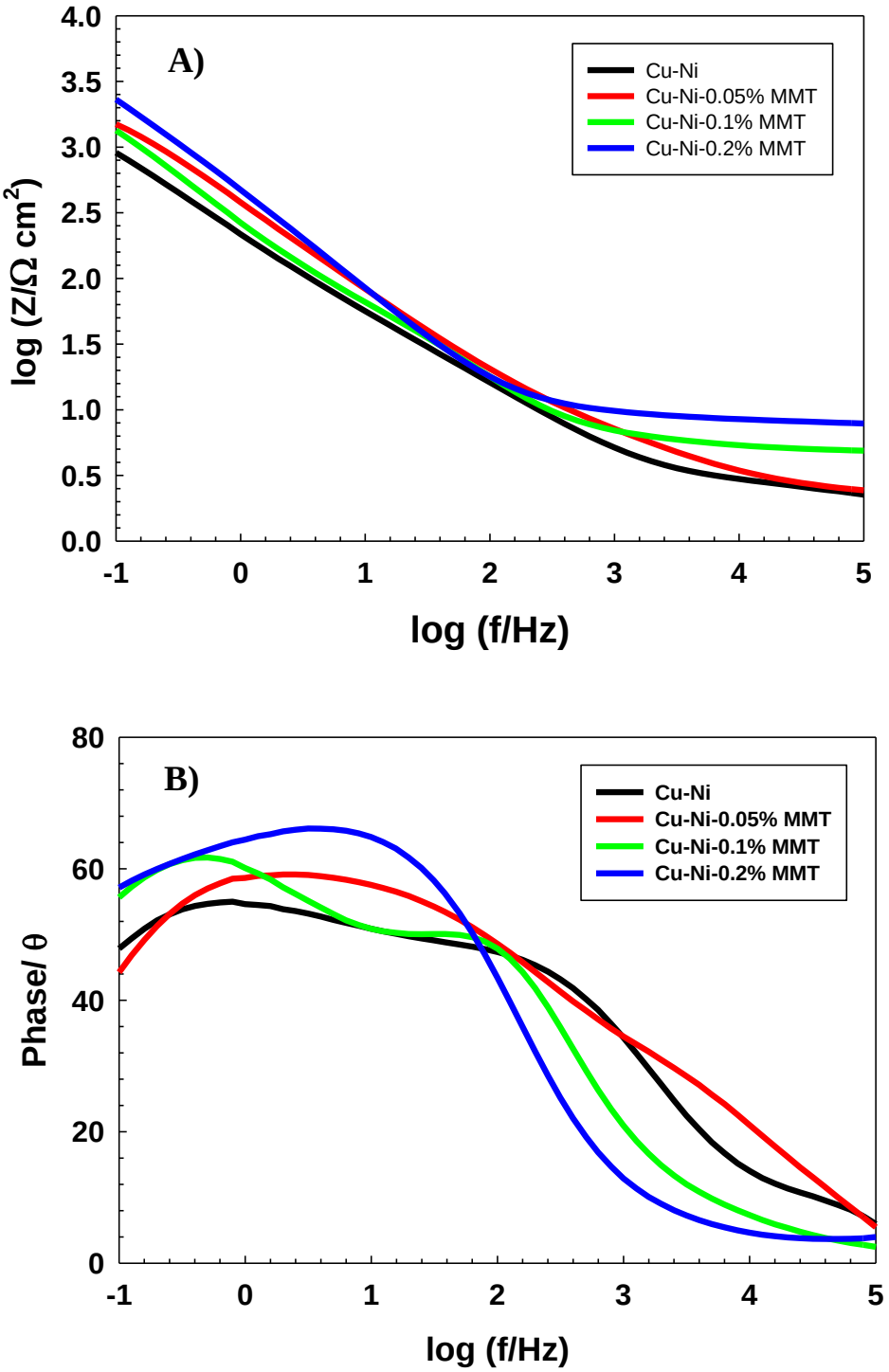

Figure 4.8: A) Bode impedance plot and B) Bode phase plot of pure 70-30 Cu-Ni and different 70-30 Cu-Ni-MMT composite coatings after 2 weeks of immersion in a 3.5 % NaCl solution.

The experimental impedance data were simulated using different models and the best fit was obtained when using the equivalent circuit model shown in the inset for Figure 9. The fitting values showed good agreement between the theoretical and measured values when a frequency dependent constant phase element (Q) was used instead of pure capacitor. The impedance related to the capacitance of this constant phase element is a combination of properties related to the surface and the electro-active species and it can be expressed as:

$$Z_{CPE} = Y_0^{-1}(j\omega)^{-\alpha} \tag{4.9}$$

where Y_0 is the frequency independent real constant of the constant phase element which is identical to the ideal capacitance at ω=1, where ω being the angular frequency (ω=2πf), j=$\sqrt{-1}$ and α is an adjustable empirical exponent, its value ranges from 0 to 1.0 (pure capacitive behavior and perfectly smooth surface) and its value is 0.5 for a porous electrode.

The equivalent circuit model used to fit the measured impedance values consists of two circuits R_1Q_1 and R_2Q_2 parallel combinations and the two circuits are in series with the solution resistance (R_s). Generally, the passive films comprise two layers: a thin barrier layer which is usually compact and crystalline and an outer layer which has usually higher thickness and porous. Accordingly, Q_1 is related to the contribution from outer layer capacitance and Q_2 of the barrier inner layer, whereas R_1 and R_2 are the resistances of the outer and inner layers constituting the passive layer, respectively.

According to this model, the total capacitance of the film can be expressed as:

$$C^{-1} = Q_1^{-1} + Q_2^{-1} \tag{4.10}$$

This circuit has several structures, one of them is the Voight model, where impedance can be expressed as:

$$Z(\omega) = R_s + \frac{R_1}{1+R_1Q_1(j\omega)^{\alpha_1}} + \frac{R_2}{1+R_2Q_2(j\omega)^{\alpha_2}} \text{ where } 0 \leq \alpha_1, \alpha_2 \leq 1 \tag{4.11}$$

Nyquist plots of pure Cu-Ni and Cu-Ni-0.2% MMT composite coatings after 14 days immersion in 3.5 % NaCl at 25°C are represented in Figure 4.9. The diameter of the depressed uncompleted semi circles is larger in case of Cu-Ni-MMT compared to pure Cu-Ni, which indicates increased stability of the passive film in the case of Cu-Ni-MMT compared to that of pure Cu-Ni. The equivalent circuit parameters of the fitting procedure are presented in Table 4.7. The calculated parameters show higher resistance for the inner layer in case of Cu-Ni-MMT composite coating compared to that of pure Cu-Ni, this resistance increases as the MMT content in the metallic matrix increases which is consistent with the data obtained from potentiodynamic polarization, and also confirms that embedding of layered silicate particles into Cu-Ni metallic matrix increases its corrosion resistance.

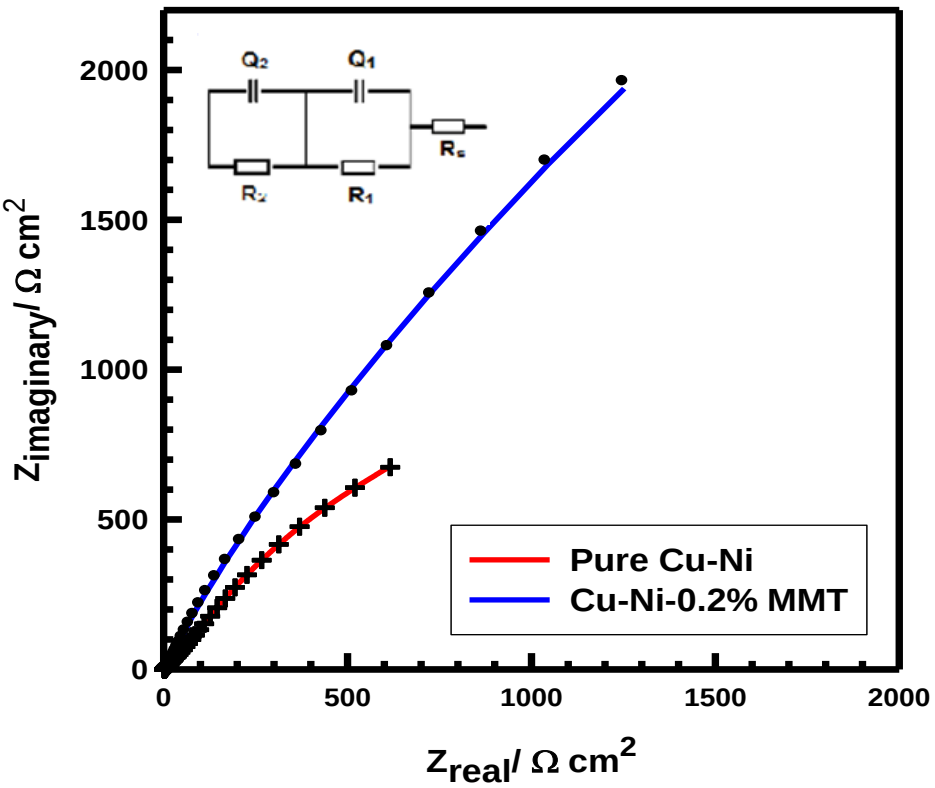

Figure 4.9: Nyquist impedance plots of pure 70-30 Cu-Ni and 70-30 Cu-Ni-0.2 % MMT after being immersed in a 3.5 % NaCl solution for 2 weeks and the equivalent circuit (inset) representing the electrode/electrolyte interface for the electrodeposited layer in the saline solution.

Table 4.7: The equivalent circuit parameters of pure 70-30 Cu-Ni and Cu-Ni-MMT composite coatings after 2 weeks immersion in 3.5 % NaCl solution.

Coatings	R_s (Ω cm^2)	R_1 (Ω cm^2)	Q_1 (Ω^{-1} s^{α} cm^{-2})	α_1	R_2 ($k\Omega$ cm^2)	Q_2 (Ω^{-1} s^{α} cm^{-2})	α_2
Cu-Ni	2.25	49.78	$2.95x10^{-3}$	0.56	2.87	$1336x10^{-6}$	0.73
Cu-Ni-0.05% MMT	0.78	5.45	$6.20x10^{-3}$	0.75	3.02	$954x10^{-6}$	0.75
Cu-Ni-0.1% MMT	5.01	54.0	$1.26x10^{-3}$	0.68	4.92	$709x10^{-6}$	0.80
Cu-Ni-0.2% MMT	8.32	95.20	$2.33x10^{-6}$	0.99	13.77	$583x10^{-6}$	0.76

4.4 Conclusions

With successful incorporation of MMT into the Cu-Ni matrix, the corrosion and mechanical properties were improved over the pure Cu-Ni alloy coating, as shown with Tafel analysis, EIS, and mechanical testing. Electrochemical plating bath conditions were found to control the composition of copper and nickel during electrodeposition, as seen in the AAS analysis. Cu-Ni-0.2% MMT proved to have the best corrosion resistance and hardness. These films may prove to be beneficial as corrosion resistant coatings for the marine environment.

4.5 References

[1] W.Z. Friend, Corrosion of nickel and nickel-base alloys. Willey-Interscience, New York, 1980.

[2] Y.Y. Chang and D.Y. Wang, Corrosion behavior of electroless nickel-coated AISI 304 stainless steel enhanced by titanium ion implantation, Surf. Coat. Tech. 200 (2005) 2187-2191.

[3] P.T. Tang, Pulse reversal plating of nickel alloys, Institute of Metal Finishings 85 (2007) 51-56.

[4] J. Tientong, C.R. Thurber, N. D'Souza, A.M.A. Mohamed, and T.D. Golden, Influence of bath composition at acidic pH on electrodeposition of nickel-layered silicate nanocomposites for corrosion protection, Int. J. Electrochem. 2013 (2013) 1-8.

[5] Painting: New Construction and Maintenance, U.S Army Corps of Engineers EM 1110-2-3400, 2-1 1995.

[6] A.J. Bard and L.R. Faulkner, Electrochemical Methods: Fundamentals and Applications, New York, 2000.

[7] R.A. Horch, T.D. Golden, N.A. D' Souza and L. Riester, Electrodeposition of nickel/montmorillonite layered silicate nanocomposite thin films, Chem. Mater. 14 (2002) 3531-3538.

[8] H.A. Conrad, J.R. Corbett and T.D. Golden, Electrochemical deposition of γ-phase zinc-nickel alloys from alkaline solution, J. Electrochem. Soc. 159 (2012) C29-C32.

[9] Y.H. Ahmad, A.M.A. Mohamed, T.D. Golden, and N. D'Souza, Electrodeposition of nanocrystalline Ni-Mo alloys from alkaline glycinate solutions, Int. J. Electrochem. Sci. 9 (2014) 6438-6450.

[10] S.J. Yuan and S.O. Pehkonen, Surface characterization and corrosion behavior of 70/30 Cu–Ni alloy in pristine and sulfide-containing simulated seawater, Corros. Sci. 49 (2007) 1276-1304.

[11] D.E. Rusu, P. Cojocaru, L. Magagnin, C. Gheorghies and G. Carac, Study of Ni-TiO_2 nanocomposite coating prepared by electrochemical deposition, J. Optoelectron Adv. M. 12 (2010) 2419-2422.

[12] R. Sen, S. Das and K. Das, Synthesis and properties of pulse electrodeposited Ni-CeO_2 nanocomposite, Metall. Mater. Trans. A 43A (2012) 3809-3823.

[13] M.R. Vaezi, S.K. Sadrnezhaad and L. Nikzad, Electrodeposition of Ni–SiC nano-composite coatings and evaluation of wear and corrosion resistance and electroplating characteristics, Colloids and Surf. A 315 (2008) 176-182.

[14] L.M. Chang, J.H. Liu and R.J. Zhang, Corrosion behaviour of electrodeposited Ni/Al_2O_3 composite coating covered with a NaCl salt film at 800 °C, Mater. Corros. 62 (2011) 920-925.

[15] Y.H. Ahmad and A.M.A. Mohamed, Electrodeposition of nanostructured nickel-ceramic composite coatings: A review, Int. J. Electrochem. Sci. 9 (2014) 1942-.

[16] L. Sahu and N.A. D'Souza, Interfacial effects in montmorillonite filled polyester thin films, Open Macromolecules J. 6 (2012) 28-32.

[17] E. Ogunsona, S. Ogbomo, M. Nar and N.A. D'Souza, Thermal and mechanical effects in polystyrene-montmorillonite nanocomposite foams, Cell. Polym. 30 (2011) 79-93.

[18] M.C. Richardson, J. Kim, D. Ho, C.R. Snyder, N.A. D'Souza and G.A. Holmes, Organofunctionalized montmorillonite/epoxy nanocomposites: The effect of interlayer cation distribution on mechanical properties, Polym. Composite 32 (2011) 67-78.

[19] Q. Wang, N.A. D'Souza and T.D. Golden, Ceramic montmorillonite nanocomposites by electrochemical synthesis, App. Clay Sci. 42 (2008) 310-317.

[20] A.Q. Wang, N.A. D'Souza and T.D. Golden, Electrosynthesis of nanocrystalline cerium oxide/layered silicate powders, J. Mater. Chem. 16 (2006) 481-488.

[21] J. Tientong, Y.H. Ahmad, M. Nar, N. D'Souza, A.M.A. Mohamed and T.D. Golden, Improved mechanical and corrosion properties of nickel composite coatings by incorporation of layered silicates, Mater. Chem. Phys. 145 (2014) 44-50.

[22] Y.H. Ahmad, J. Tientong, N. D'Souza, T.D. Golden and A.M.A. Mohamed, Salt water corrosion resistance of electrodeposited Ni-layered silicate nanocomposite coatings from Watts' Type Solution, Surf. Coat. Tech. 242 (2014) 170-176.

[23] S. Mohan and N. Rajasekaren, Influence of electrolyte pH on composition, corrosion properties and surface morphology of electrodeposited Cu-Ni alloy, Surf. Eng. 7 (2011) 519-523.

[24] M. Metikos-Hukovic, I. Skugor, Z. Grubac and R. Babic, Complexities of corrosion behaviour of copper–nickel alloys under liquid impingement conditions in saline water, Electrochim. Acta 55 (2010) 3123-3129.

[25] M. Metikos-Hukovic, R. Babic, I. Skugor and Z. Grubac, Copper–nickel alloys modified with thin surface films: Corrosion behaviour in the presence of chloride ions, Corr. Sci. 53 (2011) 347-352.

[26] A. Varea, E. Pellicer, S. Pané, B.J. Nelson, S. Suriñach, M.D. Baró and J. Sort, Mechanical properties and corrosion behavior of nanostructured Cu-rich CuNi electrodeposited films, Int. J. Electrochem. Sci. 7 (2012) 1288-1302.

[27] T.S.N. Baskaran, S. Narayanan and A. Stephen, Pulsed electrodeposition of nanocrystalline Cu–Ni alloy films and evaluation of their characteristic properties, Mater. Letters 60 (2006) 1990-1995.

[28] M. Alper, H. Kockar, M. Safak and M. C. Baykul, Comparison of Ni-Cu alloy films electrodeposited at low and high pH levels, J. Alloys Compd. 453 (2008) 15-19.

[29] E. Pellicer, A. Varea, S. Pane, K.M. Sivaraman, B.J. Nelson, S. Surinach, M.D. Baro and J. Sort, A comparison between fine-grained and nanocrystalline electrodeposited Cu–Ni films. Insights on mechanical and corrosion performance, Surf. Coat. Tech. 205 (2011) 5285-5293.

[30] W. Schleich, Typical failures of CuNi 90/10 seawater tubing systems and how to avoid them, Eurocorr 2004 (2004) 1–10.

[31] B.E.T. Bautista, M.L. Carvalho, A. Seyeux, S. Zanna, P. Cristiani, B. Tribollet, P. Marcus, and I. Frateur, Effect of protein adsorption on the corrosion behavior of 70Cu-30Ni alloy in artificial seawater, Bioelectroch. 97 (2014) 34-42.

[32] R.S. Gonçalves, D.S. Azambuja, A.M.S. Lucho, M.P. Reche, A.M. Schmidt, Electrochemical studies of copper, nickel, and a Cu55/Ni45 alloy in aqueous sodium acetate, Mater. Res. 4 (2001) 97-101.

[33] W.A. Badawy, K.M. Ismail, and A.M. Fathi, The influence of the copper/nickel ratio on the electrochemical behavior of Cu-Ni alloys in acidic sulfate solutions, J. Alloys Compd. 484 (2009) 365-370.

[34] V.A.R. Boyapati and C.K. Kanukula, Corrosion inhibition of Cu-Ni (90/10) alloy in seawater and sulphide-polluted seawater environments by 1, 2, 3-Benzotriazole, ISRN Corros., 2013 (2013) 1-22.

[35] W. Schleich, R. Feser, G. Schmitt, S. Haarmann and K. Schnier, Effect of seawater chlorination on the erosion corrosion behaviour of CuNi 90/10, *Eurocorr*, CDA Publication (2007) 1-14.

[36] K. Al-Muhanna and K. Habib, Marine bio-fouling of different alloys exposed to continuous flowing fresh seawater by electrochemical impedance spectroscopy, J. Saudi Chem. Soc. (2012) 1-6.

[37] T.A. Green, A.E. Russell and S.J. Roy, The development of a stable citrate electrolyte for the electrodeposition of copper-nickel alloys, J. Electrochem. Soc. 145 (1998) 875-881.

[38] S. Rode, C. Henninot, C. Vallières and M. Matlosz, Complexation chemistry in copper plating from citrate baths, J. Electrochem. Soc. 151 (2004), C405-C411.

[39] E.J. Podlaha, C. Bonhôte and D. Landolt, A mathematically model and experimental study of the electrodeposition of Ni-Cu alloys from complexing electrolytes, Electrochim. Acta 39 (1994) 2649-2657.

[40] S. Rode, C. Henninot and M. Matlosz, Complexation chemistry in nickel and copper-nickel alloy plating from citrate baths, J. Electrochem. Soc. 152 (2005) C248-C254.

[41] R.Y. Ying, P.K. Ng, Z. Mao and R.E. White, Electrodeposition of Cu-Ni alloys from citrate solutions on a rotating disk electrode, J. Electrochem. Soc. 135 (1988) 2964-2971.

[42] A. Karimbeigi, A. Zakeri and A. Sadighzadeh, Effect of composition and milling time on the synthesis of nanostructured Ni-Cu alloys by mechanical alloying method, Iran. J. Mater. Sci. Eng. 10 (2013) 27-31.

[43] K. Al-Muhanna and K. Habib, Corrosion behavior of different alloys exposed to continuous flowing seawater by electrochemical impedance spectroscopy (EIS), Desalin. 250 (2010) 404-407.

[44] I. Milosev and M. Metikos-Hukovic, The behaviour of Cu-xNi (x = 10 to 40 wt%) alloys in alkaline solutions containing chloride ions, Electrochim. Acta 42 (1997) 1537-1548.

[45] A.L. Ma, S.L. Jiang, Y.G. Zheng and W. Ke, Corrosion product film formed on the 90/10 copper–nickel tube in natural seawater: Composition/structure and formation mechanism, Corros. Sci. 91 (2015) 245-261.

[46] W.A. Badaway, K.M. Ismail and A.M. Fathi, Effect of Ni content on the corrosion behavior of Cu-Ni alloys in neutral chloride solutions, Electrochim. Acta 50 (2005) 3603-3608.

[47] B.V. Appa Roa, K.C. Kumar and N.Y. Hebalker, X-ray photoelectron spectroscopy depth-profiling analysis of surface films formed on Cu–Ni (90/10) alloy in seawater in the absence and presence of 1,2,3-benzotriazole, Thin Solid Films 556 (2014) 337-344.

CHAPTER 5

IMPROVED CORROSION AND MECHANICAL PROPERTIES OF ELECTRODEPOSITED 90-10 COPPER NICKEL INCORPORATED WITH LAYERED SILICATES

5.1 Introduction

Enhanced metal matrix composite (MMC) coatings that slow the rate of corrosion at a reduced cost have been heavily studied [1-5]. The MMC coatings can be produced by various techniques such as hot pressing [6], stir casting [7], diffusion bonding [8], powder metallurgy [9], and chemical vapor deposition [10]. However, some of the drawbacks to these methods include production at high temperatures or under vacuum, difficulty in controlling the thickness, and cost. As the accessibility of nanoparticles continues to rise, the interest in reduced cost and low temperature electrodeposited MMCs continues to escalate [11].

Electrodeposition has become a prevalent method for producing new materials, especially in the field of MMCs [12]. Electrodeposited alloys and composites are of particular interest because of their unique and often superior properties compared with their metal counterparts. The electrodeposition technique has several advantages over the other processing methods which include low cost, simplicity of operation, versatility, high production rates, industrial applicability, control of film thickness, and few size and shape limitations [11]. The electrodeposition of a composite involves the electrolysis of the plating bath where nano/micron sized particles are dispersed and various quantities of the particles become embedded within the plated metal matrix giving special properties to the resulting composite [13]. Successful incorporation of particles into the metal matrix by electrocodeposition relies on many different parameters, including the composition of the electrolyte, pH, current density, and properties of the particles [14].

Cu-Ni alloys have many different uses including coatings for pipeline in marine environments, condensers, microelectronics, and heat exchangers [15-18]. Electrodeposited Cu-Ni composite coatings remain important today and have a potential to replace environmentally unfriendly chromium and cadmium coatings. For use in marine environments, copper alloys are used to defend against biofouling of materials by inhibiting microbial induced corrosion (MIC) [19]. One of the most commonly used alloys is the Cu-Ni 90/10 (90% Cu and 10% Ni, Alloy 70600) [20]. This alloy shows a good balance of properties and is more economical than other compositions, which makes it the most widely used [20]. Cu-Ni 90/10 has been studied in long term exposure and it was found that the corrosion rate dropped below 2.5 μm/year after the protective oxide layer was fully formed [19]. When the concentration of nickel is below 40%, an outer layer of $Cu_2(OH)_3Cl$ and a dense inner layer of Cu_2O have been shown to be the passivating layers in high chloride environments [21]. Cu_2O is known to be the main constituent for good corrosion resistance because of its low electronic conductivity. Different ions such as nickel and iron can be incorporated into the Cu_2O layer because of the presence of vacancies [21-23]. X-ray photoelectron spectroscopy has been used to detect nickel products in the Cu_2O layer [24]. Once the Cu_2O layer has formed, the $Cu_2(OH)_3Cl$ layer is produced by precipitation from the dissolution of Cu^{2+} ions [21, 23].

The addition of ceramic nanoparticles can enhance the durability and therefore the lifetime of the coating [25-28]. Montmorillonite (MMT), a clay silicate, possess several desired properties including a large surface area, resistance to a wide range of temperatures, pH resistance, and chemical inertness. Once the clay platelets are embedded into the forming alloy coating structure, the overall thermal stability and mechanical strength of the coating increases [29]. Previous work with MMT embedded into a pure nickel matrix lead to enhanced adhesion, hardness, and corrosion

resistance [30-32]. Relatively, few studies exist on the electrodeposition of copper nickel composites into recesses, greater than a hundred microns and none completely characterize the deposition process. In this work, the corrosion resistance and mechanical properties are evaluated for 90-10 Cu-Ni coatings reinforced with MMT.

5.2 Experimental

5.2.1 Materials and Electrodeposition Procedure

MMT, a layered-silicate clay, has the formula (Na, Ca) $(Al_{1.66}\ Mg_{0.33})_3\ (Si_4O_{10})_3\ (OH)_6 \bullet n(H_2O)$ and the individual platelets are ~1-2 μm in length and 1 nm in height [33]. Various amounts of the layered silicate MMT (Southern Clay Products) were embedded into the Cu-Ni matrix during the electrodeposition process. To exfoliate the MMT, the clay was mechanically stirred for 24-48 hours. The electrochemical bath conditions are listed in Table 5.1. Citrate is an extensively used ligand for electrochemical baths containing transition metals and has been successfully complexed for the electrodeposition of Cu-Ni [34-38]. To adjust the pH of the electrochemical bath to 6, a 6.0 M NaOH solution was used. Stainless steel (Grade 430) substrates (area of 1.768 cm^2) were mechanically polished with different grade emery papers followed by a sequence of cleanings (sonication in ethanol/deionized water) to prepare the substrate surface for electrodeposition. The stainless steel substrate was then activated by dipping the electrode in a 5.0 M H_2SO_4 solution for about 3-5 minutes.

Table 5.1: Deposition conditions for the 90-10 Cu-Ni-MMT composite coatings.

Deposition Conditions	
$Ni(NH_4)_2(SO_4)_2 \bullet 6H_2O$	0.24 M
$CuSO_4 \bullet 5H_2O$	0.06 M
$Na_3C_6H_5O_7 \bullet 2H_2O$	0.25 M
MMT	0 - 0.15%
Applied Voltage	-1.0 V
Charge	30 C

Temperature	25°C
pH	6.0

An EG&G Princeton Applied Research Model 273A potentiostat/galvanostat was used for the electrodeposition, cyclic voltammetry (CV), and immersion test. The electrochemical system was made up of a three electrode system. The working, counter and reference electrodes were a stainless steel substrate, coiled chromel wire, and a saturated calomel reference (SCE), respectively. The solution was purged with N_2 for 15 minutes to deaerate the electrochemical bath before deposition. The stainless steel electrodes were coated with a thin seed layer before deposition to obtain good adhesion of the Cu-Ni coatings onto the substrate [34]. A pH 2.5 buffered nickel-citrate electrochemical bath was used to deposit the thin seed layer (1.5 Coulombs), which contained 77.8 g/L $NiSO_4 \bullet 6H_2O$, 35.3 g/L $Na_3C_6H_5O_7 \bullet 6H_2O$, and 34.6 g/L $H_3C_6H_5O_7$ [30]. After electrodeposition, the composite coating was washed and cleaned in deionized water. The adhesion of the coatings was measured on a DeFelsko, PosiTest AT-A (automatic) Pull-Off Adhesion Tester, and all of the coatings were found to be greater than 75 N/mm^2. The film thickness for the coatings was measured using a Veeco Dektak 8 Stylus Profilometer.

5.2.2 Characterization Studies

The zeta potential and particle size of the Cu-Ni plating solutions were measured using a Delsa Nano-C (Beckman-Coulter Instruments) to determine the stability of MMT in the Cu-Ni plating bath. The Cu-Ni solutions were allowed to adjust to 25°C for 90 seconds using a Peltier device in the instrument before data collection. Atomic absorption spectroscopy (AAS) (Perkin Elmer Analyst 300) analysis was performed using the standard addition method to determine the optimal plating bath to obtain a 90-10 Cu-Ni coating. X-ray Diffraction (XRD) (Siemens D-500

Diffractometer) was performed to elucidate the crystal structure and particle size of the Cu-Ni composite coatings. The experiment was performed with a Cu Kα radiation source λ = 0.15406 nm at 35 kV and 24 mA. The scans were obtained from 40-100° 2θ. Scanning Electron Microscopy (SEM) was used to determine the surface morphology of the composite coatings. FEI Quanta 200 field-emission gun environmental scanning electron microscope coupled with energy dispersion spectroscopy (EDS) was used to determine the elemental composition of Cu-Ni and the layered silicate (Al and Si) in the composite coatings.

Hardness was measured using a Buehler microhardness instrument model Micromet 5101 (Mitutoyo Corp., Japan) to determine the effect of MMT on the mechanical properties in the Cu-Ni matrix. The applied load was 10 gf for 20 s. The final value for the hardness of the coatings was the average of 10 measurements. Shear adhesion tests were measured using the XYZTEC instrument paired with a 2 mm wide knife. The knife was placed at 5 µm above the substrate-coating interface and moved 2 mm horizontally at a velocity 150 µm/s without hold time. The force to move as a function of distance was noted. The adhesive strength is the maximum recorded force divided by the area width of the knife X test distance.

Corrosion tests and the open circuit potential (OCP) study of Cu-Ni and Cu-Ni-MMT coatings were conducted in a simulated seawater bath with the composition of Burkhoder's formula B [21] for 30 days. Potentiodynamic polarization and electrochemical impedance spectroscopy (EIS) were performed on a Parstat 4000 (Princeton Applied Research) using Versa Studio software. A three electrode electrochemical cell was used as the corrosion testing system which was comprised of the working electrode films, two counter graphite rods, and a saturated calomel electrode (SCE) as the reference electrode. Potentiodynamic polarization was performed at a ±250 mV potential range and was applied to the cell with a scan rate of 0.1667 mV/s. EIS analyses were

performed in the frequency range from 10^{-2} to 10^{5} Hz with a 10 mV signal applied at OCP. ZView software was used to analyze the EIS results and the equivalent circuit elements were calculated by ZView according to the fitted EIS data. Raman Spectroscopy was performed to determine the corrosion products present at the surface of the composite coatings after being submersed in a simulated seawater for 30 days. An Almega XR Raman spectrometer equipped with Olympus BX51 microscope with a spatial resolution down to 1 μm was used. An excitation source of 780 nm (30% of 40 mW), single transverse mode, and high brightness diode laser was used. The Raman signal was collected over the range of 1200 – 80 cm^{-1} using a 20x microscope objective.

5.3 Results and Discussion

5.3.1 Cyclic Voltammetry

To determine if the MMT has an effect on the reduction potential of the Cu-Ni deposition or the cathodic peak currents (i_{pc}), cyclic voltammetry was performed. Since, MMT is a non-electroactive particle, it does not possess a redox couple for the electrodeposition cycle. The cyclic voltammograms in Figure 5.1 show that no shift was detected in the reduction potential of copper (-0.45 V) or in the i_{pc} with the addition of 0.05 to 0.15% MMT into the plating bath. The reduction potential for nickel was not observed because of the onset of hydrogen evolution. It has been noted that the concentration of copper depends on the value of the applied potential and as the voltage is increased from -1.0 to -1.075 V, the copper concentration begins to decrease leading to the conclusion that the deposition of copper is diffusion controlled and the deposition of nickel is charge-transfer controlled [39]. With the addition of MMT into the electroplating solution, the voltammograms showed that the MMT platelets have no effect on the metal redox potentials, but

the inclusion of the MMT helps to slightly shift the onset of hydrogen evolution to more cathodic potentials.

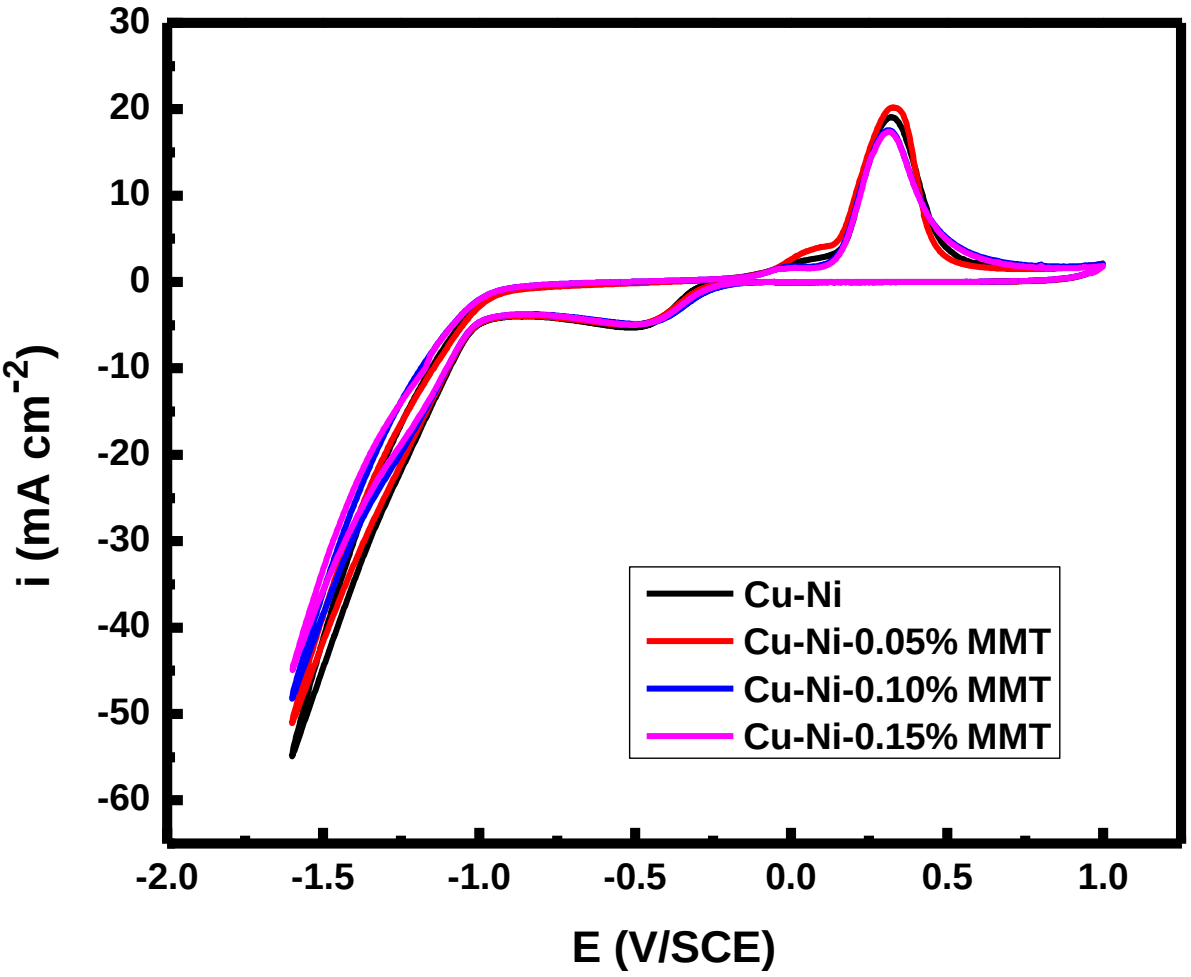

Figure 5.1: Cyclic voltammograms of the 90-10 Cu-Ni films incorporated with and without MMT, run at a scan rate of 50 mV/s.

5.3.2 Particle Size and Zeta Potential

To increase the total interfacial area, exfoliation of the MMT in an aqueous solution needs to occur in order to obtain individual platelets. When exfoliated, the individual platelets measure

approximately 1 nm in thickness and 1-2 μm in length. MMT tends to swell when placed in an aqueous environment and starts to mechanically shear after vigorous stirring for 24-48 hours. The negatively charged platelets become countered by positively charged copper and nickel ions in the plating solution. During the deposition process, the platelets are thought to electrostatically adsorb onto the stainless steel substrate. The long planar shape of the platelet helps to yield a snug contact with the oppositely-charged substrate [33]. The copper and nickel ions are reduced to Cu^0 and Ni^0 for deposition onto the substrate producing a strongly adhering coating.

When dealing with the electrocodeposition of a MMC, understanding the particle stability in the colloidal electroplating bath is crucial because the properties of composites escalate significantly with the preferential embedding of individual particles [7]. The particle size and zeta potential (Table 5.2) of the Cu-Ni plating solutions were analyzed to examine the stability of the dispersion of the MMT platelets into the electroplating bath. In an aqueous solution, the particle sizes of the MMT ranged from 430 to 525 nm. As the MMT is introduced into the plating solution, the particle size significantly increases versus the aqueous solution and continues to rise with increased amounts of MMT added into the plating bath. This change is probably due the adsorption of Cu and Ni ions onto the surface of the negatively charged platelets and platelet agglomeration. The MMT concentration (0.05-0.15%) in an aqueous solution produced zeta potential values of approximately -40 mV, which shows that the exfoliated MMT platelets yield a stable dispersion in an aqueous solution. Typically, an ideal zeta potential for nanoparticle dispersion would be greater than ±25 mV. The Cu-Ni solution incorporated with the MMT platelets produced zeta potential values of approximately -20 mV, which shows to be less stable than the ideal value. Adsorption of Cu and Ni onto the interface of the MMT platelet causes the zeta potential value to move towards a more positive value, which leads to small decrease in the

electrostatic stabilization of the dispersion into the Cu-Ni plating bath. Although, the dispersion of the MMT into the plating solution showed to be slightly unstable, the dispersion was stable long enough for deposition purposes without having to be mechanically stirred for re-stabilization.

Table 5.2: Particle Size and Zeta Potential for MMT in aqueous solution and the 90-10 Cu-Ni-MMT Plating Solutions.

Solutions	Particle Size (nm) (n=3)	Zeta Potential (mV) (n=3)
0.05% MMT	430 ± 20	-39.6 ± 0.4
0.10% MMT	495 ± 15	-39.9 ± 0.3
0.15% MMT	525 ± 20	-39.1 ± 0.5
Cu-Ni-0.05% MMT	2710 ± 90	-20.1 ± 0.5
Cu-Ni-0.10% MMT	3030 ± 70	-19.7 ± 0.4
Cu-Ni-0.15% MMT	3280 ± 80	-19.4 ± 0.4

5.3.3 Film Thickness

The film thickness of the pure 90-10 Cu-Ni and Cu-Ni-MMT coatings were measured to determine if the MMT affected the coating thickness, which can be seen in Table 5.3. All of the coatings were electrochemically deposited until 30 coulombs of charge was obtained. The MMT seemed to have no effect on the current efficiency of the electrodeposition process as the thickness of the coatings did not reduce with incorporation of MMT. However, the coatings did seem to get slightly thicker as the MMT percentage increased, which is probably due to the incorporation of the MMT into the metal matrix and a slight increase in surface roughness.

Table 5.3: Film thickness of the 90-10 coatings incorporated with an without MMT deposited to 30 coulombs of charge.

Coatings	Film Thickness (μm) (n=3)
Cu-Ni	6.12 ± 0.04
Cu-Ni – 0.05% MMT	6.17 ± 0.03
Cu-Ni – 0.10% MMT	6.20 ± 0.05
Cu-Ni – 0.15% MMT	6.24 ± 0.07

5.3.4 X-ray Diffraction and Scanning Electron Microscopy

The x-ray diffraction (XRD) scans for the Cu-Ni alloy and Cu-Ni-MMT composite coatings shown in Figure 5.2 were performed to analyze the crystal structure and the particle size. All of the XRD patterns show typical fcc peaks corresponding to the (111) crystallographic plane of Cu-Ni, as seen in Figure 5.2(A-D). Note that the peaks corresponding to the reinforced MMT particles are not seen in the XRD patterns even at low 2θ angles from the composite coatings due to complete exfoliation and low reinforcement content.

For the Cu-Ni alloy, only one peak is observed for each reflection because the Cu-Ni alloy is known as an isomorphous binary alloy, which means the two metals are completely soluble in one another and have one type of crystal structure (fcc) with little to no strain [40]. The (111) major peak at 43.51° is shifted between the values of pure copper at 43.297° (PDF # 00-004-0836) and pure nickel at 44.508° (PDF # 00-004-0850). The (111) peak starts to broaden with the addition of MMT, as seen in Figure 5.2(B-D), which indicated that there was a decrease in the particle size of the composite coatings. The particle size (L) for each film was calculated using the Scherrer equation:

$$B_r = k\lambda/L \cos \theta \quad (1)$$

The Gaussian peak fit method of $B_r^2 = B_o^2 - B_i^2$ was used to calculate the peaks, where B_o is the peak broadening of the coating and the B_i is the instrumental broadening calculated using a silicon standard. The proportionality constant k was assumed to be 1, $\lambda = 0.15406$ nm from the Cu Kα radiation, and θ is the position of the (111) peak. The calculated particle sizes presented in Table 5.4, showed that the particle size continued to decrease as the amount of MMT increased in the coatings.

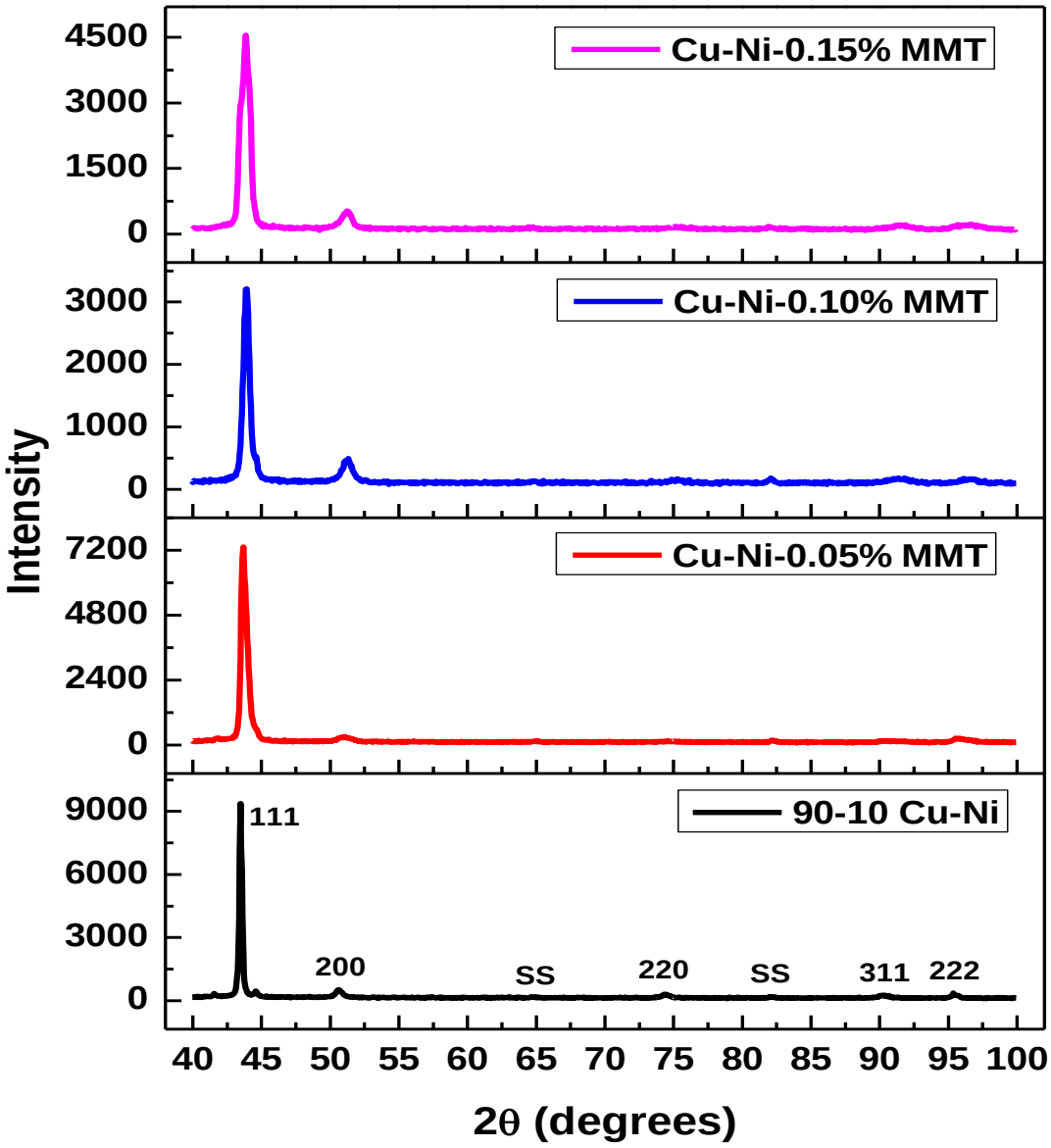

Figure 5.2: X-ray diffraction patterns of 90-10 Cu-Ni and Cu-Ni-MMT run from 40-100° 2θ at a step size of 0.05° and dwell time of 1 sec. (ss – stainless steel substrate)

Table 5.4: Particle Sizes of the 70-30 Cu-Ni Coatings incorporated with and without MMT calculated from the Scherrer Equation using X-ray Diffraction.

Coatings	Particle Size (nm) (n=3)
Cu-Ni	58 ± 5
Cu-Ni – 0.05% MMT	19 ± 3
Cu-Ni – 0.10% MMT	16 ± 4
Cu-Ni – 0.15% MMT	12 ± 3

The surface morphologies of the pure Cu-Ni alloy and Cu-Ni-MMT composite coatings are shown in Figure 5.3. The SEM micrographs display less defined grain boundaries with the incorporation of MMT into the Cu-Ni coating. With the incorporation of the MMT into the Cu-Ni matrix, the particle sizes also decrease, grain refinement takes place, and the grain boundaries reduce, which helps lead to an increase in corrosion resistance, hardness, and shear resistance of the coatings, as seen in the next sections.

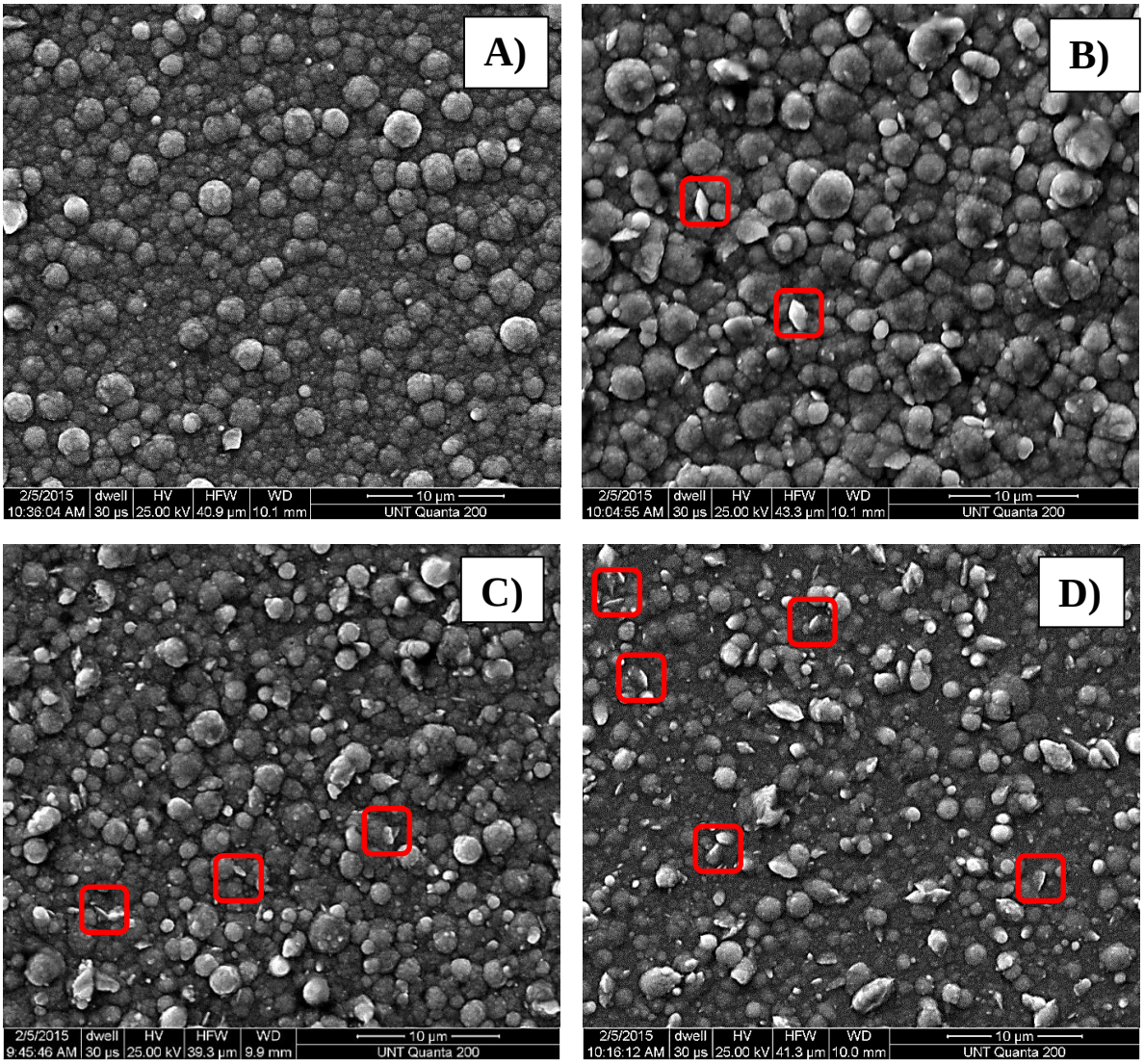

Figure 5.3: SEM micrographs of: A) 90-10 Cu-Ni, B) 90-10 Cu-Ni-0.05 % MMT, C) 70-30 Cu-Ni-0.1 % MMT, and D) 90-10 Cu-Ni-0.15 % MMT. Red Squares denote MMT platelets.

5.3.5 Atomic Absorption Spectroscopy and Energy Dispersion Spectroscopy

Atomic absorption spectroscopy (AAS) was performed to determine the composition of the Cu-Ni coatings. The atomic absorption analysis showed that the composition of 90-10 Cu-Ni was maintained during the electrodeposition process at values of copper (88 ± 1%) and nickel (12 ± 1%). EDS was also performed to evaluate the Cu, Ni, Si, and Al composition of the coatings with Si and Al being measured because they are major elemental components in the MMT. The EDS results presented in Table 5.5 showed that as the amount of MMT increased in the plating solution, the Si and Al content increased, which confirmed the presence of MMT in the coatings. Also, the Cu-Ni ratio started to slightly change to higher concentrations of Ni with the incorporation of MMT into the Cu-Ni matrix, which indicated that MMT had a minor influence on the deposition of the Cu-Ni ratio. Previous data has shown that Ni ions adhere significantly to the surface of the MMT platelet [33]. Nickel is in excess in the solution because of the deposition conditions and most of the copper is complexed with citrate [36]. At pH values greater than 5, the heterobinuclear deprotonated species, $CuNiCit_2H_2^{4-}$ appears replacing the binary deprotonated species, $Cu_2Cit_2H_2^{4-}$. With Cu present in the plating solution, less citrate is available to complex with the nickel, resulting in a lower concentration of the species containing 1 nickel and 2 citrate ($NiCit_2H^{3-}$ and $NiCit_2^{4-}$) and an increase in $Nicit^{-}$species [36]. The slight change in the Cu-Ni ratio of the coatings can be attributed to the embedding of the MMT particles with large amount of Ni adhered to the surface of the platelets.

Table 5.5: Energy Dispersive Spectroscopy of the 90-10 Cu-Ni Coatings incorporated with MMT showing the main elements of MMT (Si and Al) present in the composite coatings.

Coatings	Copper (%)	Nickel (%)	Silicon (%)	Aluminum (%)
Cu-Ni	89.65	10.35	---	---
Cu-Ni – 0.05% MMT	86.05	11.50	1.49	0.96
Cu-Ni – 0.10% MMT	84.90	11.32	2.35	1.43
Cu-Ni – 0.15% MMT	83.97	11.21	2.94	1.88

5.3.6 Hardness and Shear Strength

There are two factors that play a major role in the hardness of the MMC coating; the amount of particles embedded into the matrix and the microstructure of the metallic matrix. The microstructure of the metallic matrix is controlled by the parameters of the electrodeposition process including bath concentration of metallic ion, pH, applied current and the current density [41]. The amount of the particles embedded into the matrix are in direct relation to the bath concentration, size of particles, solution pH and type of reinforcement material [9]. MMT has shown the ability to increase the hardness substantially in a pure nickel matrix [31]. The effect of embedding MMT platelets into the Cu-Ni matrix on the microhardness was analyzed and the results can be seen in Figure 5.4. The microhardness of the Cu-Ni coatings increase by 17% with the incorporation of MMT into the Cu-Ni matrix. Since all the coatings have a nanocrystalline Cu-Ni matrix, the increasing hardness of the Cu-Ni-MMT composite coatings with increasing MMT content seems to primarily be due to the enhanced dispersion strengthening effects. In addition, the presence of the finer grains helps to impede the dislocation motion resulting in an increase in the microhardness [42]. Therefore, the increase in hardness for the Cu-Ni-MMT coatings can also be attributed to grain refining which is related to the nucleation of small grains on the surface of the incorporated particles, which leads to an overall structural refinement also seen in the XRD data.

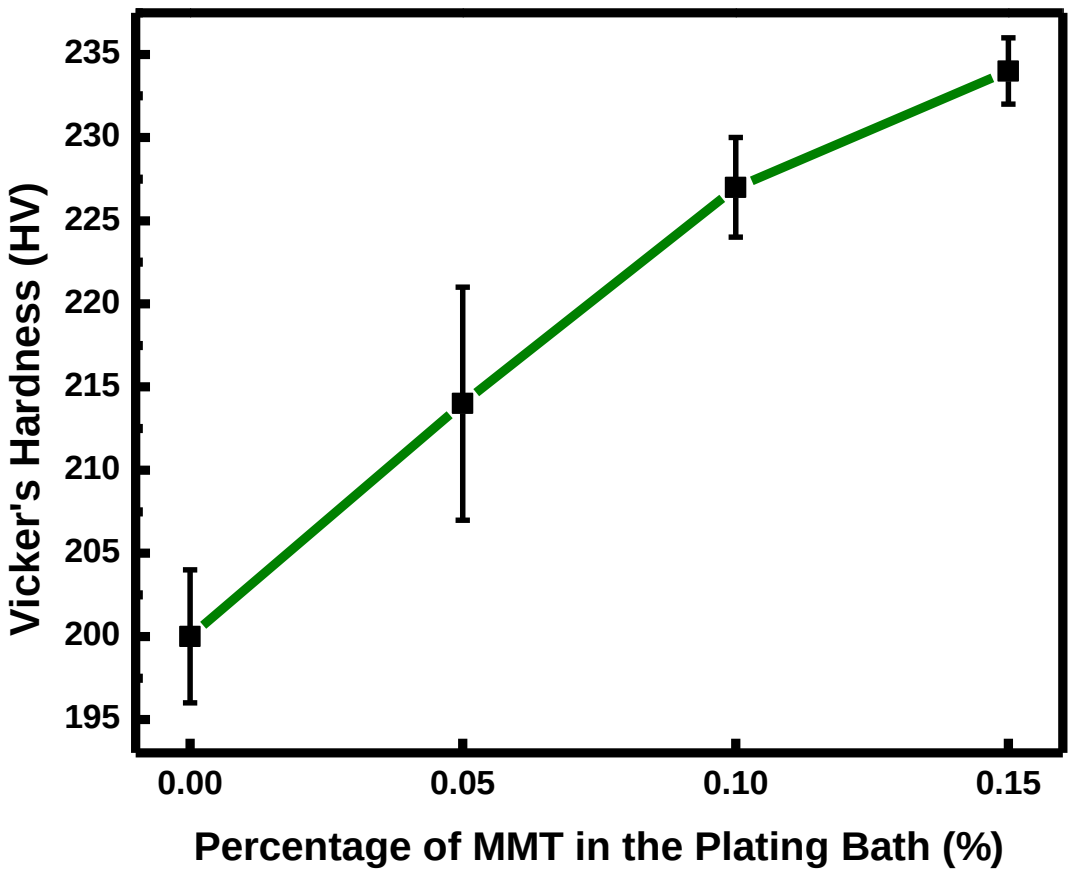

Figure 5.4: The microhardness of the 90-10 Cu-Ni composite coatings versus the percentage of MMT in the plating solution.

The adhesion strength for the coatings are shown in Figure 5.5. The adhesion strength of all the nanocomposite coatings exceeds that of the Cu-Ni matrix alone. The presence of the platelets provides enhanced resistance to the knife movement. An 85% increase was observed for the 0.10% MMT. The shear adhesion strength began to decrease beyond 0.10% MMT because with an increased amount of platelets in the coating more substrate-platelet contact occurs and decreases the effective area of the matrix-substrate contact.

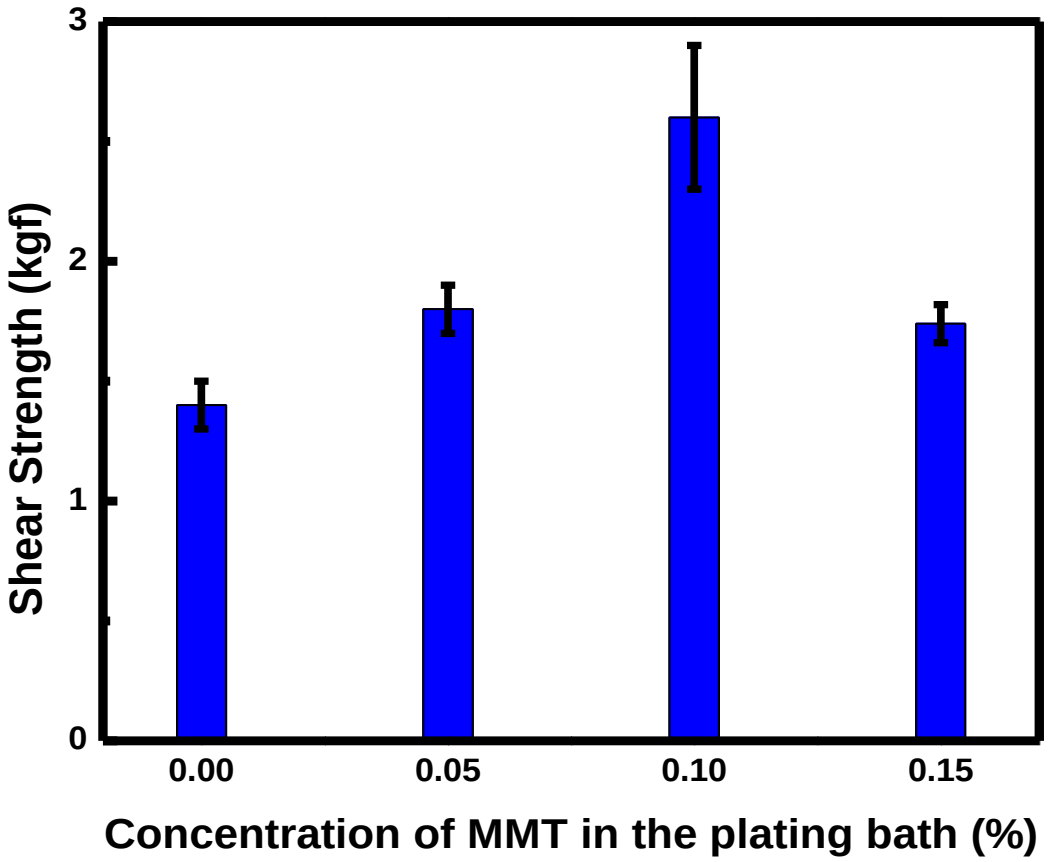

Figure 5.5: The shear adhesion strength of the 90-10 Cu-Ni with different percentages of MMT in the plating solution.

5.3.7 Immersion Study

An immersion test of open circuit potential (OCP) vs. time was performed to evaluate the coating stability of the Cu-Ni incorporated with and without MMT particles. Figure 5.6 shows that, the OCP of the pure Cu-Ni, Cu-Ni-0.05% MMT, and Cu-Ni-0.1% MMT films were shifted cathodically after three, eight and seventeen days, respectively. The OCP of Cu-Ni-0.15% MMT stayed stable over the extended period of 30 days. Al-Muhanna *et.al.* [43] also observed a cathodic shift in OCP for Cu-Ni in the first 10-15 days of their study leading to lower corrosion resistance.

This can be related to the amount of time it takes to form the protective oxide layers. Colin *et.al.* [44] observed that the temperature of the seawater plays a predominant role in the corrosion rate, where the protective oxide layer formed rapidly as the seawater temperature increased thus causing a subsequent decrease in the corrosion rate. Figure 5.7 shows the appearance of the immersed films with time. It is observed that the Cu-Ni-0.15% MMT underwent the least amount of change over the 30 day period, which follows the stability seen for this coating in the OCP vs. time graph. Eventually, this coating's OCP value also shifted cathodically after 38 days, which indicates the same Cu_2O protective layer formation. This result shows that MMT provides a barrier protection for the Cu-Ni matrix, which stabilizes and increases the corrosion resistance.

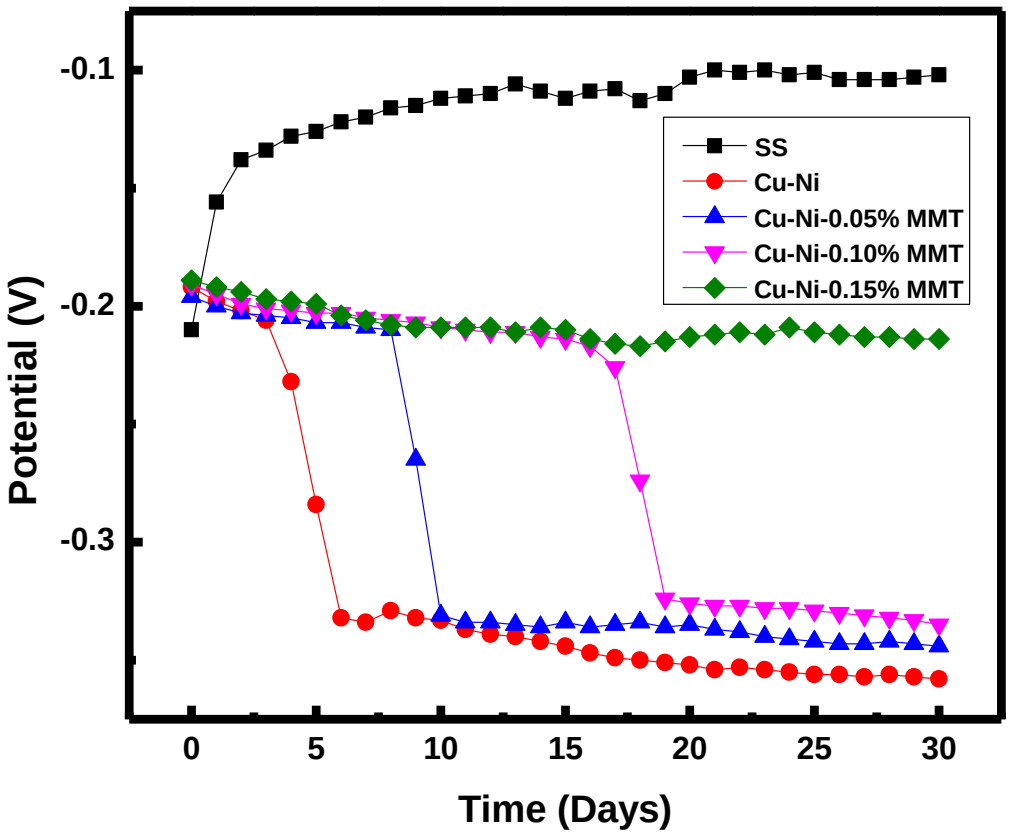

Figure 5.6: Plot of the immersion test for the 90-10 Cu-Ni coatings with and without MMT measured by OCP vs. time for 30 days in Burkhoder's Formula B solution.

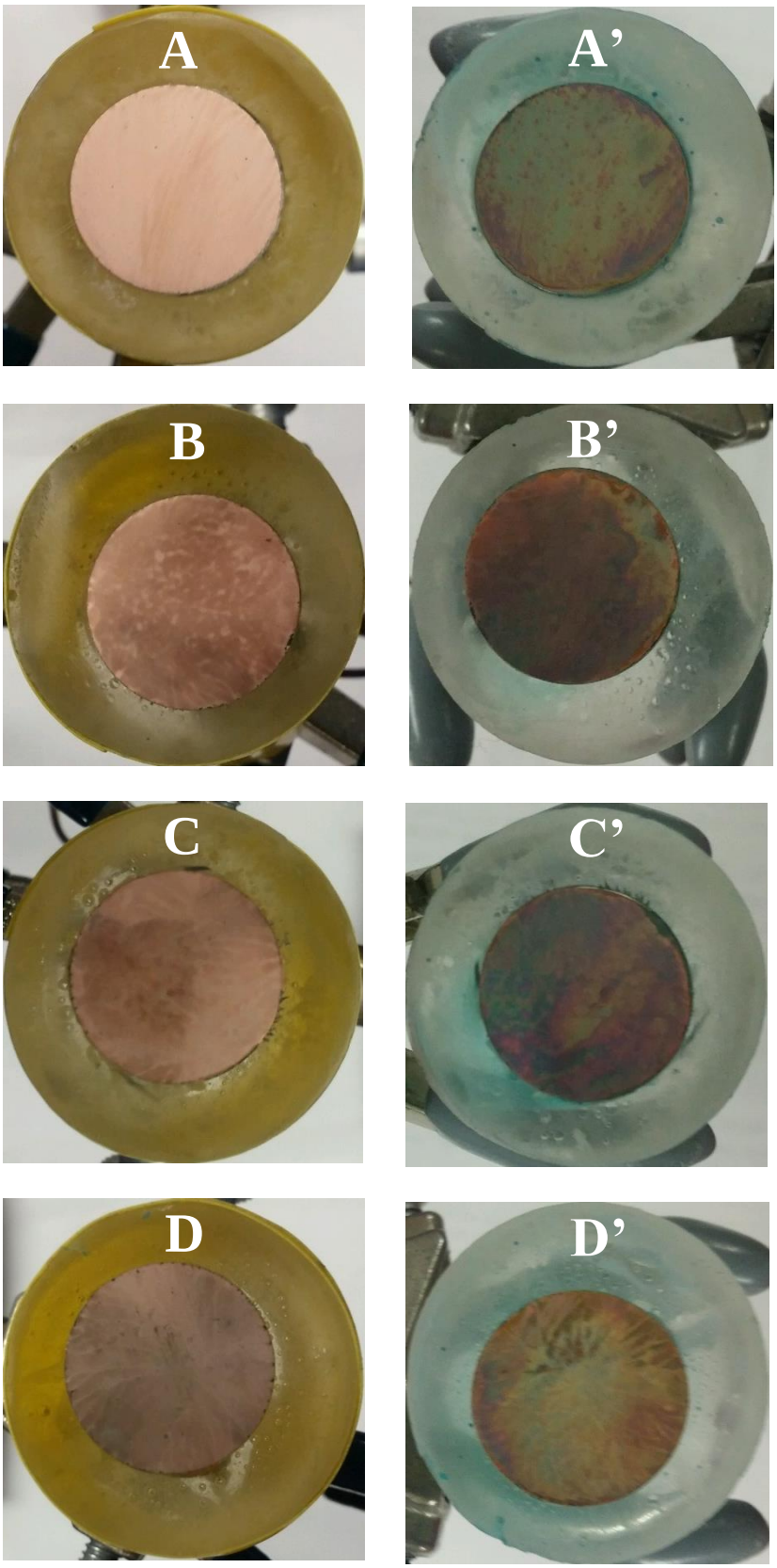

Figure 5.7: Pictures of before and after soaking the 90-10 Cu-Ni and Cu-Ni-MMT coatings in Burkhoder's Formula B for 30 days. A-A' is before-after of pure Cu-Ni, B-B' is before-after of Cu-Ni-0.05% MMT, C-C' is before-after of Cu-Ni-0.10% MMT, and D-D' is before-after of Cu-Ni-0.15% MMT.

5.3.8 Tafel Analysis

The corrosion resistance of Cu-Ni and Cu-Ni-MMT composite coatings were evaluated using potentiodynamic polarization with Tafel analysis, as seen in Figure 5.8. The corrosion values were measured after immersing the prepared coatings for 30 days in Burkhoder's Formula B simulated seawater at 25°C. Table 5.6 lists the corrosion results for the Tafel analysis. The E_{corr} value for the Cu-Ni-0.15% MMT is more anodic than the other coatings which was evident in the immersion study because of the increased stability provided by the MMT platelets in the Cu-Ni matrix. With an increase of concentration of MMT into the Cu-Ni coatings, the i_{corr} values decreased from 2.50×10^{-6} to 9.84×10^{-7} A/cm^2. Varea *et.al.* [38] also observed a similar i_{corr} value for electroplated 90-10 Cu-Ni at 1.8×10^{-6} A/cm^2. The i_{corr} value was calculated using the Stern-Geary equation:

$$i_{corr} = \frac{\beta_a \ \beta_c}{2.303 R_p(\beta_a + \beta_c)} \tag{2}$$

where β_a and β_c are the respective anodic and cathodic Tafel slopes. The R_p, polarization resistance of the coating, values shown in Table 5.6 were calculated by taking the slope of a linear polarization scan from ±20 mV at 0.1667 mV/s. The R_p value of the pure Cu-Ni coating was 11.77 kΩ•cm^2, whereas the Cu-Ni incorporated with MMT increased to 33.28 kΩ•cm^2 with 0.15% MMT. The addition of MMT into the Cu-Ni deposition process onto the stainless steel substrate significantly increased the resistance to corrosion by providing barrier protection to slow the mean free path of corrosion.

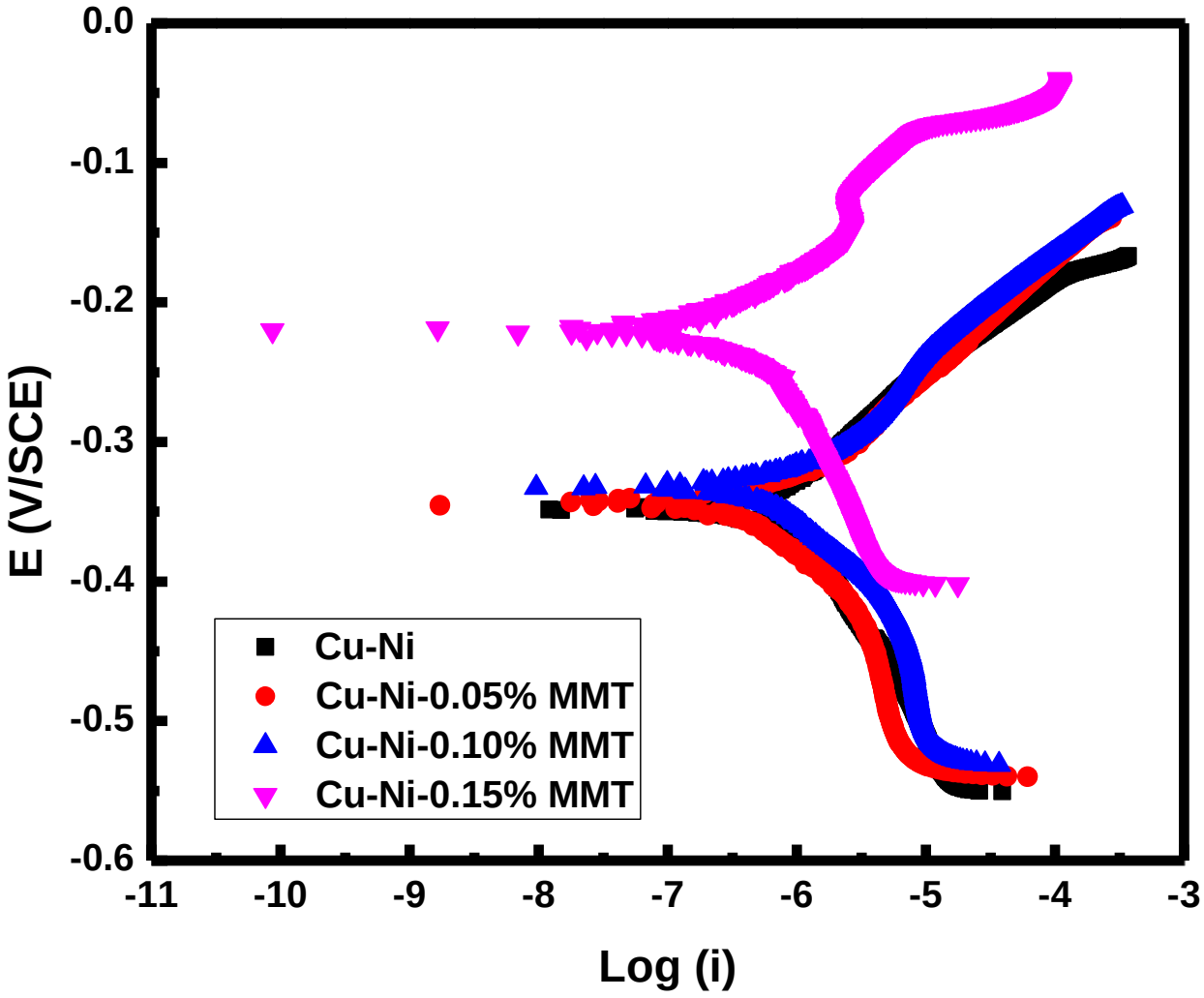

Figure 5.8: Tafel plots for the 90-10 Cu-Ni coatings with and without MMT after being immersed in Burkhoder's Formula B solution for 30 days.

Table 5.6: E_{corr}, I_{corr}, and polarization resistance (R_p) of 90-10 Cu-Ni Coatings incorporated with and without MMT.

Coatings	E_{corr} (V)	i_{corr} (Acm^{-2})	R_p ($k\Omega \bullet cm^2$)
Cu-Ni	-0.349	2.50×10^{-6}	11.77
Cu-Ni-0.05% MMT	-0.347	1.66×10^{-6}	15.50
Cu-Ni-0.10% MMT	-0.336	1.56×10^{-6}	17.10
Cu-Ni-0.15% MMT	-0.220	9.84×10^{-7}	33.28

5.3.9 Electrochemical Impedance Spectroscopy

The EIS results were modeled using the ZView software to give more information about the corrosion behavior of the Cu-Ni composite coatings in a simulated seawater environment. An equivalent electrical circuit was used to model the interaction between the coatings and simulated seawater (Burkhoder's Formula B), which is seen in Figure 5.9 (inset). In the equivalent electrical circuit, R_s displays resistance of the simulated seawater solution. R_{ct} equals the charge transfer resistance, related to resistance of the coating surface. R_p represents the resistance of the coating. The constant phase element (C_{pe1}) represents the coating capacitance, capacitance of the outer porous layer. C_{pe2} represents the double layer capacitance, determines the interface between the simulated seawater and sample.

The Nyquist plots of the Cu-Ni and Cu-Ni-MMT composite coatings after 30 days immersion in Burkhoder's Formula B at 25°C are shown in Figure 5.9. The capacitive loop diameter, which corresponds to a larger corrosion resistance, is larger in case of Cu-Ni-MMT composite coatings compared to the pure Cu-Ni coating, due to the stability of the passive composite coatings. The calculated circuit elements from the ZView software are shown in Table 5.7. The calculated parameters reveal a higher R_p value for the Cu-Ni-MMT composite coating compared to the pure Cu-Ni coating. This resistance escalates as the MMT content in the Cu-Ni matrix rises which is consistent with the data obtained from potentiodynamic polarization.

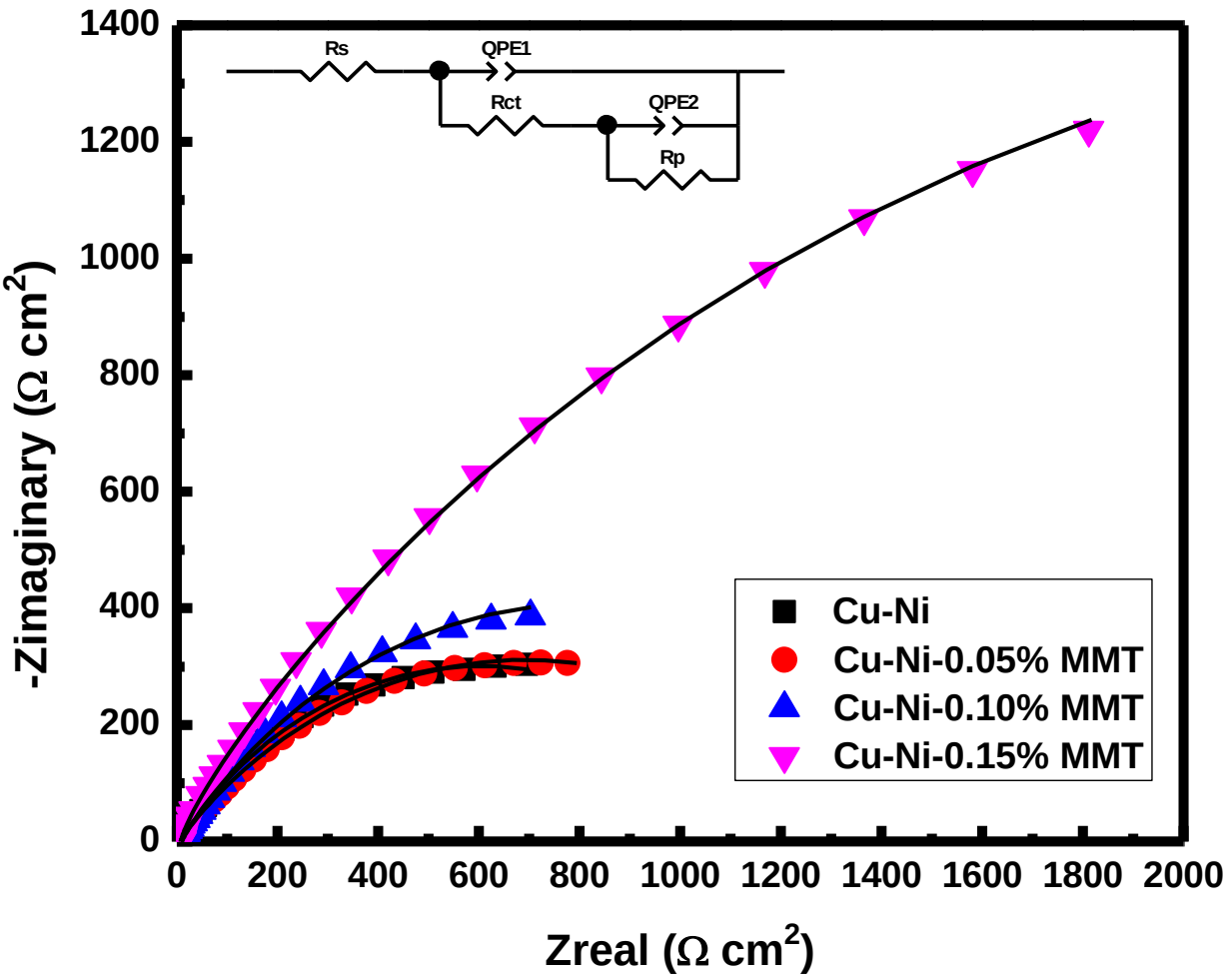

Figure 5.9: Nyquist impedance plots of the 90-10 Cu-Ni coatings with and without MMT after being immersed in Burkhoder's Formula B solution for 30 days and the equivalent circuit (inset) representing the electrode/electrolyte interface for the electrodeposited layer in the saline solution.

Table 5.7: The equivalent circuit parameters of pure 90-10 Cu-Ni and Cu-Ni-MMT composite coatings after 30 days immersion in a simulated seawater solution.

Coatings	R_s (Ω cm^2)	R_{ct} (Ω cm^2)	Q_{PE1} (Ω^{-1} s$^{\alpha}$ cm^{-2})	α_1	R_P (kΩ cm^2)	Q_{PE2} (Ω^{-1} s$^{\alpha}$ cm^{-2})	α_2
Cu-Ni	9.857	2.53	4.81×10^{-6}	0.53	1.21	1.14×10^{-5}	0.92
Cu-Ni-0.05% MMT	7.495	4.89	1.41×10^{-6}	0.57	1.38	6.16×10^{-6}	0.98
Cu-Ni-0.10% MMT	7.189	1.57	8.85×10^{-6}	0.58	1.62	8.30×10^{-6}	0.97
Cu-Ni-0.15% MMT	7.109	1.04	4.40×10^{-7}	0.59	6.08	1.48×10^{-5}	0.92

The incorporation of the exfoliated MMT played a major role in improving the corrosion resistance of Cu-Ni coating by two mechanisms. First, the MMT particles act as inert physical barriers to the initiation and development of defect corrosion, modifying the microstructure of the Cu-Ni film and hence improving the corrosion resistance of the coating. Second, the dispersion of MMT into the Cu-Ni matrix results in the formation of many corrosion microcells in which the MMT acts as cathode and the Cu-Ni matrix acts as anode. Such corrosion microcells facilitated the anode polarization. Therefore, in the presence of MMT, localized corrosion is inhibited, and mainly homogeneous corrosion occurs.

5.3.10 Raman Spectroscopy

To identify the corrosion products for the Cu-Ni and Cu-Ni-MMT coatings, Raman spectroscopy from 1200 – 80 cm^{-1} was performed on the surface of the coatings. Figure 5.10 shows the Raman spectra of the pure Cu-Ni and Cu-Ni-0.15% MMT coatings. The presence of $Cu_2(OH)_3Cl$ (peaks at 133 cm^{-1}, 357 cm^{-1} and 591 cm^{-1} [23, 45]), Cu_2O (peaks at 154 cm^{-1} and 407 cm^{-1} [23, 46]), and CuCl (peaks at 206 cm^{-1} and 1085 cm^{-1}) were observed in the spectra. In addition to the copper complexes, the presence of γ-FeOOH (peak at 260 cm^{-1} [23, 47, 48]), α-FeOOH (peak at 480 cm^{-1}), and NiO (peaks at 533 cm^{-1} and 705 cm^{-1} [49]) were also identified. In conclusion, the spectra for the two coatings were identical showing that the corrosion products are unchanged with the addition of MMT into the Cu-Ni matrix. Also, this result shows that the enhancement in the corrosion protection is due to the grain refinement and barrier protection of the MMT versus a change in the corrosion products.

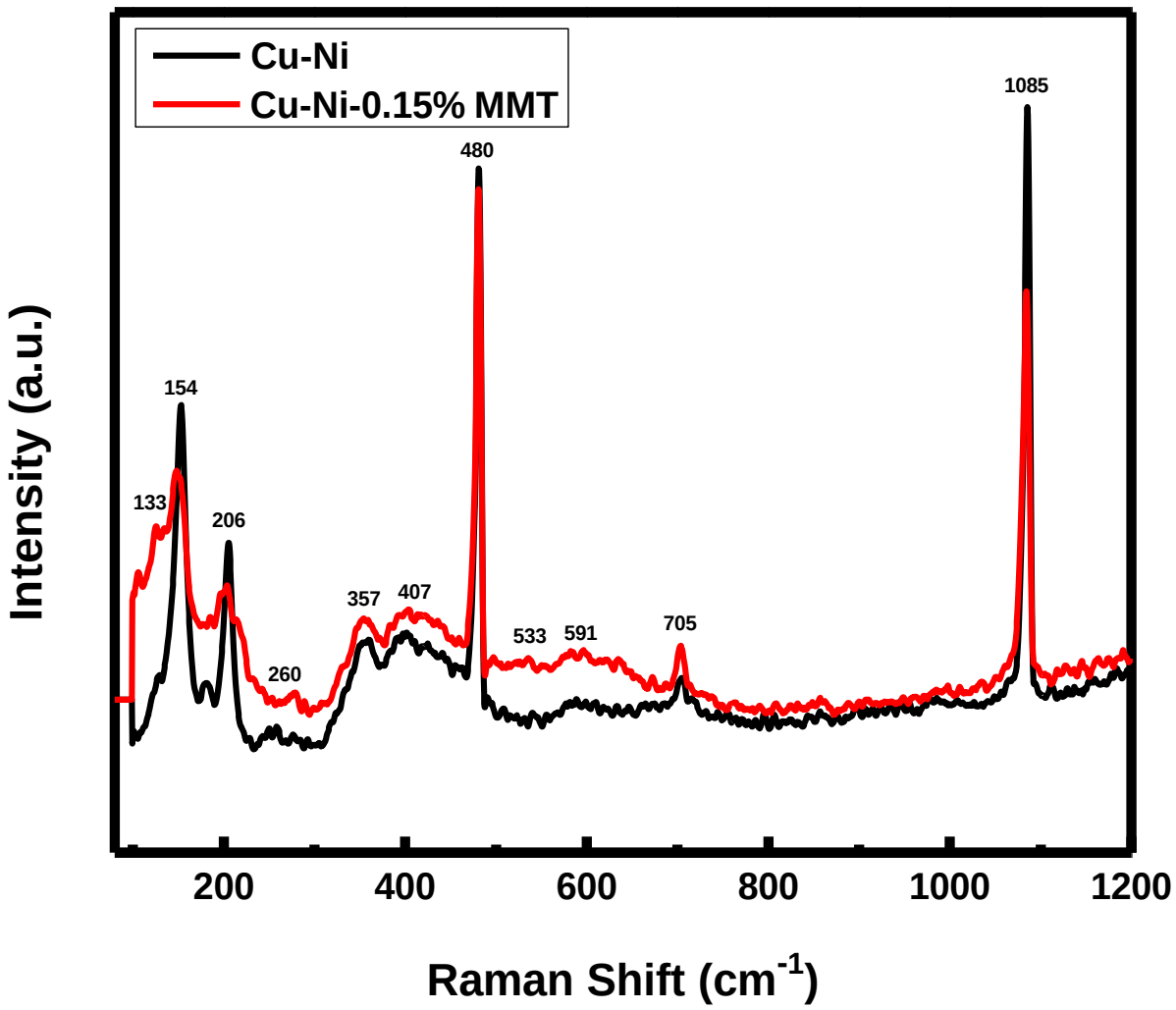

Figure 5.10: Raman Spectra of the 90-10 Cu-Ni and Cu-Ni-0.15% MMT coatings after being immersed in Burkhoder's Formula B solution for 30 days.

5.4 Conclusions

The composition of the Cu-Ni coating was controlled by the bath conditions and the applied voltage to produce a 90-10 ratio. Incorporation of the exfoliated MMT into the Cu-Ni matrix by electrodeposition helped the grain refinement and barrier protection, which improved both the corrosion resistance and mechanical properties. The 0.15% MMT addition produced the best

increase in the hardness and the corrosion resistance, whereas the 0.10% MMT addition provided the best shear adhesion strength. Also, the 0.15% MMT condition helped to stabilize the corrosion potential during the 30 day immersion study in simulated seawater.

5.5 References

[1] M.R. Vaezi, S.K. Sadrnezhaad and L. Nikzad, Electrodeposition of Ni–SiC nano-composite coatings and evaluation of wear and corrosion resistance and electroplating characteristics, Colloids and Surf. A 315 (2008) 176-182.

[2] L.M. Chang, J.H. Liu and R.J. Zhang, Corrosion behaviour of electrodeposited Ni/Al_2O_3 composite coating covered with a NaCl salt film at 800 °C, Mater. Corros. 62 (2011) 920-925.

[3] I. Zamblau, S. Varvara and L.M. Muresan, Corrosion behavior of Cu–SiO_2 nanocomposite coatings obtained by electrodeposition in the presence of cetyl trimethyl ammonium bromide, J. Mater. Sci. 46 (2011) 6484–6490.

[4] S. Ramalingam, V. S. Muralidharan and A. Subramania, Electrodeposition and characterization of Cu-TiO_2 nanocomposite coatings, J. Solid State Electrochem. 13 (2009) 1777–1783.

[5] F. C. Walsh and C. Ponce de Leon, A review of the electrodeposition of metal matrix composite coatings by inclusion of particles in a metal layer: an established and diversifying technology, Trans. Inst. Met. Finish. 92 (2) (2014) 83-98.

[6] V. K. Lindroos and M. J. Talvitie, Recent advances in metal matrix composites, J. Mater. Process. Tech. 53 (1995) 273-284.

[7] J. Hashim, L. Looney and M.S.J. Hashmi, Metal matrix composites: production by the stir casting method, J. Mater. Process. Tech. 92-93 (1999) 1-7.

[8] M. Muratoglu, O. Yilmaz and M. Aksoy, Investigation on diffusion bonding characteristics of aluminum metal matrix composites (Al/SiCp) with pure aluminum for different heat treatments, J. Mater. Process. Tech.178 (2006) 211–217.

[9] M.J. Tan and X. Zhang, Powder metal matrix composites: selection and processing, Mater. Sci. Eng. A244 (1998) 80–85.

[10] N. Popovskaa, H. Gerhard, D. Wurm, S. Poscher, G. Emig, and R. F. Singer, Chemical vapor deposition of titanium nitride on carbon fibres as a protective layer in metal matrix composites, Mater. Design 18 (4/6) (1997) 239-242.

[11] A. Gomes, I. Pereira, B. Fernández, and R. Pereiro, Electrodeposition of metal matrix nanocomposites: Improvement of the chemical characterization techniques, Advances in Nanocomposites - Synthesis, Characterization and Industrial Applications 21 (2011) 503-526.

[12] A.J. Bard, L.R. Faulkner. Electrochemical Methods: Fundamentals and Applications, New York, 2000.

[13] M. Musiani, Electrodeposition of composites: an expanding subject in electrochemical materials science, Electrochim. Acta 45 (2000) 3397–3402.

[14] C.T.J. Low, R.G.A. Wills and F.C. Walsh, Electrodeposition of composite coatings containing nanoparticles in a metal deposit, Surf. Coat. Tech. 201 (2006) 371–383.

[15] S.J. Yuan and S.O. Pehkonen, Surface characterization and corrosion behavior of 70/30 Cu–Ni alloy in pristine and sulfide-containing simulated seawater, Corr. Sci. 49 (2007) 1276-1304.

[16] B.E.T. Bautista, M.L. Carvalho, A. Seyeux, S. Zanna, P. Cristiani, B. Tribollet, P. Marcus, and I. Frateur, Effect of protein adsorption on the corrosion behavior of 70Cu-30Ni alloy in artificial seawater, Bioelectroch. 97 (2014) 34-42.

[17] T.S.N. Baskaran, S. Narayanan and A. Stephen, Pulsed electrodeposition of nanocrystalline Cu–Ni alloy films and evaluation of their characteristic properties, Mater. Letters 60 (2006) 1990-1995.

[18] X. Zhu and T. Lei, Characteristics and formation of corrosion product films of 70Cu-30Ni alloy in seawater, Corr. Sci. 44 (2002) 67-79.

[19] W. Schleich, Typical failures of CuNi 90/10 seawater tubing systems and how to avoid them, Eurocorr 2004 (2004) 1–10.

[20] W. Schleich, R. Feser, G. Schmitt, S. Haarmann and K. Schnier, Effect of seawater chlorination on the erosion corrosion behaviour of CuNi 90/10, Eurocorr, CDA Publication (2007) 1-14.

[21] I. Milosev and M. Metikos-Hukovic, The behaviour of Cu-xNi (x = 10 to 40 wt%) alloys in alkaline solutions containing chloride ions, Electrochim. Acta 42 (1997) 1537-1548.

[22] M. Metikos-Hukovic, I. Skugor, Z. Grubac and R. Babic, Complexities of corrosion behaviour of copper–nickel alloys under liquid impingement conditions in saline water, Electrochim. Acta 55 (2010) 3123-3129.

[23] A.L. Ma, S.L. Jiang, Y.G. Zheng and W. Ke, Corrosion product film formed on the 90/10 copper–nickel tube in natural seawater: Composition/structure and formation mechanism, Corros. Sci. 91 (2015) 245-261.

[24] B.V. Appa Roa, K.C. Kumar and N.Y. Hebalker, X-ray photoelectron spectroscopy depth-profiling analysis of surface films formed on Cu–Ni (90/10) alloy in seawater in the absence and presence of 1,2,3-benzotriazole, Thin Solid Films 556 (2014) 337-344.

[25] A.K. Pradhan and S. Das, Pulse-reverse electrodeposition of Cu–SiC nanocomposite coating: Effect of concentration of SiC in the electrolyte, J. Alloy Compd. 590 (2014) 294–302.

[26] Y. Gan, D. Lee, X. Chen and J.W. Kysar, Structure and properties of electrocodeposited Cu–Al_2O_3 nanocomposite thin films, J. Mater. Process. Tech. 127 (2005) 451-456.

[27] R. Sen, S. Das and K. Das, Synthesis and properties of pulse electrodeposited Ni-CeO_2 nanocomposite, Metall. Mater. Trans. A 43A (2012) 3809-3823.

[28] D.E. Rusu, P. Cojocaru, L. Magagnin, C. Gheorghies and G. Carac, Study of Ni-TiO_2 nanocomposite coating prepared by electrochemical deposition, J. Optoelectron Adv. M. 12 (2010) 2419-2422.

[29] Q. Wang, N.A. D'Souza and T.D. Golden, Ceramic montmorillonite nanocomposites by electrochemical synthesis, App. Clay Sci. 42 (2008) 310-317.

[30] J. Tientong, C.R. Thurber, N. D'Souza, A.M.A. Mohamed, and T.D. Golden, Influence of bath composition at acidic pH on electrodeposition of nickel-layered silicate nanocomposites for corrosion protection, Int. J. Electrochem. 2013 (2013) 1-8.

[31] J. Tientong, Y.H. Ahmad, M. Nar, N. D'Souza, A.M.A. Mohamed and T.D. Golden, Improved mechanical and corrosion properties of nickel composite coatings by incorporation of layered silicates, Mater. Chem. Phys. 145 (2014) 44-50.

[32] Y.H. Ahmad, J. Tientong, N. D'Souza, T.D. Golden and A.M.A. Mohamed, Salt water corrosion resistance of electrodeposited Ni-layered silicate nanocomposite coatings from Watts' Type Solution, Surf. Coat. Tech. 242 (2014) 170-176.

[33] R.A. Horch, T.D. Golden, N.A. D' Souza and L. Riester, Electrodeposition of nickel/montmorillonite layered silicate nanocomposite thin films, Chem. Mater. 14 (2002) 3531-3538.

[34] T.A. Green, A.E. Russell and S.J. Roy, The development of a stable citrate electrolyte for the electrodeposition of copper-nickel alloys, J. Electrochem. Soc. 145 (1998) 875-881.

[35] S. Rode, C. Henninot, C. Vallières and M. Matlosz, Complexation chemistry in copper plating from citrate baths, J. Electrochem. Soc. 151 (2004), C405-C411.

[36] E.J. Podlaha, C. Bonhôte and D. Landolt, A mathematically model and experimental study of the electrodeposition of Ni-Cu alloys from complexing electrolytes, Electrochim. Acta 39 (1994) 2649-2657.

[37] S. Rode, C. Henninot and M. Matlosz, Complexation chemistry in nickel and copper-nickel alloy plating from citrate baths, J. Electrochem. Soc. 152 (2005) C248-C254.

[38] R.Y. Ying, P.K. Ng, Z. Mao and R.E. White, Electrodeposition of Cu-Ni alloys from citrate solutions on a rotating disk electrode, J. Electrochem. Soc. 135 (1988) 2964-2971.

[39] A. Varea, E. Pellicer, S. Pané, B.J. Nelson, S. Suriñach, M.D. Baró and J. Sort, Mechanical properties and corrosion behavior of nanostructured Cu-rich CuNi electrodeposited films, Int. J. Electrochem. Sci. 7 (2012) 1288-1302.

[40] M. Alper, H. Kockar, M. Safak and M. C. Baykul, Comparison of Ni-Cu alloy films electrodeposited at low and high pH levels, J. Alloys Compd. 453 (2008) 15-19.

[41] E.B. Budevski, G.T. Staikov, W.J. Lorenz, Electrochemical Phase Formation and Growth, An Introduction to the Initial Stages of Metal Deposition, Wiley-VCH, Weinheim, 1996.

[42] H. Gül, F. Kılı, S. Aslan, A. Alp, H. Akbulut, Characteristics of electro-co-deposited Ni–Al_2O_3 nano-particle reinforced metal matrix composite (MMC) coatings,Wear 267 (2009) 976-990.

[43] K. Al-Muhanna and K. Habib, Corrosion behavior of different alloys exposed to continuous flowing seawater by electrochemical impedance spectroscopy (EIS), Desalin. 250 (2010) 404-407.

[44] S. Colin, E. Beche, R. Berjoan, H. Jolibois, and A. Chambaudet, An XPS and AES study of the free corrosion of Cu-, Ni-, and Zn-based alloys in synthetic sweat, Corr. Sci. 41 (1999) 1051-1065.

[45] R.L. Frost, Raman spectroscopy of selected copper minerals of significance in corrosion, Spectrochim. Acta Part A 59 (2003) 1195-1204.

[46] J.C. Hamilton, J.C. Farmer, R.J. Anderson, Insitu Raman-spectroscopy of anodic films formed on copper and silver in sodium-hydroxide solution, J. Electrochem. Soc. 133 (1986) 739-745.

[47] D.L.A. de Faria, S. Venâncio Silva, M.T. de Oliveira, Raman microspectroscopy of some iron oxides and oxyhydroxides, J. Raman Spectrosc. 28 (1997) 873-878.

[48] M.K. Nieuwoudt, J.D. Comins, I. Cukrowski, The growth of the passive film on iron in 0.05 M NaOH studied in situ by Raman micro-spectroscopy and electrochemical polarisation. Part I: near-resonance enhancement of the Raman spectra of iron oxide and oxyhydroxide compounds, J. Raman Spectrosc. 42 (2011) 1335-1339.

[49] J.H. Kim, I.S. Hwang, Development of an in situ Raman spectroscopic system for surface oxide films on metals and alloys in high temperature water, Nucl. Eng. Des. 235 (2005) 1029 1040.

CHAPTER 6

A NOVEL FLOW CELL DESIGN FOR ELECTRODEPOSITION OF METAL MATRIX COMPOSITE COATINGS

6.1 Introduction

Metal matrix composite (MMC) coatings have become of great interest recently because of improvements in corrosion resistance and mechanical properties [1-5]. Electrodeposition has become more favorable in synthesizing coatings because of low cost, convenience, and the ability to work at low temperatures [6]. Previous research has focused on the physical properties of layered silicates [7] and on the incorporation of non-electroactive inorganics such as silicas [8], aluminas [9], and cerias [10] into metal matrices to produce corrosion resistant films. These inorganic additives have diverse structures, including platelets and spheres, with proportions in the nanometer range. Platelet type particles, such as the layered silicate montmorillonite (MMT), display many different beneficial properties including a large surface area, extreme temperature resistance, resistance to a change in pH, and chemical inertness. MMT platelets benefit over its spherical counterparts because of its larger surface area, which sets up a more arduous mean free path to corrosion. Nickel was chosen as the metal matrix because of its high abundance in nature and its natural high resistance to corrosion. [11, 12].

Previous studies have also determined that MMT platelets can increase corrosion resistance as well as mechanical properties such as hardness when incorporated into the nickel matrix [13-15]. However, the smectite clays used are isotropic in nature, which means the platelets are oriented in all directions [16]. This presents problems in depositions, given that this isotropic nature is transferred to the composite coatings as well. This results in the clay platelets being deposited at random angles, limiting the enhancement of the corrosion resistance and introducing

gaps in the barrier protection that allow for an easier mean free path to corrosion (Figure 6.1A). If the platelets particles can be forced into a horizontal layer-by-layer arrangement rather than a random orientation, then the resulting films will increasingly demonstrate the beneficial properties of the arranged platelets (Figure 6.1B) [17]. Using neutron diffraction data, Ramsay et al. [16] discovered that clay platelets can orient under shear conditions. Under low shear force conditions, the platelets were shown to align in a direction parallel to the force, known as anisotropy, and retain their orientation even after flowing had ceased [16].

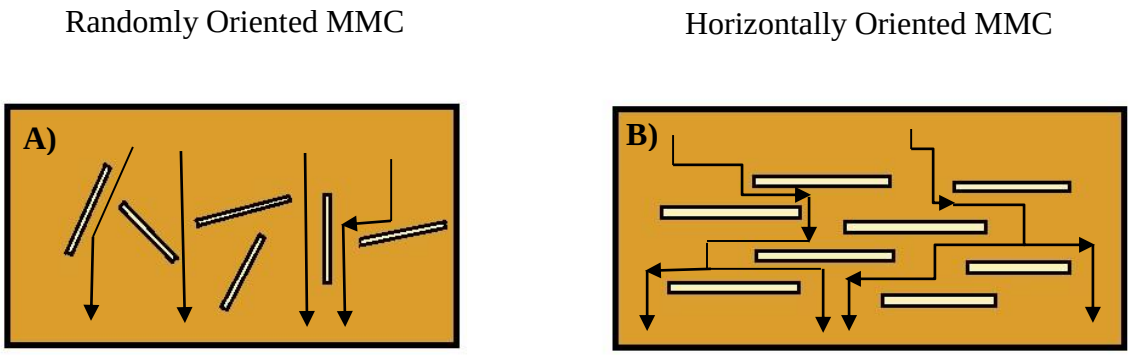

Figure 6.1: Diagram of A) a randomly oriented MMC and B) a horizontally oriented MMC showing the mean free path of corrosion.

There are several factors that affect the quality of electrocodepositing metal matrix composites including the composition of the bath, the plating parameters, and the geometry of the electrodes in the bath [18]. Different cell geometry designs have been proposed to generate enhanced composite coatings through the embedding of spherical particles [19, 20]. Also, electrochemical flow cells have also been studied to determine the effects of flowing the plating solution on the quality of the composite coating [19, 21]. Lee et al. [21] noted that the speed of the flow greatly affected incorporation of spherical particles into the metal matrix and with the higher velocities the particles would be carried away from the electrode leading to lower

concentrations of the particles in the composite coating. However no studies have been conducted examining how flow can affect a metal matrix composite coating incorporating platelet type particles. This study investigates whether anisotropy alignment can be transferred to electrodeposition solutions through the use of a novel flow cell design, resulting in oriented platelets being embedded into the metal matrix to create enhanced properties.

6.2 Materials and Methods

6.2.1 Flow Cell Design and Analysis

The flow cell used for this study consisted of a 3-D printed polylactic acid (PLA) plastic section, connected by 1/4 inch diameter Tygon tubing to a Fisher Scientific FH100 peristaltic pump with an adjustable flow rate. A Makerbot Replicator 2 was used for 3-D printing. As the electrolyte is pumped through the cell, it passes first through an inflow valve and then into a flow separator; at this point, the solution separates into 6 slots that then exit into the main chamber, where deposition takes place (Figure 6.2). The flow separator is used to ensure a consistent flow across the entirety of the working electrode, rather than just across the center of the electrode. The electrolyte then exits via the outflow valve located on the far end of the working electrode, and cycles back through the tubing to repeat the process.

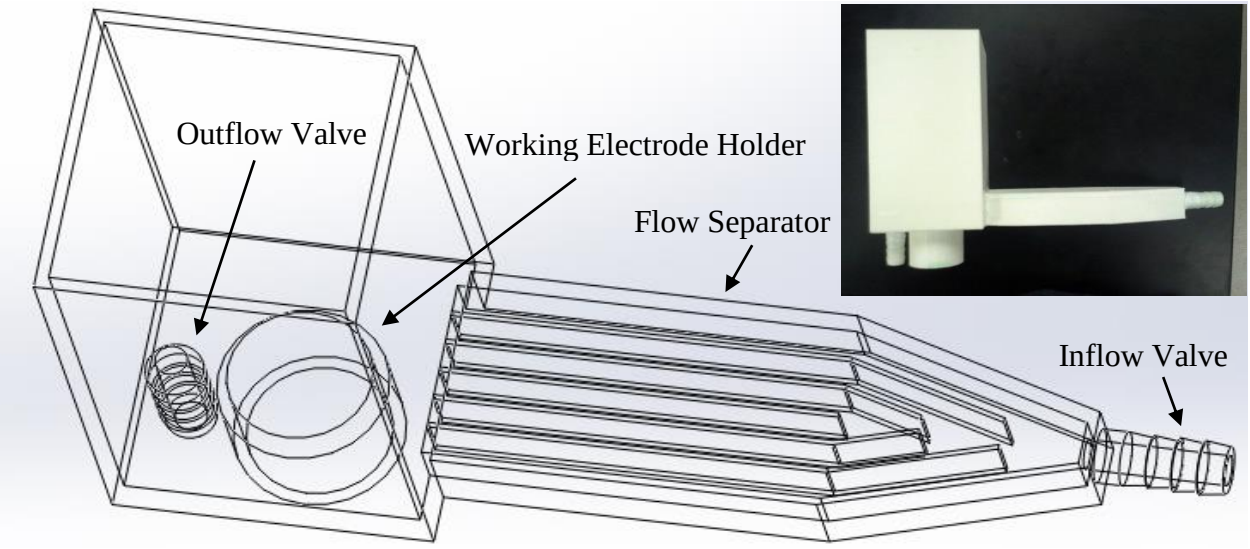

Figure 6.2: Diagrams of the flow cell designed for the deposition of nickel-layered silicates. Flow of the electrolyte starts at the right end of the diagrams at the inflow valve.

The CAD software, SolidWorks, was used for the design and modeling of the fluid flow of the electrochemical flow cell. The fluid simulation feature in the SolidWorks software independently analyzes flow patterns, modeling the path of fluids using the Navier-Stokes equation, a relationship of velocity (m/s) (v) to the fluid pressure (Pa) (p), fluid density (kg/m^3) (ρ), viscosity (Pa·s) (μ), and gravity and other body forces (N/m^3) (f) within fluids:

$$\rho\left(\frac{\partial v}{\partial t} + v \cdot \nabla v\right) = -\nabla \mathrm{p} + \mu\Delta^2 v + \mathrm{f} \tag{6.1}$$

The analysis showed that under laminar flow conditions, the flow would spread evenly over the surface of the electrode, as shown in Figure 6.3A. While the platelets need shear to orient, high velocities also increase the likelihood of turbulent flow (Figure 6.3B). Specifically, high velocities (and corresponding high flow rates) increase the Reynolds Number, a dimensionless quantity used to predict flow patterns.

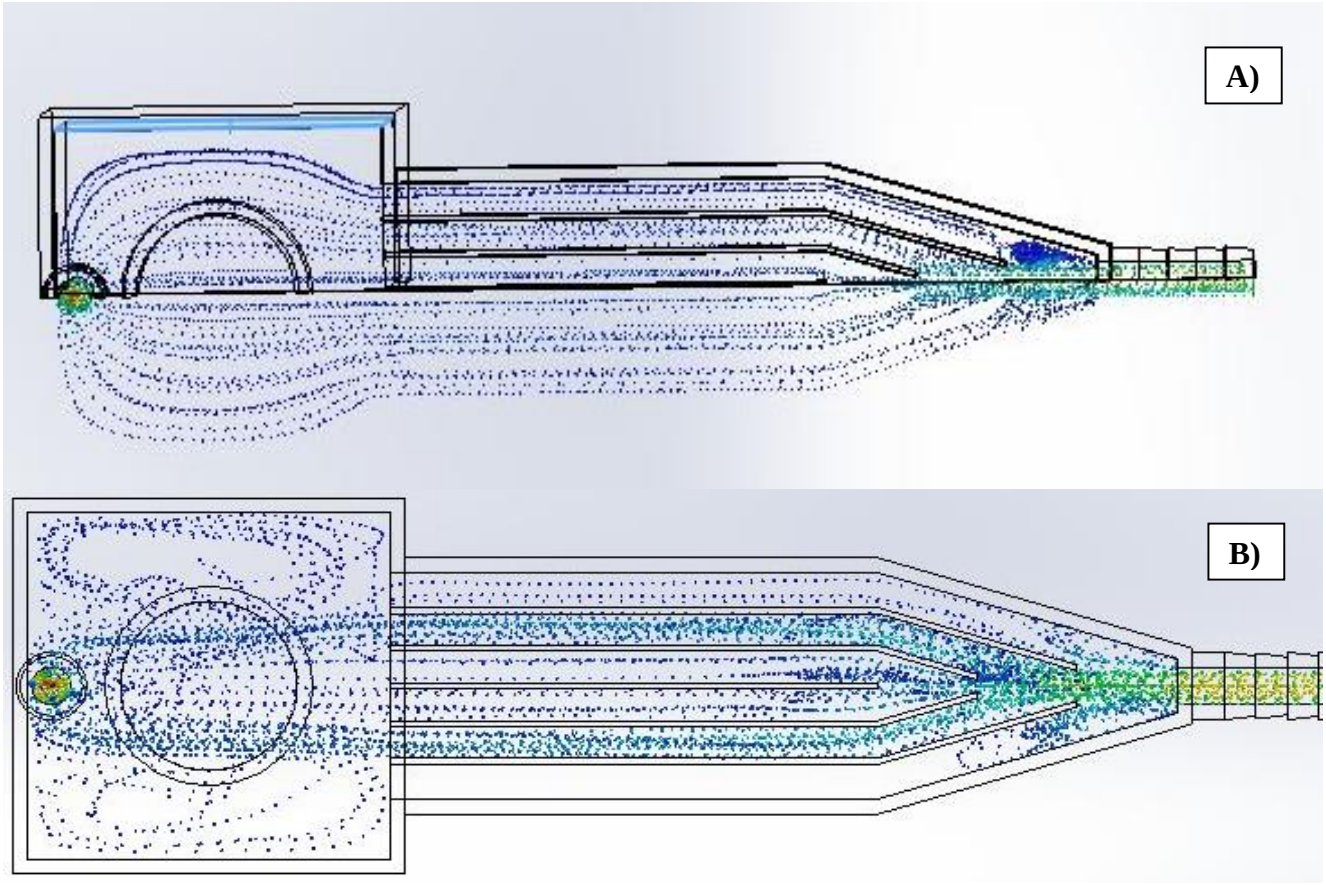

Figure 6.3: Flow patterns for (A) the finished cell at optimal flow rates and (B) the finished cell under high flow rate and thus turbulent flow, which disrupts the orientation of platelets. The electrolyte flows from the inflow valve, on the right, to the outflow valve on the left. Velocity follows the visual spectrum, from blue (slow) to red (fast).

The Reynolds Number (Re) for velocity (m/s) (v), travelled distance (m) (L), and kinematic viscosity (m^2/s) (ν) is:

$$\mathrm{Re} = \frac{\mathrm{v}L}{\nu} \tag{6.2}$$

For flow in a pipe, as occurs in the majority of the flow cell, Equation (2) can be modified to:

$$\mathrm{Re} = \frac{\mathrm{Q}D}{\nu A}, D = \frac{4A}{P} \tag{6.3}$$

Where Q is the flow rate (m^3/s), D the hydraulic diameter (m), A the area (m^2), and P is the wetted perimeter (m). At low numbers, the flow is laminar, which results in the fluid flowing in discrete layers. These layers facilitate a similar orientation of the clay platelets. In contrast, high Reynolds numbers (>2300) result in turbulent flow, which consists of random fluid movement that prevents

anisotropy. In addition, high flow rates may interfere with the deposition process. However, the platelets require at least some flow to orient. The range of flow rates used in this study was determined by converting the shear rate into flow rate from the studies on the effects of flow on orientation in clay platelets performed by Ramsey et al. [16]. The shear rate converted into velocity by using the equation for shear rate at the inner edge of a pipe of diameter (*d*), given as:

$$\dot{y} = \frac{8\mathrm{v}}{d} \rightarrow \mathrm{v} = \frac{d\dot{y}}{8} = \frac{0.25 \cdot 25}{8} = \frac{25}{32} = 0.78125 \ \frac{\mathrm{in}}{\mathrm{s}} \tag{6.4}$$

Using the value of velocity from Equation (6.4), the calculated flow rate (F) is:

$$\mathrm{F} = \frac{\pi d^2 \mathrm{v}}{4} = \frac{\pi \cdot 0.25^2 \cdot 0.78125}{4} = 0.0383 \frac{\mathrm{in}^3}{\mathrm{s}} \tag{6.5}$$

and converted into:

$$0.0383 \ \frac{\mathrm{in}^3}{\mathrm{s}} \cdot \frac{60\mathrm{s}}{\mathrm{m}} \cdot \frac{0.0164\mathrm{L}}{\mathrm{in}^3} \cdot \frac{1000\mathrm{mL}}{\mathrm{L}} = 37.7 \ \frac{\mathrm{mL}}{\mathrm{m}} \tag{6.6}$$

Based on this value, the experiment was conducted between 0-100 mL/min.

6.2.2 Deposition and Materials

An EG&G Princeton Applied Research Model 273A potentiostat/galvanostat was used for electrodeposition of nickel and Ni-MMT. The electrochemical system consisted of a three electrode system. The working electrode was a mounted stainless steel disc in epoxy, the counter electrode was a coiled chromel wire, and a saturated calomel reference electrode (SCE). The deposition parameters and electrochemical bath conditions were determined in a previous work [13]. A 5g/L MMT (Southern Clay Products) solution with 14.56 grams of $NiSO_4 \cdot 6H_2O$ (Alfa-Aesar), 10.58 grams of $Na_3C_6H_5O_7 \cdot 6H_2O$ (Fisher), and 4.6 grams of $H_3C_6H_5O_7$ (Fisher) buffered at pH 3.0 was used for deposition. While higher concentrations of clay help induce anisotropy in the platelets, the kinematic viscosity increases rapidly when clay is added in excess of 0.5%, which leads to difficulty with plating, as seen in Figure 6.4 [13]. The MMT platelets were exfoliated by

mechanical stirring for 24-48 hours. During the electrodeposition process, the plating solution was flowed at 0, 20, 40, 60, 80, and 100 milliliters per minute to determine an optimal flow rate.

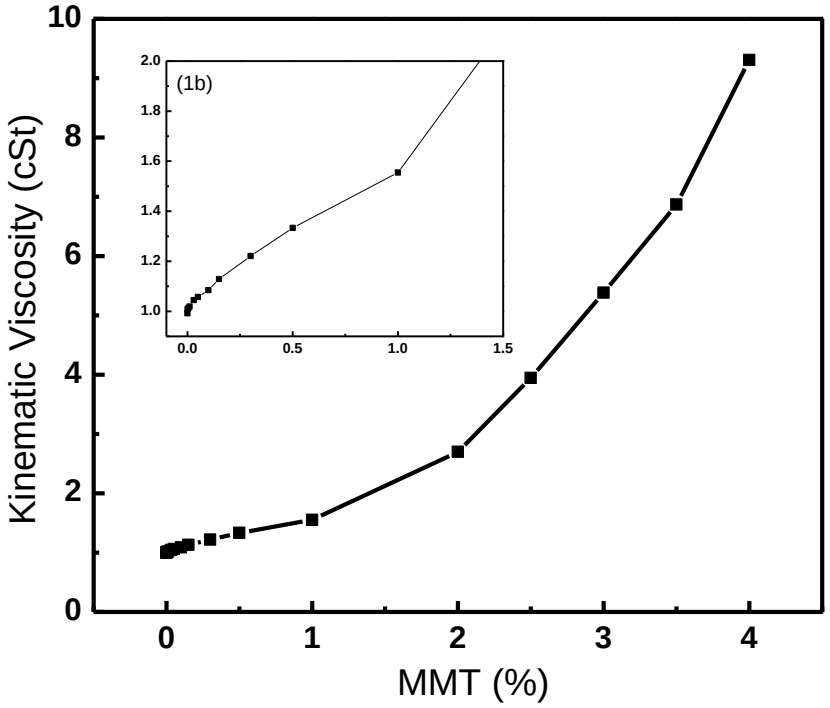

Figure 6.4: Kinematic viscosity of varying percentages (0-4%) of MMT in aqueous solution [13].

While MMT was chosen for this study, the results are not limited to MMT; rather, the flow cell could be used to obtain similar results for all platelet-type inorganic compounds, as the mechanism for shear-induced orientation is the same [7]. As each class of compounds shows different properties, and as clays can be modified to express additional properties through organic additives, this opens up many avenues of research (Table 6.1).

Table 6.1: Common clays that could be co-deposited with this flow cell, along with examples of their uses and beneficial properties.

Type	Beneficial Properties
Beidellite	Corrosion protection [22]. Catalysts (as a pillared clay) [23].
Kaolinite	Wastewater treatment [24]. Chemically inert [25].
Laponite	Biocatalyst [26]. Corrosion resistance [27].
Layered Double Hydroxides	Use in electronics [28]. Corrosion resistance [29].
Montmorillonite	Resistance to temperature, pH, and many corrosive chemicals [30]. Improved mechanical properties when co-deposited [31].

6.2.3 Characterization

X-ray Diffraction (XRD) (Siemens D-500 Diffractometer) with Williamson-Hall analysis was performed to determine the crystal structure and particle size of the pure Ni and Ni-MMT composite coatings. The experiment was performed with a Cu Kα radiation $\lambda = 0.15406$ nm at 35 kV and 24 mA. The scans were obtained from 40-100° 2θ with a step size of 0.05° and a dwell time of 1 second. Scanning Electron Microscopy (SEM) was used to determine the morphology of the composite coatings. The micrographs of the coatings were obtained using an Environmental FEI Quanta 200 scanning electron microscope with an Everhart Thornley detector. Energy dispersion spectroscopy (EDS) was used to determine the elemental composition for MMT (Al and Si) in the composite coatings. Potentiodynamic Polarization with Tafel analysis was performed on a Parstat 4000 (Princeton Applied Research) using Versa Studio software to determine the corrosion resistance of the coatings. A three electrode electrochemical cell was used as the corrosion testing system which was comprised of the working electrode film, two counter graphite rods, and a saturated calomel electrode (SCE) as the reference electrode. The potentiodynamic polarization was performed at a ±250 mV potential range and was applied to the cell with a scan rate of 0.1667 mV/s.

6.3 Results and Discussion

6.3.1 Reynolds Number

Reynolds number is a measure of whether a flow pattern is laminar or turbulent. As MMT platelets orient under laminar conditions, flow rates were examined that fall within the boundaries of laminar flow ($Re < 2300$), while also being near the flow rates previously found to orient MMT

[16]. The Reynolds number was calculated using Equation (6.3) for the flow rates tested (Table 6.2). While the Re increased with flow rate, it remained far below turbulent.

Table 6.2: Reynolds Numbers for various flow rates within the flow cell used for the deposition of Ni-MMT films. Kinematic viscosity of the plating bath used for deposition was 2.2 cSt [13].

Flow Rate (mL/min)	0	20	40	60	80	100
Reynolds Number (Re)	0	19.2	38.4	57.6	76.8	96

6.3.2 X-Ray Diffraction

XRD scans were performed to determine the crystal structure and particle size with changes in the flow rate for pure Ni and Ni-MMT during the electrodeposition process (Figure 6.5 and Figure 6.6). As the flow rate is increased, the (200) plane started to grow preferentially compared to the (111) in the XRD patterns, which shows that the flow does have an effect on the crystal structure of the composite coatings. Also in the XRD patterns, the peaks corresponding to the reinforced MMT particles are not observed even at low 2θ angles from the composite coatings due to complete exfoliation of the MMT.

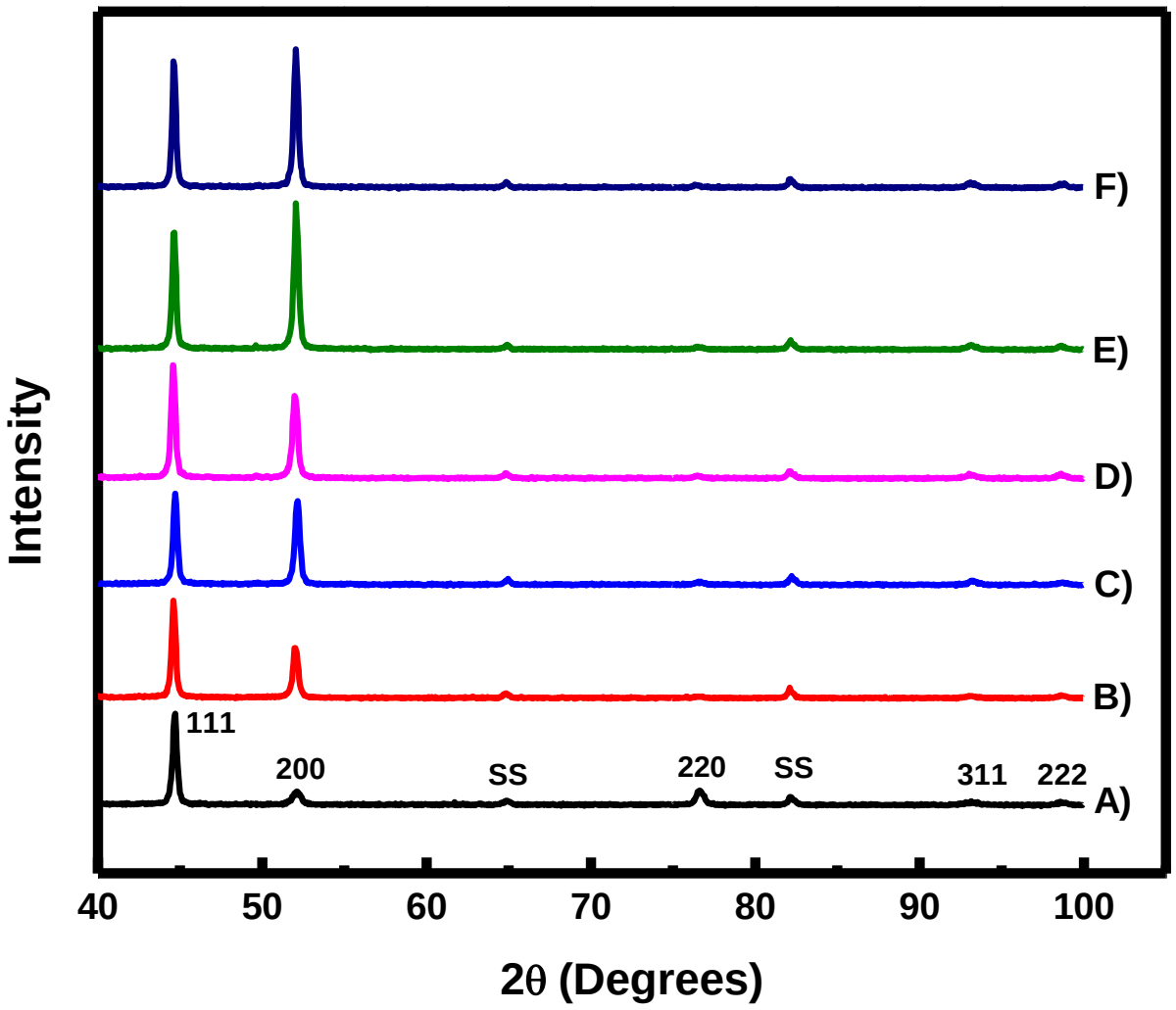

Figure 6.5: X-ray diffraction patterns of Ni-MMT coatings at a flow rate of: A) 0 mL/min, B) 20 mL/min, C) 40 mL/min, D) 60 mL/min, E) 80 mL/min, and F) 100 mL/min. (SS – stainless steel substrate)

The FWHM values (Full-Width at Half-Maximum) were determined for the peaks to calculate the peak broadening and how it relates to the particle size. A Williamson-Hall analysis was performed, and a pure silicon standard, which has no sample broadening, was used to calculate the instrumental broadening. The broadening (β) of the sample was determined by removing instrumental broadening with the Gaussian equation:

$$B^2_{sample} = B^2_{total} - B^2_{instrumental} \quad (6.7)$$

The Williamson-Hall equation was calculated, where η is strain, k a constant, λ the wavelength used, and *L* the crystallite size:

$$B_{sample}\cos\theta = \eta\sin\theta + \frac{k\lambda}{L} \quad (6.8)$$

Examining this equation at θ=0 (which was determined from the linear regression of observed points) yields:

$$B_{sample} = \frac{k\lambda}{L} \quad (6.9)$$

The proportionality constant k was assumed to be 1, and the λ = 0.15406 nm from the Cu Kα radiation.

Using the Williamson-Hall method, the average crystallite size (n = 3) was determined for the flow-cell films (Figure 6.6). The data showed that the deposition of pure Ni stayed consistent at around 60-70 nm as the flow rate changed. However, the Ni-MMT coating particle size sharply decreased at the 20 mL/min flow rate and then continued to rise well above pure Ni by 100 mL/min. This decrease in particle size between the flow rates of 20-40 mL/min was observed at flow rates similar to where the MMT platelets are hypothesized to orient, which leads to the conclusion that the MMT may be completely oriented optimally in the horizontal position. As the flow rate further increased the anisotropy flow of the MMT platelets became disrupted, which alters the normal deposition of nickel leading to larger particle sizes.

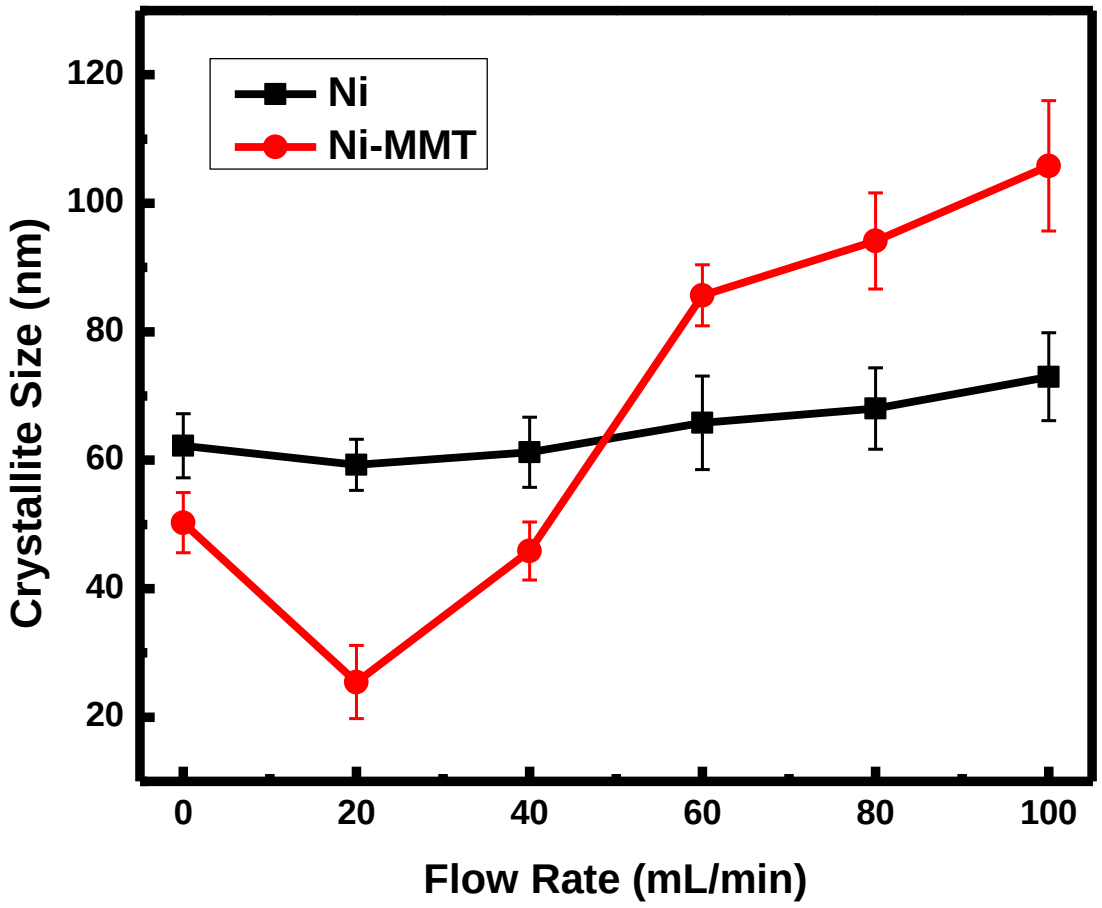

Figure 6.6: Particle sizes calculated from Williamson-Hall for the pure Ni and Ni-MMT coatings deposited at various flow rates (0-100 mL/min).

6.3.3 Scanning Electron Microscopy and Energy Dispersion Spectroscopy

SEM was performed to study the morphology of the prepared MMC coatings. In Figure 6.7, the micrographs show that the coatings are more compact and smoother for flow rates of 0-40 mL/min. The films deposited between flow rates of 60-100 mL/min show a rougher surface morphology and sharper edges on the surface, characteristic of films deposited with the same conditions but without flowing.

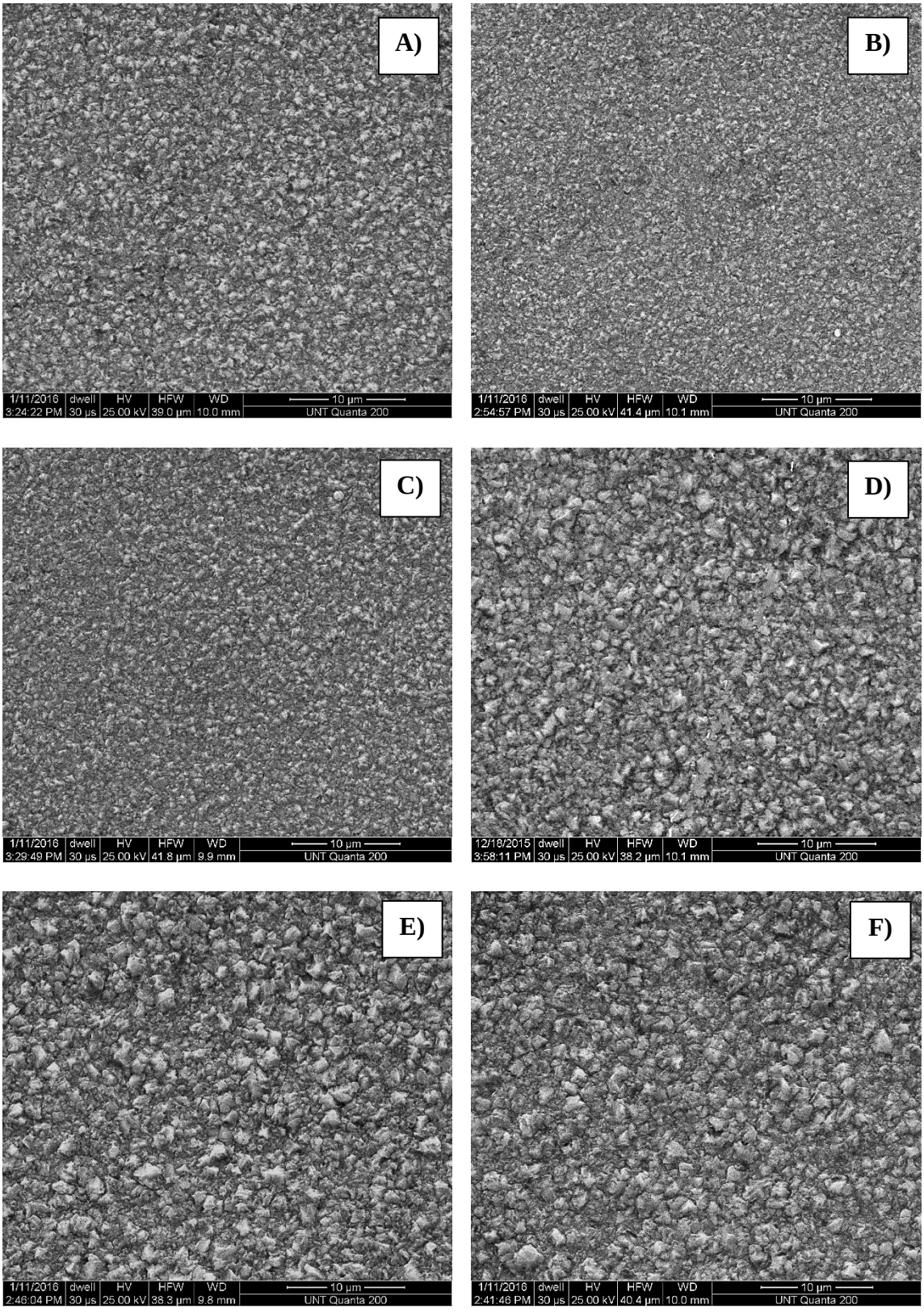

Figure 6.7: SEM micrographs of Ni-MMT at a flow rate of: A) 0 mL/min, B) 20 mL/min, C) 40 mL/min, D) 60 mL/min, E) 80 mL/min, and F) 100 mL/min.

EDS was used to obtain the MMT composition in the Ni coatings (Table 6.3). The composition of Si and Al were determined to study the effect of change in flow rate on the amount of MMT being incorporated into the film. The EDS results showed that as the flow rate increased to 20 mL/min the highest concentration of MMT was incorporated and slowly decreased as the flow rate continued to rise. This result confirms that as the flow increases above 40 mL/min the anisotropy flow breaks down with platelets falling out of orientation leading to lower amounts of MMT being embedded into the Ni matrix.

Table 6.3: Energy Dispersion Spectroscopy of the pure Ni at a flow rate of 0 mL/min and Ni-MMT at 0, 20, 40, 60, 80, and 100 mL/min.

Coatings	Nickel (%)	Silicon (%)	Aluminum (%)
Pure Ni 0 Flow	100	---	---
Ni-MMT 0 Flow	96.47	2.21	1.32
Ni-MMT 20 Flow	93.58	3.67	2.75
Ni-MMT 40 Flow	96.26	2.34	1.40
Ni-MMT 60 Flow	97.02	1.91	1.07
Ni-MMT 80 Flow	97.39	1.73	0.88
Ni-MMT 100 Flow	97.89	1.50	0.61

6.3.4 Tafel Analysis

The corrosion resistance of the pure Ni and Ni-MMT composite coatings were evaluated using potentiodynamic polarization with Tafel analysis, as seen in Figure 6.8 and Table 6.4. As the flow increased to between 20-40 mL/min, the i_{corr} values decreased below pure Ni and Ni-MMT at the 0 mL/min flow rate and then rose above those values at 60-100 mL/min. The i_{corr} values were calculated using the Stern-Geary equation:

$$i_{corr} = \frac{\beta_a \ \beta_c}{2.303 R_p(\beta_a + \beta_c)} \tag{6.10}$$

β_a and β_c are the respective anodic and cathodic Tafel slopes. The R_p, polarization resistance of the coating, values shown in Table 6.4 were calculated by taking the slope of a linear polarization scan at ±20 mV at 0.1667 mV/s. The best R_p values were obtained at a flow rate of 20-40 mL/min, as they were above the resistance observed for the pure Ni and Ni-MMT at 0 mL/min flow rate. Above 40 mL/min, the R_p value began to decrease to values above pure Ni and Ni-MMT at the 0 mL/min flow rate. The addition of MMT into the Ni matrix at flow rates of 20-40 mL/min helped to significantly increase the corrosion resistance of the coating by providing the optimal barrier protection to slow the mean free path of corrosion.

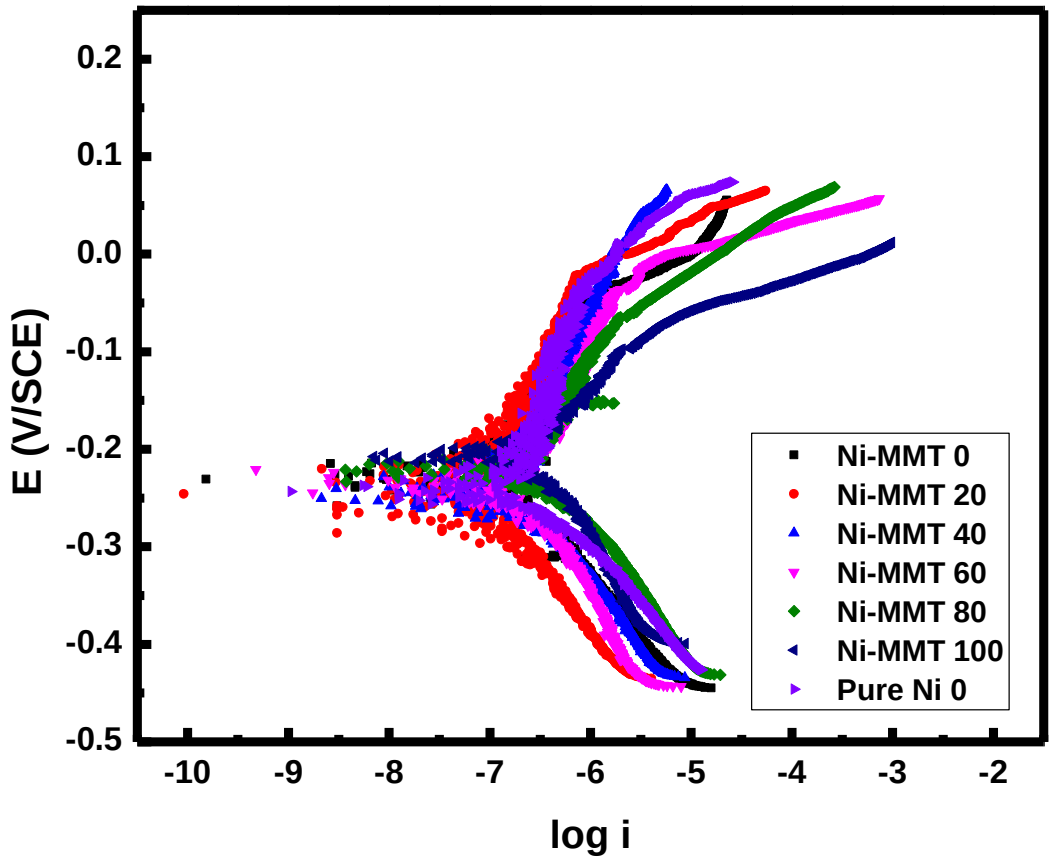

Figure 6.8: Tafel plots of pure Ni at a flow rate of 0 mL/min and Ni-MMT at 0, 20, 40, 60, 80, and 100 mL/min.

Table 6.4: E_{corr}, I_{corr}, and polarization resistance (R_p) of pure Ni at a flow rate of 0 mL/min and Ni-MMT at 0, 20, 40, 60, 80, and 100 mL/min.

Coatings	E_{corr} (V)	i_{corr} (Acm^{-2})	R_p ($k\Omega \bullet cm^2$)
Pure Ni 0 Flow	-0.228	1.35×10^{-7}	221.9
Ni-MMT 0 Flow	-0.229	1.27×10^{-7}	242.7
Ni-MMT 20 Flow	-0.246	6.26×10^{-8}	473.1
Ni-MMT 40 Flow	-0.245	1.07×10^{-7}	276.8
Ni-MMT 60 Flow	-0.236	2.44×10^{-7}	171.0
Ni-MMT 80 Flow	-0.213	3.34×10^{-7}	83.57
Ni-MMT 100 Flow	-0.206	5.68×10^{-7}	43.82

6.4 Conclusions

A novel flow cell was designed for the incorporation of platelet type particles into a metal matrix. SolidWorks software was successfully used to model the flow of the plating solution over the surface of the electrode. A flow rate of 20-40 mL/min showed the highest incorporation of MMT, the smallest particle size, and the best corrosion resistance. As, the flow rate rose above 40 mL/min the platelets began to disorient leading to larger particle sizes and lower corrosion resistances. This flow cell could help to improve the incorporation of platelet type particles with various properties into the metal matrix for many different types of applications.

6.5 References

[1] D.E. Rusu, P. Cojocaru, L. Magagnin, C. Gheorghies, G. Carac, *J. Optoelectron Adv. M.* **2010**, 12, 2419.

[2] R. Sen, S. Das, K. Das, Metall. *Mater. Trans. A* **2012**, 43A, 3809.

[3] M.R. Vaezi, S.K. Sadrnezhaad, L. Nikzad, *Colloids and Surf. A* **2008**, 315, 176.

[4] L.M. Chang, J.H. Liu, R.J. Zhang, *Mater. Corros.* **2011**, 62, 920.

[5] Y.H. Ahmad, A.M.A. Mohamed, *Int. J. Electrochem. Sci.* **2014** 9, 1942.

[6] R.A. Horch, T.D. Golden, N.A. D' Souza, L. Riester, *Chem. Mater.* **2002**, *14*, 3531.

[7] J.D. Ramsay, S.W. Swanton, J. Bunce, *Journal of the Chemical Society, Faraday Transactions* **1990** 86, 3919.

[8] T.R. Khan, A. Erbe, M. Auinger, F. Marlow, M. Rohwerder, *Science and Technology of Advanced Materials*, 2011, 12, 055005.

[9] A.B. Vidrine, E.J. Podlaha, *J. App. Electrochem.* **2001**, 31, 461.

[10] S.T. Aruna, V.K. Grips, V.E. Selvi, K.S. Rajam, *J. App. Electrochem.*, **2007**, 37, 991.

[11] Y. Xuetao, W. Yu, S. Dongbai, Y. Hongying, *Surf. Coat. Tech.* **2008**, 202, 1895.

[12] L. Wang, J. Zhang, Y. Gao, Q. Xue, L. Hu, T. Xu, *Scripta Materialia* **2006**, 55, 657.

[13] J. Tientong, C.R. Thurber, N. D'Souza, A.M.A. Mohamed, T.D. Golden, *Int. J. Electrochem.* **2013**, 2013, 1.

[14] J. Tientong, Y.H. Ahmad, M. Nar, N. D'Souza, A.M.A. Mohamed, T.D. Golden, *Mater. Chem. Phys.* **2014**, 145, 44.

[15] Y.H. Ahmad, J. Tientong, N. D'Souza, T.D. Golden, A.M.A. Mohamed, *Surf. Coat. Tech.* **2014**, 242,170.

[16] J.D. Ramsay, P. Lindner, *Journal of the Chemical Society, Faraday Transactions,* **1993**, 89, 4207.

[17] T.H. Lin, W.H. Huang, I.K. Jun, P. Jiang, *InTech* **2011**, 6, 127.

[18] F.C. Walsh, C. Ponce de Leon, *Trans. Inst. Met. Finish.* **2014**, 92, 83.

[19] J. Lapinski, D. Pletcher, F.C. Walsh, *Surf. Coat. Techn*. **2011**, 205, 5205.

[20] V.D. Stankovic, M. Gojo, *Surf. Coat. Techn*. **1996**, 81, 225.

[21] C.C. Lee, C.C. Wan, *J. Electrochem. Soc.* **1988**, 135, 1930.

[22] A.A. Aghzzaf, B. Rhouta, E. Rocca, A. Khalil, J. Steinmetz, *Corr. Sci.*, **2014**, 80, 46.

[23] R. Setton, *Pillared Montmorillonite and Beidellite: Acidity and Catalytic Properties*, Dordrecht: D. Reidel **1986**.

[24] T. Leiviskä, S. Gehör, E. Eijärvi, A. Sarpola, J. Tanskanen, *Central European Journal of Engineering* **2012**, 2, 239.

[25] H.H. Murray, *Clays and Clay Minerals* **1961**, 10, 291.

[26] J. Feng, X. Hu, P.L. Yue, H.Y. Zhu, G.Q. Lu, *Chemical Engineering Science* **2003**, 58, 679.

[27] M. Gordon, *Master's Thesis*, Virginia Polytechnic Institute and State University, Blacksburg, Virginia **2003**.

[28] X. Guo, F. Zhang, D.G. Evans, X. Duan, *Chemical Communications* **2010**, 46, 5197.

[29] F. Zhang, M. Sun, S. Xu, L. Zhao, B. Zhang, *Chemical Engineering Journal* **2008**, 141, 362.

[30] D. Zaarei, A.A. Sarabi, F. Sharif, S.M. Kassiriha, *Journal of Coatings Technology and Research* **2008**, 5, 241.

[31] A.Q. Wang, N. D'souza, T.D. Golden, (2006). *Journal of Materials Chemistry* **2006**, 16, 481.

CHAPTER 7

CONCLUSIONS AND FUTURE WORK

7.1 Conclusions

Electrodeposition of metal matrix composites has become popular for corrosion resistance and hardness in the oil and gas industry because of the major problems that persist with corrosion. In the oil and gas industry, high corrosion resistance and hardness are needed to extend the lifetime of coatings due to exposure to high stress and salt environments. Electrodeposition has become a favorable technique in synthesizing coatings because of low cost, convenience, and the ability to work at low temperatures. Two major alloys of copper-nickel, 90-10 and 70-30, were evaluated for microbial corrosion protection in marine environments on a stainless steel substrate. Copper and copper alloys are commonly used in marine environments to resist biofouling of materials by inhibiting microbial growth. Also, a novel flow cell design for the enhanced deposition of metal matrix composites was examined to obtain the optimal oriented structure of the layered silicates in the metal matrix. With the addition of montmorillonite into the Ni and Cu-Ni matrix, an increase in strength, adhesion, wear and fracture toughness of the coating occurs, which leads to an increase corrosion resistance and longevity of the coating. These coatings were evaluated for composition and corrosion using many different types of instrumental and electrochemical techniques. The overall corrosion resistance and mechanical properties were improved with the composite films in comparison to the pure metals, which proves to be advantageous for many economic sectors including the oil and gas industry.

Literature surveying the electrodeposition of Cu-Ni incorporated with nano- to micro-particles to produce metal matrix composites has been reviewed. The inclusion of particles into

the metal matrix produced enhanced properties in the areas of electronics, mechanics, electrochemistry, and corrosion. In electronics, an increase in the magnetic properties and durability for microactuators was observed. Measurements of the mechanical properties showed an increase in hardness, wear resistance, shear adhesion, and tensile strength for the material. The corrosion resistance of the metal matrix coatings was improved over that of pure Cu-Ni. As the accessibility of nanoparticles continues to increase, the interest in reduced cost and low temperature electrodeposited metal matrix composites continues to rise. However, only a small number of articles have investigated Cu-Ni composite coatings, these composite coatings need further examination due to their advantageous properties.

A copper-nickel alloy (70:30 ratio) was electrochemically deposited and compared to a composite coating incorporating layered silicate platelets to obtain copper-nickel-montmorillonite (MMT). The composite coatings were electrochemically deposited from a citrate bath to investigate the effects of MMT on the corrosion and mechanical properties of the coatings. Incorporation of MMT into the Cu-Ni alloy films was not affected by the deposition parameters such as applied voltage and pH. Scanning electron microscopy and atomic absorption spectroscopy confirmed the successful incorporation of the MMT into the coatings. Longer term stability in the presence of corroding solutions was noted for the copper-nickel composite films. The Tafel calculations showed an increase in polarization resistance, R_p, from 190.7 kΩ•cm^2 for pure Cu-Ni to 314.3 kΩ•cm^2 for Cu-Ni-0.2% MMT after soaking the coatings in 3.5% NaCl at 25°C for two weeks, which was consistent with the resistance increase measured by electrochemical impedance spectroscopy. Microhardness test results showed about a 25% increase in the hardness for the copper-nickel coatings incorporated with the layered silicate platelets versus the pure Cu-Ni coating.

Due to frequent problems with corrosion, the need for cost efficient protective coatings continues to rise. Copper-Nickel-montmorillonite (Cu-Ni-MMT) films were studied to determine the effects of MMT on the corrosion and mechanical properties of nanocomposite coatings. A 90-10 Cu-Ni alloy was electrodeposited with varying amounts of MMT embedded into the metallic matrix. The improved mechanical properties include a 17% increase in the hardness and an 85% increase in the shear adhesion strength with the incorporation of MMT. The enhanced corrosion properties show an increase in the polarization resistance from 11.77 $k\Omega \bullet cm^2$ for the pure Cu-Ni to 33.28 $k\Omega \bullet cm^2$ for the Cu-Ni-0.15% MMT coating after being soaked in a simulated seawater environment for 30 days, which was also similar to the increase seen in the electrochemical impedance spectroscopy measurements. The incorporation of MMT also helped to stabilize the corrosion potential during the 30 day immersion study.

The 70-30 and 90-10 Cu-Ni-MMT coatings were examined with for corrosion potential, corrosion current, polarization resistance, hardness, and shear adhesion. Table 7.1 shows the results of both alloy conditions.

Table 7.1: Summarized characterization values for the Cu-Ni-MMT coatings.

Coating Type	E_{corr} (V/SCE)	i_{corr} (Acm^{-2})	R_p ($k\Omega \bullet cm^2$)	Hardness (HV)
70-30 Cu-Ni	-0.376	$1.24x10^{-6}$	190.7	185±5
70-30 Cu-Ni-0.05% MMT	-0.354	$8.27x10^{-7}$	208.1	219±10
70-30 Cu-Ni-0.10% MMT	-0.349	$7.20x10^{-7}$	239.7	221±10
70-30 Cu-Ni-0.20% MMT	-0.197	$5.60x10^{-7}$	314.3	232±8
90-10 Cu-Ni	-0.349	$2.50x10^{-6}$	11.77	200±4
90-10 Cu-Ni-0.05% MMT	-0.347	$1.66x10^{-6}$	15.50	214±7
90-10 Cu-Ni-0.10% MMT	-0.336	$1.56x10^{-6}$	17.10	227±3
90-10 Cu-Ni-0.15% MMT	-0.220	$9.84x10^{-7}$	33.28	234±5

A novel electrochemical flow cell was designed to aid in the deposition of layered silicates into a metal matrix. Metal matrix composites involving platelet type particles have shown promise. However, the deposited platelets show random orientation, limiting their properties. Computational fluid dynamics simulations in SolidWorks have shown this newly designed flow cell to generate flow patterns capable of orienting clay platelets, which can then be deposited in an oriented manner. The flow rates between 20-40 mL/min produced the best properties by having highest incorporation of MMT, the smallest particle size, and the best corrosion resistance. Although, as the flow rate increased to above 40 mL/min the platelets began to disorient leading to larger particle sizes and lower corrosion resistances. Table 7.2 displays the overall findings from the flow cell experiments for particle size, corrosion potential, corrosion current, and resistance.

Table 7.2: Summarized characterization values for the various flow rate for the Ni-MMT coatings.

Coating Type	E_{corr} (V/SCE)	i_{corr} (Acm^{-2})	R_p ($k\Omega \bullet cm^2$)	Particle Size (nm)
Pure Ni 0 Flow	-0.228	$1.35x10^{-7}$	221.9	59.3
Ni-MMT 0 Flow	-0.229	$1.27x10^{-7}$	242.7	49.7
Ni-MMT 20 Flow	-0.246	$6.26x10^{-8}$	473.1	23.7
Ni-MMT 40 Flow	-0.245	$1.07x10^{-7}$	276.8	48.1
Ni-MMT 60 Flow	-0.236	$2.44x10^{-7}$	171.0	81.1
Ni-MMT 80 Flow	-0.213	$3.34x10^{-7}$	83.57	90.6
Ni-MMT 100 Flow	-0.206	$5.68x10^{-7}$	43.82	96.3

7.2. Future Work

The incorporation of MMT into other metal or metal alloy systems need to be examined. This concept can be further expanded to examine improvement of other desired material

properties. A tri-alloy examining zinc-copper-nickel with montmorillonite incorporation would be a beneficial coating. Zinc-copper-nickel coatings are shown to have better corrosion resistance to chloride attack (due to the sacrificial nature of zinc).

The Cu-Ni-MMT coatings could be immersed in a simulated seawater that is flowed at different flow rates to test erosion corrosion. 70-30 Cu-Ni coatings are commonly used in spray zones where high mechanical properties are needed and the incorporation of MMT could help extend the lifetime of coatings in these environments. The flow cell designed in chapter 6 could be used to facilitate this experiment.

The flow cell samples need be tested mechanically to see if the oriented platelets help improve the mechanical properties. The flow cell could be furthered examined by dispersing different types of platelet type particles, such as layered double hydroxides, to better reinforce MMC coatings to slow the rate of corrosion. With better dispersion of the particles into the metal matrix, the mean free path to corrosion can be further inhibited, which would reduce the rate of corrosion and help to enhance the mechanical properties.

BIOGRAPHICAL INFORMATION

CASEY RAY THURBER

Publications

C.R. Thurber, M. Hashe, R.E. Daugherty, T.D. Golden "A Novel Flow Cell Design for Electrodeposition of Metal Matrix Composite Coatings" (Submitted).

C.R. Thurber, Y.H. Ahmad, M.C. Calhoun, Amaal Al-Shenawa, N. D'Souza, A.M.A. Mohamed, T.D. Golden "Improved Corrosion and Mechanical Properties of Electrodeposited 90-10 Cu-Ni Incorporated with Layered Silicates" (Submitted).

C.R. Thurber, A.M.A. Mohamed, T.D. Golden "Electrodeposition of Cu-Ni Composite Coatings" Electrodeposition of Composite Materials. Intech. pp. 83-104, 2016, ISBN 978-953-51-4633-9.

C.R. Thurber, Y.H. Ahmad, Stephen F. Sanders, Amaal Al-Shenawa, N. D'Souza, A.M.A. Mohamed, T.D. Golden "Electrodeposition of 70-30 Cu-Ni Nanocomposite Coatings for Enhanced Mechanical and Corrosion Properties" *Curr. Appl. Phys.*, vol. 16, pp. 387-396, 2016.

K.M. Haynes, K.C. Kratch, S.D. Stovall, C.O. Obondi, C.R. Thurber, W.J. Youngblood "Tuning Interfacial Electron Transfer in Nanostructured Cuprous Oxide Photoelectrochemical Cells with Chare-Selective Molecular Coatings" *ACS Appl. Mater. Interfaces*, vol. 7, pp. 16133-16137, 2015.

C.R. Thurber, M.C. Calhoun, Y.H. Ahmad, N. D'Souza, A.M.A. Mohamed, T.D. Golden "Electrodeposition of Cu-Ni Incorporated with Layered Silicates for Corrosion Protection" *ECS Trans.* vol. 61 (20), pp. 49-60, 2014.

J. Tientong, S. Garcia, C.R. Thurber, T.D. Golden "Synthesis of Nickel and Nickel Hydroxide Nanopowders by Simplified Chemical Reduction" *J. Nanotechnol.*, vol. 2014, pp. 1-6, 2014.

J. McDonald, K.L. Steelman, P. Veth, J. Mackey, J. Loewen, C.R. Thurber, T.P. Guilderson "Results from the first intensive dating program for pigment art in the Australian arid zone: insights into recent social complexity" *J. Archaeol. Sci.*, vol. 46, pp. 195-204, 2014.

J. Tientong, C.R. Thurber, N. D'Souza, A. Mohamed, and T.D. Golden "Influence of Bath Composition at Acidic pH on Electrodeposition of Nickel-Layered Silicate Nanocomposites for Corrosion Protection "*Int. J. Electrochem.*, vol. 2013, pp. 1-8, 2013.

Presentations

C.R. Thurber, M.C. Calhoun, Y.H. Ahmad, A. Al-Shenawa, N. D'Souza, A. Mohamed, T.D. Golden "Enhanced Corrosion and Mechanical Properties of 90-10 Cu-Ni Nanocomposite Coatings" SAMPE, Irving, TX, April 23rd 2015. (Poster-Placed 1st)

C.R. Thurber, M.C. Calhoun, Y.H. Ahmad, N. D'Souza, A.M.A. Mohamed, T.D. Golden "Electrodeposition of 90-10 Cu-Ni Nanocomposite Coatings for Corrosion Protection" 2015 Federation Graduate Student Research Symposium, Texas Woman's University, Denton, TX, April 10th, 2015. (Poster)

C.R. Thurber, M.C. Calhoun, Y.H. Ahmad, A. Al-Shenawa, N. D'Souza, A. Mohamed, T.D. Golden "Enhanced Corrosion and Mechanical Properties of 90-10 Cu-Ni Nanocomposite Coatings" NACE Corrosion 2015, Dallas, TX, March 15th-19th 2015. (Poster- Honorable Mention)

C.R. Thurber, M.C. Calhoun, Y.H. Ahmad, A. Al-Shenawa, N. D'Souza, A.M.A. Mohamed, T.D. Golden " Electrodeposition of 90-10 Cu-Ni Nanocomposite Coatings for Corrosion Protection " Pittcon 2015, New Orleans, LA, March 8th-12th, 2015. (Oral Presentation)

C.R. Thurber, M.C. Calhoun, Y.H. Ahmad, N. D'Souza, A.M.A. Mohamed, T.D. Golden "Electrodeposition of 90-10 Cu-Ni Nanocomposite Coatings for Corrosion Protection" 2015 Graduate Student Exhibition, University of North Texas, Denton, TX, March 7th, 2015. (Poster-Placed 1st)

C.R. Thurber, M.C. Calhoun, Y.H. Ahmad, S.F. Sanders, A. Al-Shenawa, N. D'Souza, A.M.A. Mohamed, T.D. Golden "Electrodeposition of Cu-Ni Nanocomposite Coatings for Enhanced Mechanical and Corrosion Properties" University of Central Arkansas Seminar Series, Conway, AR, February 13th 2015. (Invited Oral Presentation)

C.R. Thurber, M. C. Calhoun, S. F. Sanders, Y.H. Ahmad, N. D'Souza, A. Mohammed, T.D. Golden "Electrodeposition of 70-30 Cu-Ni Composite Coatings for Corrosion Protection "ACS Southwest Regional Meeting, Ft. Worth, TX, November 2014. (Poster)

C.R. Thurber, M.C. Calhoun, Y.H. Ahmad, N. D'Souza, A.M.A. Mohamed, T.D. Golden "Electrodeposition of Cu-Ni Incorporated with Layered Silicates for Microbial Corrosion Protection" 225th Electrochemical Society Meeting, Orlando, FL, May 11th – 15th, 2014. (Poster)

J. Tientong, C.R. Thurber, M.C. Calhoun, Y.H. Ahmad, N. D'Souza, A.M.A. Mohamed, T.D. Golden "Ni-Mo and Cu-Ni Nanocomposite Coatings for High-Temperature and Microbial Induced Corrosion" SAMPE DFW Meeting, Irving, TX, April 10th, 2014. (Poster-Placed 1st)

C.R. Thurber, M.C. Calhoun, Y.H. Ahmad, N. D'Souza, A.M.A. Mohamed, T.D. Golden "Electrodeposition of 90-10 and 70-30 Cu-Ni for Microbial Corrosion Protection" 247th American Chemical Society National Meeting, Dallas, TX, March 16th - 20th, 2014. (Poster)

C.R. Thurber, M.C. Calhoun, Y.H. Ahmad, N. D'Souza, A.M.A. Mohamed, T.D. Golden "Electrodeposition of 90-10 and 70-30 Cu-Ni for Microbial Corrosion Protection" 2014 Graduate Student Exhibition, University of North Texas, Denton, TX, March 1st, 2014. (Poster-Placed 2nd)

"Trace Element Analysis of Mineral Water Samples through XRF and ICP-MS" Ninth Annual University Scholars Day, University of North Texas, Denton, TX, April 2012.

"Radiocarbon dating rock art using a multi-sample plasma oxidation system" Poster Presentation at the 243rd American Chemical Society National Meeting, San Diego, CA, March 25th - 29th, 2012.

"Chemical Pretreatment and Plasma Oxidation on Aboriginal Paintings for Radiocarbon Dating" Poster Presentation at the 241st American Chemical Society National Meeting Anaheim, CA, March 27th - 31st, 2011.